



NAVAL POSTGRADUATE SCHOOL

MONTEREY, CALIFORNIA

THESIS

**OBSERVATIONS AND MODELING OF THE SHELF
CIRCULATION NORTH OF THE MONTEREY BAY
DURING AUGUST 2006**

by

Rebecca E. Wolf

June 2007

Thesis Advisor:
Second Reader:

Steven R. Ramp
Leslie K. Rosenfeld

Approved for public release; distribution is unlimited

THIS PAGE INTENTIONALLY LEFT BLANK

REPORT DOCUMENTATION PAGE			<i>Form Approved OMB No. 0704-0188</i>	
Public reporting burden for this collection of information is estimated to average 1 hour per response, including the time for reviewing instruction, searching existing data sources, gathering and maintaining the data needed, and completing and reviewing the collection of information. Send comments regarding this burden estimate or any other aspect of this collection of information, including suggestions for reducing this burden, to Washington headquarters Services, Directorate for Information Operations and Reports, 1215 Jefferson Davis Highway, Suite 1204, Arlington, VA 22202-4302, and to the Office of Management and Budget, Paperwork Reduction Project (0704-0188) Washington DC 20503.				
1. AGENCY USE ONLY (Leave blank)		2. REPORT DATE June 2007	3. REPORT TYPE AND DATES COVERED Master's Thesis	
4. TITLE AND SUBTITLE Observations and Modeling of the Shelf Circulation North of the Monterey Bay during August 2006			5. FUNDING NUMBERS	
6. AUTHOR(S) Rebecca E. Wolf			8. PERFORMING ORGANIZATION REPORT NUMBER	
7. PERFORMING ORGANIZATION NAME(S) AND ADDRESS(ES) Naval Postgraduate School Monterey, CA 93943-5000			10. SPONSORING/MONITORING AGENCY REPORT NUMBER	
9. SPONSORING /MONITORING AGENCY NAME(S) AND ADDRESS(ES) N/A				
11. SUPPLEMENTARY NOTES The views expressed in this thesis are those of the author and do not reflect the official policy or position of the Department of Defense or the U.S. Government.				
12a. DISTRIBUTION / AVAILABILITY STATEMENT Approved for public release; distribution is unlimited			12b. DISTRIBUTION CODE	
13. ABSTRACT (maximum 200 words) <p>In August of 2006 the Adaptive Sampling and Prediction (ASAP) experiment was conducted near the northern Monterey Bay. Multiple assets including aircraft, autonomous vehicles, moorings, and numerical models were used to gain a better understanding of three-dimensional upwelling centers. Data were collected at two separate mooring locations using Acoustic Doppler Current Profilers (ADCPs) during the experiment. The focus of this thesis is to determine the effects of local wind forcing on the ocean circulation and provide a comparison between the data collected at the mooring locations and numerical predictions for the region. Upwelling and relaxation events are used as the basis for understanding the local wind forcing. Upwelling typically results in equatorward flow while relaxation events typically result in poleward flow. Several different types of analyses were used to determine the effects of the local wind forcing. A visual analysis was performed with stick vector plots and component plots of the rotated time series that compared the wind with the data from the water column. Two methods of cross correlation, component correlations and vector correlations, were exploited as well as a spectral analysis of the wind and ADCP data. Finally the coherence and phase between the wind and currents were examined. Based on the analysis it became evident that the currents were forced by both wind and non-local events such as eddies, meanders, and the large-scale alongshelf pressure gradient.</p> <p>Associated with the ASAP experiment, the Harvard Ocean Prediction System (HOPS), the Regional Ocean Modeling System (ROMS), and the Navy Coastal Ocean Model (NCOM) provided nowcasts that were compared with the mooring data to determine their accuracy and precision. Overall, in the beginning of August the models provided reasonable representations of the flow patterns at the mooring locations. The prediction error increased towards the end of August which was possibly related to data assimilation techniques and more non-local forcing at that time. The military application of this thesis is that accurate current prediction by ocean models will benefit amphibious operations, special warfare operations, and mine warfare in the littoral zone</p>				
14. SUBJECT TERMS Monterey Bay, Adaptive Sampling and Prediction (ASAP) Experiment, Wind Forcing, Numerical Modeling			15. NUMBER OF PAGES 125	
			16. PRICE CODE	
17. SECURITY CLASSIFICATION OF REPORT Unclassified	18. SECURITY CLASSIFICATION OF THIS PAGE Unclassified	19. SECURITY CLASSIFICATION OF ABSTRACT Unclassified	20. LIMITATION OF ABSTRACT UL	

THIS PAGE INTENTIONALLY LEFT BLANK

Approved for public release; distribution is unlimited

**OBSERVATIONS AND MODELING OF THE SHELF CIRCULATION NORTH
OF THE MONTEREY BAY DURING AUGUST 2006**

Rebecca E. Wolf
Ensign, United States Navy
B.S., United States Naval Academy, 2006

Submitted in partial fulfillment of the
requirements for the degree of

MASTER OF SCIENCE IN PHYSICAL OCEANOGRAPHY

from the

**NAVAL POSTGRADUATE SCHOOL
June 2007**

Author: Rebecca E. Wolf

Approved by: Steven R. Ramp
Thesis Advisor

Leslie K. Rosenfeld
Second Reader

Mary L. Batteen
Chairman, Department of Oceanography

THIS PAGE INTENTIONALLY LEFT BLANK

ABSTRACT

In August of 2006 the Adaptive Sampling and Prediction (ASAP) experiment was conducted near the northern Monterey Bay. Multiple assets including aircraft, autonomous vehicles, moorings, and numerical models were used to gain a better understanding of three-dimensional upwelling centers. Data were collected at two separate mooring locations using Acoustic Doppler Current Profilers (ADCPs) during the experiment. The focus of this thesis is to determine the effects of local wind forcing on the ocean circulation and provide a comparison between the data collected at the mooring locations and numerical predictions for the region. Upwelling and relaxation events are used as the basis for understanding the local wind forcing. Upwelling typically results in equatorward flow while relaxation events typically result in poleward flow. Several different types of analyses were used to determine the effects of the local wind forcing. A visual analysis was performed with stick vector plots and component plots of the rotated time series that compared the wind with the data from the water column. Two methods of cross correlation, component correlations and vector correlations, were exploited as well as a spectral analysis of the wind and ADCP data. Finally the coherence and phase between the wind and currents were examined. Based on the analysis it became evident that the currents were forced by both wind and non-local events such as eddies, meanders, and the large-scale alongshelf pressure gradient.

Associated with the ASAP experiment, the Harvard Ocean Prediction System (HOPS), the Regional Ocean Modeling System (ROMS), and the Navy Coastal Ocean Model (NCOM) provided nowcasts that were compared with the mooring data to determine their accuracy and precision. Overall, in the beginning of August the models provided reasonable representations of the flow patterns at the mooring locations. The prediction error increased towards the end of August which was possibly related to data assimilation techniques and more non-local forcing at that time. The military application of this thesis is that accurate current prediction by ocean models will benefit amphibious operations, special warfare operations, and mine warfare in the littoral zone.

THIS PAGE INTENTIONALLY LEFT BLANK

TABLE OF CONTENTS

I.	INTRODUCTION.....	1
A.	BACKGROUND	1
B.	FUNDAMENTALS OF SHELF CIRCULATION	2
1.	Wind Forced Circulation	2
2.	Upwelling Events.....	3
3.	Wind Relaxation Events.....	5
C.	OVERVIEW OF MODEL SPECIFICATIONS	6
II.	DATA COLLECTION	11
A.	ACOUSTIC DOPPLER CURRENT PROFILERS.....	11
B.	COORDINATE ROTATION	12
C.	DATA FILTERING.....	12
III.	DATA ANALYSIS.....	13
A.	MEAN FLOW	13
B.	VISUAL ANALYSIS	13
C.	CROSS CORRELATIONS BETWEEN MOORING LOCATIONS	15
D.	SPECTRAL ANALYSIS.....	16
E.	COHERENCE AND PHASE CALCULATIONS.....	17
F.	RESPONSE OF SHELF CURRENTS TO WIND EVENTS.....	19
IV.	MODEL/DATA COMPARISONS.....	21
A.	DATA PROCESSING	21
B.	NUMERICAL MODEL ANALYSIS	23
1.	Principal Axis Ellipses	23
2.	Stick Vector Plots.....	24
3.	Components and Statistical Analysis	25
C.	SUMMARY OF MODEL COMPARISONS.....	27
D.	MILITARY AND OPERATIONAL APPLICATIONS.....	28
	APPENDIX A. FIGURES	29
	APPENDIX B. TABLES	79
	LIST OF REFERENCES.....	101
	INITIAL DISTRIBUTION LIST	105

THIS PAGE INTENTIONALLY LEFT BLANK

LIST OF FIGURES

Figure 1.	Illustration of coastal Ekman dynamics. Ekman transport is 90° to the right of the wind stress, therefore equatorward winds off the coast of Californian result in offshore transport, an important factor in the seasonal upwelling cycle.	29
Figure 2.	Visual depiction of the upwelling process. (From http://cordellbank.noaa.gov/environment/seasons.html , last accessed February 2007).	30
Figure 3.	Top: HOPS two way nested modeling scheme (From Pierre Lermusiaux, MIT) Middle: Hierarchy of Navy Coastal Ocean Models (NCOM) in the Pacific (from http://www7320.nrlssc.navy.mil , last accessed May 2007) Bottom: Digital representation of ROMS model nesting depicting a three level one-way nested scheme (From http://ocean.jpl.nasa.gov/MB06/ , last accessed April 2007).	31
Figure 4.	Illustration of Sigma coordinate method for resolving vertical levels in ocean models. This method follows the bottom topography and is more effective in coastal regions and over the continental shelf and slope. η represents sea surface height. Sigma coordinate systems are used by all three numerical models, the Harvard Ocean Prediction System (HOPS), Navy Coastal and Ocean Modeling (NCOM) and Regional Ocean Model System (ROMS) (From http://www.oc.nps.navy.mil/nom/modeling/index.html , last accessed April 2007).	32
Figure 5.	Illustration of z level coordinates. This type of vertical grid is more effective in the surface layers of the water column. η represents sea surface height (From http://www.oc.nps.navy.mil/nom/modeling/index.html , last accessed April 2007).	33
Figure 6.	This representation of hybrid vertical levels shows the sigma coordinates at the surface layer and the z coordinates in the deep water and away from abrupt topography. (From Dr. Julie Pullen, Marine Meteorology Division, NRL).	34
Figure 7.	ADCP moorings and MBARI M2 wind buoy locations near the Monterey Bay. Bathymetric contours in meters are shown by the color bar. The solid white line is the coastline.	35
Figure 8.	Wind vectors (top), across-shelf velocity contours (middle), and alongshore velocity contours (bottom) at ADCP 2.	36
Figure 9.	Wind vectors (top), across-shelf velocity contours (middle), and alongshore velocity contours (bottom) at ADCP 1.	37
Figure 10.	Spatial distribution of the surface wind at 30 m elevation as observed by the NPS Twin Otter Aircraft. The magnitude is shown by both the arrows and the color bar. The units are in m/s.	38
Figure 11.	Stick plot of the velocity vectors for (a) the wind from MBARI M2 compared with the stick plots for the (b) surface (10 m), (c) mid-depth (34	

	m) and (d) near-bottom (46 m) currents for ADCP 1. The sticks are plotted every six hours. Relaxations in the winds are denoted by R . Wind relaxation events are positive (poleward) and upwelling wind events are negative (equatorward). Poleward current is positive and equatorward current is negative.	39
Figure 12.	Stick plot of the velocity vectors for (a) the wind from MBARI M2 compared with the stick plots for the (b) surface (10 m), (c) mid-depth (34 m) and (d) near-bottom (46 m) currents for ADCP 2. The sticks are plotted every six hours. Relaxations in the winds are denoted by R . Wind relaxation events are positive (poleward) and upwelling wind events are negative (equatorward). Poleward current is positive and equatorward current is negative.	40
Figure 13.	Spatial distribution of the wind at 30 m altitude and sea surface temperatures as observed by the NPS Twin Otter Aircraft for a) August 3; b) August 4; c) August 7; and d) August 8, 2006. The magnitude of the wind is shown by the arrows and the sea surface temperatures are shown by the color bar. The units are in m/s.	41
Figure 14.	Time series comparing data from the two ADCPs. The black line is ADCP 1 and gray line is ADCP 2.	42
Figure 15.	Autospectra of the surface (10 m), mid-depth (34 m), and near-bottom (46 m) currents for ADCP 1. Note the energy difference between the across-shelf (top) and alongshelf (bottom) components.	43
Figure 16.	Autospectra of the surface (12.24m), mid-depth (52.24m), and near-bottom (72.24m) currents for ADCP 2. Note the energy difference between the across-shelf (top) and alongshelf (bottom) components.	44
Figure 17.	Across-shelf and alongshelf autospectra for the wind observations at MBARI Buoy M2.	45
Figure 18.	Coherence and phase plots between wind and current for surface (10 m), mid-depth (34 m), and near-bottom (46 m) currents for ADCP 1. A positive (negative) phase means wind leads (lags) the current. The red line indicates a 95% significance level for the coherence (From: Amos and Koopmans, 1963).	46
Figure 19.	Coherence and phase plots between wind and current for surface (12 m), mid-depth (52 m), and near-bottom (72 m) currents for ADCP 2. A positive (negative) phase means wind leads (lags) the current. The red line indicates a 95% significance level for the coherence (From: Amos and Koopmans, 1963).	47
Figure 20.	Coherence and phase plots for alongshelf wind and across-shelf currents for ADCP 1 and 2. A positive (negative) phase means wind leads (lags) the current. The red line indicates a 95% significance level for the coherence (From: Amos and Koopmans, 1963)	48
Figure 21.	Aircraft data during the relaxation event on 02-05 August 2006. There are stronger winds north of the cape and minimum winds at the mouth of the bay.	49

Figure 22.	Upwelling event from the 09-11 August 2006. Note the maximum of alongshore wind off Point Año Nuevo.	50
Figure 23.	Harvard Ocean Modeling System model output showing eddies, meanders, and other non-local events that affect the current flow. (From Lermusiaux, W.G., P.J. Haley, and W.G. Leslie, 2006: ASAP: adaptive sampling and prediction Monterey Bay 2006, Harvard University, from http://oceans.deas.harvard.edu/ASAP/index_ASAP.html , last accessed February 2007).	51
Figure 24.	Principle variance ellipses for the numerical models and ADCP 1 mooring data.	52
Figure 25.	Principle variance ellipses for the numerical models and ADCP 2 mooring data.	53
Figure 26.	Stick vector plots comparing surface currents at ADCP 1 with the four numerical models.	54
Figure 27.	Stick vector plots comparing mid-depth currents at ADCP 1 with the four numerical models.	55
Figure 28.	Stick vector plots comparing near-bottom currents at ADCP 1 with the four numerical models.	56
Figure 29.	Stick vector plots comparing surface currents at ADCP 2 with the four numerical models.	57
Figure 30.	Stick vector plots comparing mid-depth currents at ADCP 2 with the four numerical models.	58
Figure 31.	Stick vector plots comparing near-bottom currents at ADCP 2 with the four numerical models.	59
Figure 32.	Spatial comparisons between the numerical models and ADCP time series for surface currents at ADCP 1. The gray line is the model time series and the black line is the ADCP time series. The across-shelf components form the left column and the alongshelf components are on the right.	60
Figure 33.	Spatial comparisons between the numerical models and ADCP time series for mid-depth currents at ADCP 1. The gray line is the model time series and the black line is the ADCP time series. The across-shelf components form the left column and the alongshelf components are on the right.	61
Figure 34.	Spatial comparisons between the numerical models and ADCP time series for near-bottom currents at ADCP 1. The gray line is the model time series and the black line is the ADCP time series. The across-shelf components form the left column and the alongshelf components are on the right.	62
Figure 35.	Spatial comparisons between the numerical models and ADCP time series for surface currents at ADCP 2. The gray line is the model time series and the black line is the ADCP time series. The across-shelf components form the left column and the alongshelf components are on the right.	63
Figure 36.	Spatial comparisons between the numerical models and ADCP time series for mid-depth currents at ADCP 2. The gray line is the model time series and the black line is the ADCP time series. The across-shelf components form the left column and the alongshelf components are on the right.	64

Figure 37.	Spatial comparisons between the numerical models and ADCP time series for near-bottom currents at ADCP 2. The gray line is the model time series and the black line is the ADCP time series. The across-shelf components form the left column and the alongshelf components are on the right.....	65
Figure 38.	As in Figure 32, but with the series aligned better according to the cross-correlation results. The model output has been shifted forward/back according to the lag/lead estimated from the peak in the cross-correlation function.	66
Figure 39.	As in Figure 33, but with the series aligned better according to the cross-correlation results. The model output has been shifted forward/back according to the lag/lead estimated from the peak in the cross-correlation function.	67
Figure 40.	As in Figure 34, but with the series aligned better according to the cross-correlation results. The model output has been shifted forward/back according to the lag/lead estimated from the peak in the cross-correlation function.	68
Figure 41.	As in Figure 35, but with the series aligned better according to the cross-correlation results. The model output has been shifted forward/back according to the lag/lead estimated from the peak in the cross-correlation function.	69
Figure 42.	As in Figure 36, but with the series aligned better according to the cross-correlation results. The model output has been shifted forward/back according to the lag/lead estimated from the peak in the cross-correlation function.	70
Figure 43.	As in Figure 37, but with the series aligned better according to the cross-correlation results. The model output has been shifted forward/back according to the lag/lead estimated from the peak in the cross-correlation function.	71
Figure 44.	Optimal space/time lagged data producing the highest correlations and minimal rms error between the model output and the data at ADCP 1. For example, the alongshelf ROMS data was best at grid point 8, lagged back by 6 hours.....	72
Figure 45.	Optimal space/time lagged data producing the highest correlations and minimal rms error between the model output and the data at ADCP 1. For example, the alongshelf ROMS data was best at grid point 2, lagged back by 6 hours.....	73
Figure 46.	Optimal space/time lagged data producing the highest correlations and minimal rms error between the model output and the data at ADCP 1. For example, the alongshelf ROMS data was best at grid point 5, lagged back by 10 hours.....	74
Figure 47.	Optimal space/time lagged data producing the highest correlations and minimal rms error between the model output and the data at ADCP 2. For example, the alongshelf ROMS data was best at grid point 7, lagged by 0 hours.....	75

Figure 48.	Optimal space/time lagged data producing the highest correlations and minimal rms error between the model output and the data at ADCP 2. For example, the alongshelf ROMS data was best at grid point 7, lagged ahead by 22 hours.....	76
Figure 49.	Optimal space/time lagged data producing the highest correlations and minimal rms error between the model output and the data at ADCP 2. For example, the alongshelf ROMS data was best at grid point 9, lagged back by 7 hours.....	77

THIS PAGE INTENTIONALLY LEFT BLANK

LIST OF TABLES

Table 1.	Comparative table for the numerical models used during the ASAP project (From http://aosn.mbari.org/coop/ , last accessed February 2007).....	83
Table 2.	Means and standard deviations from the ADCP data. Statistics are reported as across-shelf, alongshelf.	84
Table 3.	Correlation values between ADCP 1 and ADCP 2. The italicized numbers are statistically insignificant and the lags (hrs) are reported as the second number in the across-shelf and alongshelf components.	85
Table 4.	Vector correlations for the cross correlation between ADCP 1 and ADCP 2. The magnitude describes the correlation between the two vectors while the orientation describes the angle between the vectors. A negative orientation indicates that ADCP 2 is to the right of ADCP 1.	86
Table 5.	Significant spectral peaks in the 5-10 day band from the cross spectra between the across-shelf wind and the across-shelf current and the alongshelf wind and the alongshelf current ADCP 1. A positive (negative) phase means wind leads (lags) the current. No data indicates no significant coherence in the 5-10 day band.....	87
Table 6.	Significant spectral peaks from the alongshelf wind and the alongshelf current at ADCP 2. A positive (negative) phase means wind leads (lags) the current. There were no significant periods in the across-shelf component.....	88
Table 7.	Significant spectral peaks from the cross spectra between the alongshelf wind and the across-shelf current for both mooring locations. A positive (negative) phase means wind leads (lags) the current. There were no significant periods at ADCP 1.	89
Table 8.	The grid point locations for the model/data comparisons. The ADCP is at grid point 5.....	90
Table 9.	Computed correlation values, RMS errors and lag times (hrs) for the NCOM model at ADCP 1. The shaded grid points are insignificant and the bolded numbers are the highest/optimal correlations in the grid.	91
Table 10.	Computed correlation values, RMS errors and lag times (hrs) for the NCOM model at ADCP 2. The shaded grid points are insignificant and the bolded numbers are the highest/optimal correlations in the grid.	92
Table 11.	Computed correlation values, RMS errors and lag times (hrs) for the ROMS model at ADCP 1. The shaded grid points are insignificant and the bolded numbers are the highest/optimal correlations in the grid. NaN (Not a Number) indicates no model output provided at that depth/location.	93
Table 12.	Computed correlation values, RMS errors and lag times (hrs) for the ROMS model at ADCP 2. The shaded grid points are insignificant and the bolded numbers are the highest/optimal correlations in the grid. NaN (Not a Number) indicates no model output provided at that depth/location.	94
Table 13.	Computed correlation values, RMS errors and lag times (hrs) for the HOPS Solo model at ADCP 1. The shaded grid points are insignificant	

	and the bolded numbers are the highest/optimal correlations in the grid. NaN (Not a Number) indicates no model output provided at that depth/location.....	95
Table 14.	Computed correlation values, RMS errors and lag times (hrs) for the HOPS Solo model at ADCP 2. The shaded grid points are insignificant and the bolded numbers are the highest/optimal correlations in the grid.	96
Table 15.	Computed correlation values, RMS errors and lag times (hrs) for the HOPS Nested model at ADCP 1. The shaded grid points are insignificant and the bolded numbers are the highest/optimal correlations in the grid.	97
Table 16.	Computed correlation values, RMS errors and lag times (hrs) for the HOPS Nested model at ADCP 2. The shaded grid points are insignificant and the bolded numbers are the highest/optimal correlations in the grid.	98
Table 17.	Calculated angles for the principle axis ellipses of each model and ADCP data for the individual mooring locations.	99

ACKNOWLEDGMENTS

I would like to acknowledge my thesis advisor Professor Steven Ramp for his direction, analysis assistance, and patience. Additionally, I would like to thank and acknowledge Mr. Fred Bahr for his MATLAB guidance, explanations, and overall support. I would like to thank Professor Collins for his additional assistance. A special thanks goes to my family, and roommate Kendra Crabbe, for their unconditional support and realistic perspectives. This thesis project could not have been completed without the patient aid of the above parties.

I would like to recognize the numerical modelers who were responsible for providing the output for this thesis comparison. Pierre Lermusiaux (MIT) with the HOPS model, Igor Shulman (NRLSSC) with the NCOM model and Yi Chao (JPL) with the ROMS model.

THIS PAGE INTENTIONALLY LEFT BLANK

I. INTRODUCTION

A. BACKGROUND

Due to its proximity to both the continental shelf and the Monterey Bay submarine canyon, the Monterey Bay provides a unique area for oceanographic research. The waters off the California coast are also part of the California Current System, a prominent eastern boundary current. Eastern boundary currents are generally linked to major upwelling systems with circulation patterns similar to those observed in the vicinity of the Monterey Bay. Wind forcing experiments have previously been conducted at areas north of the San Francisco Bay because the continental shelf there has comparatively uncomplicated bottom topography, and changes due to the large-scale wind stress can be identified (Winant et al., 1987).

In August of 2006 the Adaptive Sampling and Prediction (ASAP) experiment was launched in northern Monterey Bay. The major goals of the ASAP experiment were to use multiple observational assets and data assimilation in an attempt to gain the best insight into model predictive skill. First, autonomous vehicles including two types of gliders were deployed in patterns surrounding the Point Año Nuevo upwelling center. The mobility of the gliders makes them efficient sampling resources since they can observe the constantly changing ocean environment. These unmanned sampling devices can provide near-real time data as they sample the ocean. As the data are analyzed onshore, the paths of the gliders can be changed to sample interesting oceanic elements such as eddies and thermal fronts, a process known as adaptive sampling (Princeton ASAP Program, 2006). The real-time data were then assimilated into three separate numerical models focused on the Monterey Bay region. The overall goal is to have a system of data/model assimilations that produce predictions of oceanographic conditions with the smallest error.

This thesis project is designed to analyze data recorded by two Acoustic Doppler Current Profilers (ADCP) moored in an across-shelf configuration as part of the ASAP experiment. The ADCPs served as points of comparison between the moorings, autonomous vehicles, and model outputs. The data from these profilers were filtered,

rotated, plotted, and compared. The statistical analysis of the data helps to determine the effects of upwelling and relaxation events on the circulation of the water column north of the Monterey Bay. In particular, there is an episodic upwelling of cold water that historically appears there during the spring and early summer time frame. The data will also be compared with model nowcasts and forecasts from three ocean models associated with the ASAP experiment.

B. FUNDAMENTALS OF SHELF CIRCULATION

The area north of the Monterey Bay is a convenient area to conduct field work pertaining to wind forcing, since upwelling and relaxation events appear to be responsible for a good percentage of the coastal circulation in this region. The surface circulation in this area tends to be equatorward in the summer with evidence of eddies and meanders, tidal variabilities, and the local sea breeze (Ramp et al., 1997; 2005). Through data collected by the ADCPs and the model/data comparisons, research is conducted to observe the effects of wind forcing on the speed and direction of ocean currents. This project attempts to describe key aspects of ocean circulation mainly focusing on coastal upwelling and relaxation cycles. The upwelling process is important because it stimulates mixing, brings nutrients and dissolved chemicals to the surface layers, and contributes to surface water temperatures and productivity.

1. Wind Forced Circulation

The earliest contribution to understanding the wind forced circulation was made by oceanographer V. W. Ekman (Ekman, 1905). Within the surface boundary layer surface currents are directed 45° to the right of the wind. This forcing is propagated downward throughout the water column until the current has been rotated 180° clockwise from its starting direction. The decreasing magnitude of the downward rotating current is known as the Ekman Spiral. The depth at which the current direction is 180° from the surface vector is referred to as the Ekman depth. The Ekman transport is the integrated transport over the Ekman depth, and is directed 90° to the right of the wind. As a result the equatorward winds off the California coast transport surface water offshore during upwelling events (Figure 1). The offshore transport is balanced by onshore flow in the near-bottom layers.

Effects of wind forcing have been observed within the Monterey Bay and its vicinity. Strong upwelling favorable equatorward wind events lasting periods of two to three weeks are common during the upwelling season. These periods of strong winds typically lead to upwelling conditions and create a cyclonic circulation throughout the bay. Southward flow is found across the mouth of the bay, northwestward flow is found across the northern shelf, and the circulation is completed with eastward flow on the southern shelf (Ramp et al., 2005). The circulation becomes more chaotic and less defined during relaxations in the winds. Additionally, the California undercurrent flows poleward across the mouth of the Monterey Bay during these relaxations (Ramp et al., 2005).

The wind stress is typically effective in directly driving currents on the continental shelf due to the divergence of the Ekman transport at the coast and the shallow topography. The amount of correlation between the wind stress and circulation depends on a number of factors including the presence of a coastline, the bottom topography, and the wind near the coast as well as the presence of other significant oceanic features such as eddies or pressure gradients.

2. Upwelling Events

In general an upwelling event is characterized by colder bottom waters replacing warmer surface waters closer to shore, a process that occurs as the surface layer is forced away from the coast by the surface wind stress (Graham and Largier, 1997; Hickey, 1998) (Figure 2). In a relaxation event there is poleward or no wind. Wind relaxations can usually be observed in the alongshelf component of the current flow (Send et al, 1987).

Along a straight coast, this two dimensional process can be described in terms of a vertical and across-shelf direction. Offshore Ekman transport causes the isopycnals to slope upwards toward the coast and generates an equatorward alongshelf jet. The upwards slope is associated with a mean vertical shear in the alongshelf current flow (Huyer, 1984). Within the California Current System, the upwelled waters are saltier as well as colder. Mixing and vertical advection can also occur creating a homogenous/less stratified environment near the coast. This newly defined thermal structure also affects the equatorward direction of the current.

During a coastal upwelling situation the sea level at the coast will decrease. This change in sea level, reflected in the southward flow of the alongshelf surface currents, creates a barotropic pressure gradient directed eastward towards the coast (Huyer, 1984). At this point the current flow near the coast is consistently downwind and not following the direction of the Ekman spiral hence the transport is less than 45° to the right of the wind (Ekman, 1905). The total current is therefore the sum of the equatorward geostrophic flow, the baroclinic jet, and the Ekman flow. As depth increases offshore, the alongshelf currents often reverse to form a poleward undercurrent flowing in a direction opposite of the wind forcing (Kosro, 1987; Huyer, 1984). This circulation model is a typical result of coastal ocean dynamics.

Many field experiments focusing on shelf circulation along a straight coast line have been completed in the vicinity of the northern California continental shelf and slope. In 1981 and 1982 the Coastal Ocean Dynamics Experiment (CODE) successfully recorded two four-month data sets through two upwelling seasons with an emphasis on summer upwelling conditions. In relation to wind forcing, the CODE study found that the alongshelf wind is coherent with the currents and appears to have a direct effect on the direction of current flow and temperature change (Send et al, 1987). Conducted between Pt. Arena and Pt. Reyes, the CODE study took place in an area with the strongest upwelling favorable winds in the California Current System (Huyer, 1984). The CODE study discerned that the combination of the strengthening of the North Pacific high and the resulting colder surface temperatures of approximately 9°C announced the beginning of the upwelling season (Winant et al., 1987).

A variable coastline geometry with headlands results in a three-dimensional upwelling circulation. Vertical, across- and alongshelf directions are all considered in a three-dimensional model. In a three-dimensional cycle, the general mechanics of upwelling remain the same as compared to a two-dimensional cycle. The difference between the two is determined by the location of the colder upwelled water as a function of coastline topography. Recall in a two-dimensional upwelling cycle the colder water will be more or less evenly distributed along the straight coastline. In a three-dimensional situation with headlands, the upwelled water is concentrated in a general location off of the headland, often referred to as an upwelling center.

Upwelling centers are regions of locally intense upwelling, which have been observed at several locations along the west coast of the United States. These regions have a characteristic “tongue” of cold water extending from the coast to several hundred kilometers offshore (Kosro, 1987). A decrease in surface temperature results in diminished vertical temperature, and corresponding density gradients over the continental shelf (Winant et al., 1987). Observing and understanding the properties of the water column will determine how the circulation in an upwelling situation is altered by outside forcing.

There are two major upwelling centers in the Monterey Bay region, located to the south at Point Sur (Breakers and Mooers, 1986) and to the north at Point Año Nuevo. While Point Sur is a larger, more energetic upwelling center, this experiment focused on the upwelling center at Point Año Nuevo due to its closer location to Santa Cruz and Moss Landing. The cold waters from the Point Año Nuevo center have been observed to flow south and circulate within the Monterey Bay region, thus impacting local upwelling and temperature gradients. Specifically in the Monterey Bay region cold water first appears in the north but eventually spreads southward as a result of the wind (Rosenfeld et al., 1994; Ramp et al., 2005).

The Monterey Bay region experiences coastal upwelling for approximately six months from March through August. The northern California seasonal upwelling begins following the annual spring transition that occurs when the large-scale wind becomes equatorward during the spring (Hickey, 1998). The six-month upwelling season can be classified into three different phases. In March when the upwelling season begins the Monterey Bay is characterized by surface waters near 13 °C, a slight indication of surface warming, and low salinities (Graham and Largier, 1997). Colder waters (<10.5 °C) and higher salinity values (>33.7 psu) are indications of the peak of the upwelling cycle occurring during April through June (Rosenfeld et al., 1994). Towards the end of the season, July through September, warmer temperatures (13-16 °C) are observed in the Bay (Graham and Largier, 1997).

3. Wind Relaxation Events

In the northern California shelf region, relaxation events occur throughout the spring-summer upwelling season. It is intuitive to conclude that relaxation events are the

reverse of upwelling events. If this were an accurate situation then when the upwelling winds stop the warmer water that was dislocated offshore would move back to its initial position closer to the coast and the sea level would increase. This, however, does not always happen.

During a wind relaxation event, warmer less saline water appears along the coast (Ramp et al., 2005; Rosenfeld et al., 1994). Even though the dominant process is not fully understood the appearance of warmer coastal waters after a relaxation event can be related to alongshelf advection or surface heat fluxes. As a result of this change, the isotherms and isohalines that were sloped upwards to the coast in the upwelling event adjust to a more level state. In this case across-shelf advection and flow do not contribute to the increased warm waters observed during relaxation events (Send et al., 1987).

In the Monterey Bay region, relaxation events are observed more frequently and have longer time periods towards the later part of the season (July and August). Prolonged relaxation events tend to result in shoreward movement of the California Current into the Monterey Bay causing low salinity values and warmer water temperatures varying around 15 °C (Graham and Largier, 1997). Previous studies of the Monterey Bay region have also observed rapid onshore advection of warmer waters combined with surface warming as far inshore as the beginning of the Monterey Submarine Canyon (Rosenfeld et al., 1994).

C. OVERVIEW OF MODEL SPECIFICATIONS

Another important aspect of the ASAP experiment was to evaluate the importance of data assimilation to numerical predictions. The three models used during the ASAP study were the Harvard Ocean Prediction System (HOPS) (Robinson, 1999), the Regional Ocean Modeling System (ROMS) (Schepetkin and McWilliams, 2004), and the Navy Coastal Ocean Model (NCOM) (Shulman et al., 2002). A comparative table of the numerical models is included for reference (Table 1). These nested mesoscale models were adapted to the area of interest off Point Año Nuevo just north of the Monterey Bay. Even though the three numerical models are designed to predict the same variables, there are many factors that can cause differences in the outputs. Each model has a different domain and set of initial conditions used to set up the model. These domains are designed

to encapsulate the oceanic/atmospheric conditions of the particular area of interest. One-way nested models, such as the NCOM and ROMS models, have larger domains that provide boundary conditions for the smaller areas of interest (Figure 3). The ROMS model uses a triply-nested domain which covers the west coast, central California coast, and the Monterey Bay at 15 km, 5 km and 1.6 km resolution respectively (Jet Propulsion Lab, 2006) (Figure 3). Whereas one-way nested models only communicate from the larger domain to the smaller area of interest, two-way nested models can share boundary influences both ways between nests. The HOPS model in particular is two-way nested in a local scale model whose largest domain only covers an area between the Monterey Bay and San Francisco Bay. There were two separate HOPS runs used for comparison. The HOPS Solo model has 1.5 km resolution and the HOPS Nested model is a two-way nest with 1.5-0.5 km resolution. The two HOPS models also use different bottom friction parameters.

Most oceanographic models use one of three coordinate systems to resolve the water column. Sigma coordinate models use vertical coordinates that follow bottom bathymetry. The sigma coordinate method is more effective in complex topographic situations, coastal regions and over the continental shelf. To most effectively map the water column, sigma levels are typically closely spaced near the surface and/or bottom (Figure 4). This separation scheme allows for improved resolution of the boundary layers (Chassignet et al., 2002). The HOPS model uses 30 sigma levels to resolve the water column from surface to bottom. They are most effective in the surface mixed layer because they are capable of providing the high resolution needed to represent 3D turbulence (Chassignet et al., 2002). The z coordinates use a predetermined number of depth levels to resolve the water column and do not provide accurate resolution in areas with sloping topography (Figure 5). There is also another method, which involves a hybrid system between the sigma and z levels to obtain the most effective representation of the water column. These models use sigma coordinates in the upper ocean and z coordinates in the deep ocean and away from abrupt topography (Figure 6). In this study all three models used the sigma coordinate system. The ROMS model uses 32 sigma levels and the NCOM model uses 30 sigma levels.

Mixing is one of the most critical modeling aspects to consider because it provides significant differences between model outputs. It is necessary for a model to use an accurate range of mixing parameters. Too little mixing could cause a model to crash, while a large mixing parameter could produce model outputs that are too smooth. Due to the nature of this study and the focus on upwelling and relaxation events, mixing plays a large role in the model output. The NCOM model used the most common mixing scheme- the Mellor-Yamada 2.5 scheme, while the ROMS model used the K-Profile Parameterization. The HOPS model used a two-mode scheme involving a top layer that incorporates wind stress and Ekman depth and a bottom layer that is based on the local gradient Richardson number.

In addition to mixing, models must also have a starting point. Each model has its own set of initial conditions for the predicted/output variables. The HOPS model used recent conditions from the local area to form initial conditions, while the ROMS and NCOM models used climatology that was forced by the Coupled Ocean Atmosphere Mesoscale Prediction System (COAMPSTM). Generally, the background climatic information is entered into the models during the spin-up process. Spin-up describes the amount of time needed for a model to reach a state of statistical balance under forcing. This process builds a historical climatic reference of the region of interest and the surrounding area. Depending on the purpose and goals of the model the spin-up process can vary in time, the amount of included historical information, and the type of climatologic database. The ROMS model had a significantly longer spin up time, starting in July of 2003, than the NCOM and HOPS models started in July 2006. All three models used COAMPS data to define air-sea heat flux parameters as well as surface wind stress parameters. The ROMS model used the COAMPS data for wind information and used the Large and Pond drag coefficient to compute the wind stress (Large and Pond, 1981).

In an effort to provide the most accurate prediction, there are different data assimilation techniques utilized by models. The fundamental idea of data assimilation is to incorporate real data into the simulated ocean system that is predicted by the model. This is achieved by identifying the correlation scales, determining the correct amount of influence the real data retains, and finally applying the accurate amount of change to the

model output. Data assimilation is a delicate process since adjusting one predicted parameter in accordance with the real data will have a ripple effect on the remaining variables in the model output.

The three models in this study apply three separate methods of data assimilation within continuous assimilation schemes. An assimilation window describes the regularity of the data assimilation. The HOPS and NCOM models used twelve-hour updates while the ROMS model used six-hour updates. All three models assimilated temperature and salinity from the gliders and sea surface temperatures from the aircraft. ROMS additionally assimilated satellite sea surface temperatures and temperature and salinity from MBARI moorings M1 and M2. The NCOM model did not apply satellite data but used temperature and salinity profiles along with sea surface temperatures from the Modular Ocean Data Assimilation System (MODAS) (Summary of Three Ocean Models, 2006).

THIS PAGE INTENTIONALLY LEFT BLANK

II. DATA COLLECTION

A. ACOUSTIC DOPPLER CURRENT PROFILERS

Current information for the 2006 circulation experiment was recorded using two bottom-mounted Teledyne RD Instruments Sentinel Workhorse 300 kHz ADCPs. Located at $36^{\circ} 55.336'N$, $122^{\circ} 07.344'W$, ADCP 1 was placed in shallower water of 54 meters. ADCP 2 was located at $36^{\circ} 53.683'N$, $122^{\circ} 11.244'W$ at a depth of 92 meters (Figure 7). The moorings were located 6.55 km apart. The wind time series was recorded by buoy M2 located in the Monterey Bay and maintained by the Monterey Bay Aquarium Research Institute (MBARI). Buoy M2 rather than M1 was used for the ASAP experiment as its location farther offshore was more representative of the winds at ADCP 1 and 2. Bottom-mounted moorings are advantageous because they have no extraneous movement, and allow faster sampling and less averaging than a surface mooring. The ADCP is capable of recording the data in four-meter bins up to the surface of the water; however, the sidelobes reflect from the surface and contaminate the first three bins. The ADCP has a correlation magnitude feature that allows it to determine when the recorded data is good or not.

The ADCP uses a multiple beam system to obtain an accurate observation of current velocity. The current profilers are designed to sample the water column every second from four separate beams on a 20° slant. Since only three beams are required to evaluate velocity, the fourth beam serves as a way to assess the quality of the data (Teledyne RD Instruments, 2007). Three beams resolve the x,y,z directions while the fourth beam allows computation of the error velocity, the difference between two vertical velocity estimates. This fourth beam is designed to assess accuracy, reliability, and quality of the data (Teledyne RD Instruments, 2007).

The ADCPs were used for data collection over a one-month period. Data were continuously collected and an ensemble was created as the one-second samples were averaged over a one-minute period. The ADCPs were programmed to send back the most recent estimate via satellite link, every 10 minutes.

B. COORDINATE ROTATION

To ease analysis, the principal axis technique was used to rotate the raw wind and ADCP data. Rotating the data separates the u and v components into across- and alongshelf components. This method of rotation ensures that a minimum of the alongshelf flow will be translated into the across-shelf flow (Kosro, 1987). The principal axis rotation agreed with the local orientation of the bathymetry and yielded angles of 58° for ADCP 1 and 48° for ADCP 2.

C. DATA FILTERING

The raw recorded data from both ADCP mooring sites were truncated and checked for errors. Once the data were transcribed into a form useable by MATLAB, they were filtered on three different time scales to include energy with periods less than five hours for internal waves, periods between five and thirty-three hours for tidal and inertial motions, and greater than thirty-three hours for wind forcing, mesoscale events, and mean currents. These different filtering bands allow different ocean phenomena to be observed in the plotted outputs. Time series plots were used extensively throughout this research for data analysis. Additionally, the filtered and rotated across-shelf and alongshelf component plots and color contours were also generated using MATLAB. These plots aid in interpreting statistical computations of the data. Autospectra were used to show the distribution of energy as a function of frequency and coherence and phase were computed between wind and currents as well as between the time series from the two ADCP moorings.

III. DATA ANALYSIS

A. MEAN FLOW

In order to achieve an accurate understanding of the circulation, it is necessary to analyze different depths of the water column. Table 2 outlines the depths used for the two moorings. As previously mentioned, the near-surface depth is not directly at the surface due to sidelobe interference. The near-bottom depth for ADCP 2 represents the deepest depth provided by all four models.

The mean currents at ADCP 1 were all poleward. The surface flow (2.05 cm/s) was less than the subsurface flow (4.84, 4.19 cm/s) due to the opposing equatorward wind stress. The across-shelf means were small, less than 1 cm/s. At ADCP 2 the surface mean was equatorward (-6.68 cm/s), the bottom was poleward (1.69 cm/s) and the mid-depth mean was near zero. The across-shelf means were similar to ADCP 1, less than 1 cm/s. The standard deviations at ADCP 2 were about double ADCP 1, indicating much larger current fluctuations there (Table 2).

B. VISUAL ANALYSIS

The velocity contours show significant flow variations within the water column. Three poleward flow events can be clearly observed. ADCP 2 showed strong poleward flow starting on 03 August and lasting to 08 August (Figure 8). This four-day event resulted in strongest flow between 05 and 06 August and occurred partially during a wind relaxation event. Poleward current flow may also be associated with alongshelf pressure gradients and mesoscale variabilities. The poleward event starts earlier than the wind relaxation event hence this strong forcing could be a coincidence or a combination of the wind relaxation and other oceanic processes. Additionally, there were two visibly weaker poleward flow events that took place later in the month during equatorward winds. These events appear to be more affected by remote forcing versus local forcing

The first poleward flow at ADCP 2 appears to lead a weaker flow event at ADCP 1 by about one day (Figure 9). This is indicative of an oceanic process that could be moving onshore such as an eddy or front. Additionally, shorter spatial and temporal scales were observed in across-shelf components at both mooring locations indicating evidence of wind forced currents in the surface layer.

Before analyzing the directional effects of the winds and currents it is necessary to discuss the differences in current magnitude at the individual mooring locations. The upwelling winds are on the order of 5 m/s and occur at the same time as currents on the order of 5-10 cm/s at ADCP 1 and in excess of 15 cm/s at ADCP 2. There are several possible explanations to consider concerning the stronger current flow at ADCP 2. Firstly due to location, ADCP 2 was located closer to the center of the upwelling jet where ADCP 1 was located farther inshore of the jet. A second possible reason for increased flow rates is related to the offshore increase in the wind stress, causing more wind stress at ADCP 2 than at ADCP 1. This spatial variation was observed in the aircraft data, for instance on 01 August 2006 (Figure 10).

The stick vector plots clearly show the strong poleward flow from 03 August to 08 August (Figures 11 and 12). After comparing with the wind events, it becomes clear that a wind relaxation occurred during a shorter time frame than the poleward flow. The wind relaxation is also consistent with the aircraft data taken during the experiment. Small or poleward wind velocities are evident on 03-04 August (Figure 13). It is evident at both mooring locations that the poleward current leads the relaxation event. As the time series progresses, both mooring sites show a transition day on 07 August where upwelling favorable winds start in the north and the flow of the poleward currents start to decelerate. Again this transition was also apparent on the aircraft data. Figure 13c shows the beginning of the equatorward wind shift. By 08 August, the aircraft data indicates strong equatorward upwelling favorable winds consistent with the stickplots (Figure 13d). Around 09 August the currents become equatorward thus following the southward wind events indicative of an upwelling situation.

A wind reversal was observed around 14 August but there was no significant visible change in the currents at any depths at either mooring. Lack of reversals in the

water column can be related to the required response time between currents and wind. It is observed that the current weakens only to increase again around 16 August in relation to the upwelling wind event. Equatorward flow was observed at both mooring sites and appeared to be stronger in the surface currents than the mid-depth or near-bottom currents for both ADCP 1 and 2 (Figures 11 and 12). A weak relaxation event on 18 August was followed by a poleward shift of the current. Despite strong upwelling winds, this poleward shift appears to dominate the next ten days at both moorings. It is interesting to note that the upwelling winds are the same strength (5 m/s) as they were on 08 August when they were accompanied by an equatorward flow. As observed at both mooring locations, the poleward flow from 18 August to 28 August was not as strong as previous flows. Late in the summer, there is often a poleward flow that is associated with an alongshelf pressure gradient force.

The wind time series showed an upwelling event that began on 26 August and continued to the end of the time series. At ADCP 1 the surface currents showed weak equatorward flow that was less than 5 cm/s (Figure 11). The mid-depth and near-bottom currents showed no immediate change from poleward to equatorward flow until 30 August. After the currents switched, the equatorward flow was weak, roughly 2 cm/s. There is also some previous evidence that the poleward pressure gradient force increases with the season (Ramp and Abbott, 1998). At ADCP 2, the flow at all three depths clearly became equatorward and followed the upwelling favorable wind (Figure 12). Overall, it appears that there was a stronger response at ADCP 2 to the wind forcing than ADCP 1.

C. CROSS CORRELATIONS BETWEEN MOORING LOCATIONS

Vector and scalar correlation values were calculated between ADCP 1 and ADCP 2. Individual comparisons of the time series plots show that there are higher correlations associated with the alongshelf component than with the across-shelf component. In the alongshelf component, correlation increased proportionally with depth. Table 3 displays the cross correlation coefficients for the maximum across-shelf and alongshelf values as well as the respective significance levels for the three indicated depths. There is strong

correlation in the alongshelf components, while the across-shelf components show lower or statistically insignificant correlations, and additionally, appear more out of phase. These results are consistent with the time series plots of the mooring data (Figure 14).

Significance levels were calculated following Amos and Koopmans (1963) using degrees of freedom estimates derived by Davis (1976). The effective degrees of freedom, N_{eff} , is defined as

$$N_{eff} = N / \tau_n$$

where

$$\tau_n = \sum_{i=-\infty}^{\infty} C_0(i\Delta t)C_n(i\Delta t)\Delta t$$

is the correlation time scale for the data. N_{eff} provides the degrees of freedom used in the computational process to determine if the individual correlations between the time series were statistically significant with a confidence interval of 95%. Fewer degrees of freedom correspond to more self-correlated data and therefore higher significance levels. Due to the lower significance levels of the across-shelf component, only the mid-depth correlation was found to be insignificant (Table 3).

Vector correlation is a technique that enables the average correlation and angular displacement between a pair of two-dimensional vectors to be resolved (Kundu, 1975). The magnitude describes the overall correlation of the vector while the phase angle describes the average counterclockwise angle of the second vector in relation to the first (Kundu, 1975). Upon examination of the vector correlations at the mooring locations it becomes evident that the vectors were well aligned and the correlation increased as depth increased (Table 4).

D. SPECTRAL ANALYSIS

Spectral analyses were completed to look at the time series in relation to frequency. A linear detrend method was used to give the most realistic distribution of the spectral energy. Five overlapping pieces of the time series were used to resolve a period of ten days. An hourly sampling interval and a confidence interval of 95% were used.

During the principal ellipse coordinate rotation process, energy was transferred from the east and north components into the along and across-shelf components. This process resulted in an order of magnitude more energy in the alongshelf components in comparison to the across-shelf components (Figures 15 and 16). The alongshelf autospectra show that the only significant points at the 95% confidence level are the five and ten day periods and the tidal bands. The alongshelf autospectra for ADCP 2 also reveals an unambiguous inertial peak. This wind-generated peak is most visible in the mid-depth and near-bottom spectra. An inertial peak describes the primary frequency at which wind pumps energy into the ocean. The inertial period is calculated using the formula below for T_i where ϕ is latitude.

$$T_i = \frac{12}{\sin(\phi)}, \text{ (hrs)}$$

The inertial period for this latitude is 20.16 hrs and falls between the 12 and 24 hour tidal peaks. This inertial period is more visible at ADCP 2 than ADCP 1, indicating stronger wind forcing further offshore (Figures 15 and 16). The inertial oscillations at ADCP 1 may also be inhibited by the coastline. The diurnal tidal peak is sometimes broader than the semidiurnal peak at the surface with a less discernible inertial peak. Due to the complexities of the surface environment, some of the inertial motions in the surface currents is included with the broad diurnal peak. The autospectra of the near-bottom currents resolve the inertial peak in addition to both tidal peaks.

The autospectra for the alongshelf and across-shelf wind were also computed (Figure 17). The magnitude of the across-shelf component was also smaller, by almost two orders of magnitude, than the alongshelf wind spectrum. The diurnal sea breeze peak is evident in both the across and along shore spectra. Consistent with the ADCP autospectra, the wind spectra also show the same significant five and ten day periods.

E. COHERENCE AND PHASE CALCULATIONS

The final numerical analysis applied to the wind and current time series was a test for coherence and phase. Similar to the autospectra, coherence and phase outputs are a

function of frequency. Coherence and phase were calculated between each station (ADCP 1 and 2) and with the respective across-shelf and alongshelf wind components. The lag time was calculated using the following equation.

$$\left(\frac{\theta}{360^\circ} \right) \times period (hrs)$$

where θ is the phase angle.

Figure 18 depicts the coherence and phase between the alongshelf wind and alongshelf current, and the across-shelf winds and across-shelf current at ADCP 1 at each depth. The straight horizontal line on the coherence plot indicates the 95% significance level. While randomly significant, information with frequency higher than 10^{-1} is considered noise. Based on the autospectral analysis only primary wind-band periods of 5-10 days were considered for further study. At ADCP 1 there is evidence of surface coherence with a phase angle of 21° corresponding to a lag time of 14.9 hours (Table 5). Significant coherences were additionally observed at both the mid-depth and near-bottom currents in the alongshelf component.

Contrary to ADCP 1, there were no significant wind-band periods in the across-shelf components at ADCP 2 (Figure 19, Table 6). There were however significant coherences in all three depths of the alongshelf component at ADCP 2. The mid-depth and near-bottom currents have similar phase angles and lag times, however the surface current has a larger phase angle and lag time (Figures 19 and 20).

The coherence and phase was also analyzed between the alongshelf wind and the across-shelf current. Explained by ocean dynamics and air sea interactions, the alongshelf wind forces the across-shelf current near the surface. This case was studied to discern any Ekman-type flow. Focusing on the 5-10 day period there was significant coherence at the surface and near-bottom currents at ADCP 2 (Table 7). Both the 5.16 day and 10.31 day periods were calculated for the surface currents with matching phase and lag times. The near-bottom current was also significant at 10.31 days but with opposite phase. There

was no significant coherence for any period in the mid-depth (Figure 20). This result can be directly related to Ekman dynamics. The response to the wind was offshore at the surface, onshore at the bottom, with weak flow in between.

F. RESPONSE OF SHELF CURRENTS TO WIND EVENTS

As seen clearly in the aircraft observations, there was submesoscale variability in the offshore wind distribution. During the relaxation event in the beginning of the month there are stronger winds north of the cape and a wind minimum at the mouth of the Bay (Figure 21). During the upwelling events starting on 08 August, all aircraft observations show an alongshelf wind maximum off Point Año Nuevo. There is also a wind maximum at Point Año Nuevo during the upwelling event from the 09-11 August (Figure 22). This may account for the formation of an upwelling center there. Consistent with previous studies, there was a wind shadow behind the coastal mountains in the northeast corner of the Monterey Bay (Graham and Largier, 1997; Ramp et al., 2005).

The auto and cross-spectral analysis demonstrated some wind/current interactions with the alongshelf wind and the across-shelf current. There were diurnal and semidiurnal peaks present as well as indications of wind generated inertial peaks. These peaks display some local wind/sea interactions in the time series. As usual on the continental shelf more coherence was found between the alongshelf wind and currents than between the across-shelf wind and currents.

Based on the four completed analyses (visual, spectral, correlations and coherence and phase), it is evident that the currents appear to be forced by both wind and non-local events such as eddies, meanders, and the alongshelf pressure gradient. As previously noted, there is some previous evidence that the poleward pressure gradient force increases during the progression of the upwelling season (Ramp, et al., 2005). Since this study was completed in August, towards the end of the upwelling season, there is reason to believe that the poleward pressure gradient force is responsible for the observed poleward flow. This pressure gradient is driven by a combination of two oceanic phenomena. Warmer waters to the south, near Point Conception, result in higher coastal sea levels there thus creating a pressure gradient from the high sea surface levels in the

south to the lower sea surface levels in the north along the West Coast. This pressure gradient results in a poleward flow up the coast. Another aspect of this poleward flow is related to the stronger upwelling favorable winds located in the north. Stronger winds tend to set down the sea level more in the north causing a higher sea level in the south and a similar situation ensues, a pressure gradient is formed with resulting poleward flow. Both the upwelling favorable winds in the north and the warmer sea surface temperatures in the south contribute to the poleward flow. This is evident in the data, particularly at the end of the month. The wind is clearly upwelling favorable but the current flow is poleward.

Given the observations it appears logical that the wind forcing would affect the current flow. This hypothesis could be more clearly demonstrated in an environment that is not interrupted by eddies and meanders and most likely influenced by the California Current (Figure 23). Figure 23 is an example of model outputs for the area of interest clearly depicting eddies and other oceanographic phenomena that could also affect the current flow. Previous studies have also cited that the California Current meander could also affect circulation patterns in the Monterey Bay region (Ramp et al., 2005; Rosenfeld et al., 1994). Overall, an important result of this study is that both local and remote forcing were active on the continental shelf near Point Año Nuevo.

IV. MODEL/DATA COMPARISONS

A. DATA PROCESSING

Accurate modeling of the ocean circulation is of high interest to oceanographers and the Navy. Another aspect of this project is to analyze comparisons between the data from the ADCP moorings and three numerical models that are designed to formulate current predictions for the continental shelf and Monterey Bay. As discussed earlier, the model outputs used for comparisons are from the ROMS model, the NCOM model and the HOPS model. In order to build a basis for comparison, the time series from all three models underwent the same low frequency filtering and coordinate rotation as the time series from the ADCPs. Once completed these procedures had similar effects on the across and alongshelf components of the model outputs. Physically constrained by the coast, the across-shelf component is naturally weaker. Therefore, the models show more energy in the alongshelf direction, similar to the results from the ADCP rotation.

Oceanographic models are able to predict the currents over an area that is significantly larger than the ASAP region. The best way to organize the model data is to examine the temporal and spatial errors of the model relative to the observed time series. A uniform grid of model output was chosen to account for spatial variability surrounding each mooring (Table 8). The center point of the grid corresponds to the ADCP location. A temporal analysis was completed using time lags at the center point while a spatial analysis was completed by comparing the ADCP data with the surrounding model grid points.

In order to quantify the visual analysis it was necessary to compute the correlation coefficients between the time series of the ADCP and model data. The normalized correlation values, by definition between -1 and 1, indicate how well the model data matches the ADCP data. The lag (hours) indicates the temporal mismatch between the two time series. For well behaved functions, the optimal cross correlation value will be a high positive number at a small lag indicating highly correlated sequences. Negative correlation values indicate that the time series are 180° out of phase at the given lag. A

positive lag time indicates that the data leads the model. As the time series are temporally aligned the difference between the curves should become smaller both visually and statistically.

The correlation coefficient calculated from the normalized cross covariance function is used to compare the model and the data time series. (Bendat and Piersol, 1986). It states that dividing the cross covariance (C_{xy}) by the variance ($\sigma_x \sigma_y$) of both sequences will yield the linear dependence between the two series x (model) and y (ADCP data) (Bendat and Piersol, 1986).

$$\rho_{xy}(\tau) = \frac{C_{xy}(\tau)}{\sigma_x \sigma_y}$$

$$-1 \leq \rho_{xy}(\tau) \leq 1$$

where $\rho_{xy}(\tau)$ is defined as the correlation coefficient (normalized cross-covariance function) between x and y , $C_{xy}(\tau)$ is the cross covariance between x and y , σ_x , σ_y are the variances of series x and y , and τ is the lag.

The root mean square (rms) error describes the mean offset (cm/s) between the model time series and the data time series. The root mean square error is the square root of the sum of the individual squared errors and is defined as

$$rms \ error = \sqrt{[\hat{\Phi} - \Phi]^2}$$

where $\hat{\Phi}$ is the estimated value (model time series) and Φ is the true value (ADCP time series).

The reported rms value is the rms value associated with the maximum correlation at each grid point (Tables 9-16). Mathematically the lagged rms will generally be smaller than the original rms, assuming the lag created an improvement.

For each grid point the maximum correlation, its lag time, and the rms error between the model and data were recorded for both the across-shelf and alongshelf components. The statistical significance of the correlations was also calculated based on

the degrees of freedom. The calculation for the degrees of freedom was derived by Davis (1976) and was described in more detail in the wind and current correlation statistics section. These parameters indicate which grid points are legitimate and should be considered, as well as those correlations that are insignificant.

B. NUMERICAL MODEL ANALYSIS

In line with the goals of the ASAP experiment, results from the three associated numerical models were compared to the data from the ADCP moorings. Three comparison techniques were used: the principal axis ellipses give estimates of the low frequency alignment between the models and the moored time series. Stick vector plots provide an intuitive approach and show differences in the magnitude and direction of the flow. Finally the along and across-shelf components were used in conjunction with the statistical calculations to determine model accuracy based on correlation coefficients, rms error and lag time.

1. Principal Axis Ellipses

Before the data were filtered all of the time series were rotated based on the principal axis technique. Differences in length are considered discrepancies in estimates of magnitude while differences in width describe inconsistencies in the energy distribution between the alongshelf and across-shelf components. The principal axis ellipses show that there was more horizontal shear in the water column than the models predict. The lengths of the model ellipses are generally the same at ADCP 1 and ADCP 2 while the mooring data ellipses increased in length at ADCP 2 (Figures 24 and 25).

The green ellipses, representing the NCOM predictions show the model overestimated by approximately 2 cm/s relative to the remaining models and the moored data at ADCP 1 (Figure 24). At ADCP 2 the NCOM model underestimated and showed a misalignment with respect to the mooring data (Figure 25). The NCOM ellipse (-57.2°) was aligned outside of the ADCP envelope (-49.5°); where as the other models were more evenly aligned within the ADCP envelope (Table 17). The error from the misalignment in the NCOM ellipse is seen in subsequent analyses. The HOPS nested (HOPSn) model appears to have the best alignment at both mooring locations. The ROMS model shows a

clear misalignment (-69.5°) at ADCP 1 and slightly improved alignment (-57.5°) at ADCP 2. The HOPS solo (HOPSs) model predicted significantly more energy in the across-shelf direction than the other models and mooring data.

2. Stick Vector Plots

Stick vector plots were created to provide a concise analysis of the magnitude and direction of the predicted current. The currents at the mooring locations may be divided into three general flow patterns. There was a poleward flow from 01-09 August, an equatorward flow from 09-18 August and the remainder of the month (18-31 August) was mixed but generally poleward flow. The exception was near the surface at ADCP 2.

In the beginning of the time series at ADCP 1, NCOM shows weak variable flow at the surface and poleward flow at deeper depths (Figures 26, 27 and 28). NCOM underestimates the first poleward flow event but badly overestimates the second two events (15-31 August). Additionally, at ADCP 1 NCOM predicts poleward flow patterns from 09-12 August with observed currents that were equatorward. The ROMS model shows an initial poleward flow at all three depths. These initial similarities could be related to a longer spin-up process. The model does not however predict the equatorward flow from 09-11 August. Although the flow for the second two events are slightly overestimated, the ROMS predicted patterns appear to be more similar to the flow patterns of the ADCP 1 data than NCOM.

At ADCP 1, the predictions from the HOPSn model shows the most correlated flow patterns with slight overestimates in current magnitude in the surface currents and improvements with depth. There appears to be too much poleward flow at the beginning of the month (01-02 August) which could be related to initialization problems or problems associated with the data assimilation.

All three depths of the HOPSs model at ADCP 1 show a strong initial poleward flow. The model predicts only poleward flow in the surface currents throughout the entire time series. The strength of the poleward flow is decreased with depth resulting in improved agreement near the bottom. Similar to ROMS and NCOM, HOPSs does not predict the equatorward flow in the middle of the time series.

NCOM's current predictions for ADCP 2 were often opposite from the observed flow at the surface (Figures 29, 30 and 31). Flow agreement improved in the mid-depth and near-bottom currents. Consistent with ADCP 1 results, NCOM overestimated the poleward flow from 15-31 August. This may be improved in a subsequent version of the model (I. Shulman, personal communication, 14 February 2007). In the beginning of the time series ROMS surface predictions were orientated in the same direction as the observations although the flow patterns at the mid-depth and near-bottom were all poleward. After 18 August, the ROMS model was anti-correlated with the surface currents but the model shows slight improvements with depth. The predicted mid-depth and near-bottom currents show flow patterns that are opposite to and larger than the ADCP flow and do not predict the equatorward event.

At ADCP 2 the current magnitude and direction of the HOPSn model appear to be the closest match to the mooring data. At the surface, the HOPSs model shows reasonable predictions. At the deeper levels the model does not predict the poleward flow. The magnitudes are overestimated and the flow direction is misaligned. There also appears to be too much energy in the across-shelf component, a result consistent with the principal ellipse analysis.

3. Components and Statistical Analysis

In terms of spatial and temporal variability, the across- and alongshore component plots and statistical analysis provide a more quantitative method for comparing the models and ADCP data. The correlation coefficients, lag times, and rms errors between models and observations provide an overall picture of model accuracy. The calculated values are presented in tables for each model at both ADCP mooring locations (Tables 9-16). The focus of these time series will be primarily in the alongshelf component as the across-shelf correlations were generally statistically insignificant. To determine geographical offset between the model and ADCP mooring locations, model output from the grid points surrounding each ADCP were compared with the data in addition to the grid points co-located with the ADCP.

The comparisons at the center grid points with ADCP 1 were consistent among three of the models (Figures 32, 33 and 34). The ROMS and both HOPS models showed the same pattern of decreasing correlations with depth and smallest RMS error values in

the near-bottom currents (Tables 12-16). All depths of the alongshelf component of the NCOM model were found to be statistically insignificant (Table 9). The time series for the center point at ADCP 2 show high correlations between HOPSn, HOPSS and ROMS (Figures 35, 36 and 37). The NCOM model does not appear to be as in sync with the ADCP data as the other models. Recall that the principal ellipse for NCOM at ADCP 2 indicated over-estimates. The ROMS and both HOPS models had high correlation values on the order of 0.6 to 0.8 (Tables 12-16). Both HOPS models however showed highest correlations at the surface (0.88 for HOPSn and 0.77 for HOPSS). Additionally, the HOPSS model shows the smallest RMS error (8.15 cm/s) at the surface while the smallest RMS error for HOPSn (6.25 cm/s) was found at the near-bottom depth.

Better agreement can be visually observed at both mooring locations when the time lags are accounted for (Figures 38-43). At ADCP 1, ROMS had the smallest lags and the both HOPS models showed comparable lag times while NCOM had the largest lag times (Figures 38, 39 and 40). The lag times for the ROMS model were all positive indicating that the data leads the model. NCOM and both HOPS models had negative lag times indicating the model leads the data.

There was slightly more temporal offset at mooring 2 (Figures 41, 42 and 43). Although ROMS again had the smallest lags, the surface currents predicted a positive lag while the mid-depth and near-bottom currents showed negative lags. NCOM showed large lag differences decreasing in depth as the model predicted -39 hrs at the surface and -3 hrs in the near-bottom currents. HOPSn recorded larger lag times than HOPSS and there was zero lag at HOPSS in the surface currents.

Spatial accuracy of the model predictions is observed by statistically comparing neighboring grid points to the center point. Three of the models showed evidence of improved nowcasts via spatial lags (Figures 44-49). Higher correlations at a grid point other than the center grid point (5) indicate that the fronts and other oceanic features are misplaced with respect to reality. ROMS and HOPSS both had the optimal correlations aligned along the center of the grid (grid points 2, 5, 8) indicating no east-west spatial misalignment. The HOPSn model shows improvements with a shift to the southern row of the grid (grid points 7, 8, 9). The NCOM model predictions do not show any

discernible patterns in ADCP 1. At ADCP 2, the ROMS model shows spatial improvements to the south while the NCOM model shows improvements to the west (grid points 1, 4, 7) (Figures 47, 48 and 49). The HOPSn model showed optimal correlations at grid point one (northwest) at all three depths. HOPSs was the only model that did not show any overall spatial improvements by shifting the grid pattern indicating it gave the most accurate spatial predictions.

C. SUMMARY OF MODEL COMPARISONS

As a main focus of the ASAP experiment, three numerical models were compared with observations in an effort to assess their usefulness for adaptive sampling. In general the NCOM model produced the least reliable results. More localized models with shorter spin-up times appeared to give better predictions. Overall differences between the models and mooring data are expected. One of the complex factors in this experiment making it tougher for the models is that the ADCP moorings were located only 6.55 km apart thus creating a small scale area for model resolution.

The HOPS models were nested on a smaller local scale and the highest domain extended only to cover the Monterey Bay/ San Francisco regions as well as the Point Año Nuevo region. Point Año Nuevo is recognized to be a significant source of upwelling for the Monterey Bay and is located northward of the mooring locations (Ramp et al, 2005). This upwelling center has been shown to affect the circulation of the northern bay area. Even though all the models account for this outside forcing effect the HOPS models appear to predict flow patterns more accurately. The HOPS models were better at predicting the equatorward flow event (09-18 August) in the stick plot analysis. This event appeared to be the hardest for the models to describe. This is possibly because it resulted from an eddy rather than the wind, as indicated by the barotropic nature of the flow.

In addition to resolution and domains, there are many other parameters that can cause differences between model predictions. All numerical models are affected by the differences in data assimilation. All the models assimilated the same glider and aircraft data. In addition to these inputs the models assimilated other types of information into

their predictions. ROMS assimilated the MBARI buoy M1 and M2 temperature and salinity data and NCOM assimilated the MODAS information as well. It is difficult to determine whether these extra assimilations were helpful or not.

At ADCP 1 the ROMS and HOPSs models both had reasonable spatial accuracy. At ADCP 2, HOPSn showed the most consistent model output as it predicted the best improvements would occur with a northwest shift (grid point 1). This shift is completely opposite the southern shift the HOPSn model predicted at ADCP 1. After reviewing the three analysis methods, the HOPS models, in particular HOPSn, were the most accurate in terms of the metrics chosen.

D. MILITARY AND OPERATIONAL APPLICATIONS

Accurate current prediction by ocean models will benefit amphibious operations, special warfare operations, and mine warfare in the littoral zone. This project also provides information useful to oceanographers interested in understanding the combined effects of wind forcing and continental shelf bathymetry on ocean circulation. Model predictions can be improved by exploring different methods of real time data gathering, data assimilation, and enhanced numerical techniques.

APPENDIX A. FIGURES

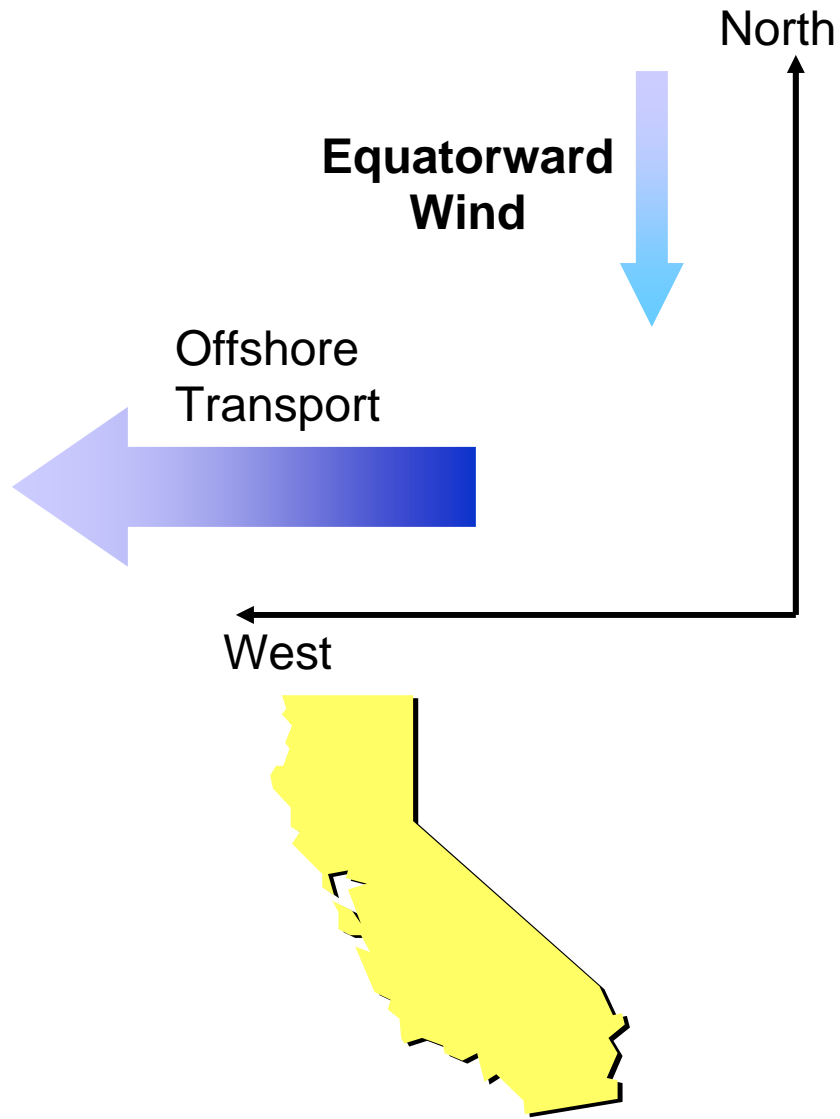


Figure 1. Illustration of coastal Ekman dynamics. Ekman transport is 90° to the right of the wind stress, therefore equatorward winds off the coast of Californian result in offshore transport, an important factor in the seasonal upwelling cycle.



Figure 2. Visual depiction of the upwelling process. (From [http://cordellbank.noaa.gov/ environment/seasons.html](http://cordellbank.noaa.gov/environment/seasons.html), last accessed February 2007)

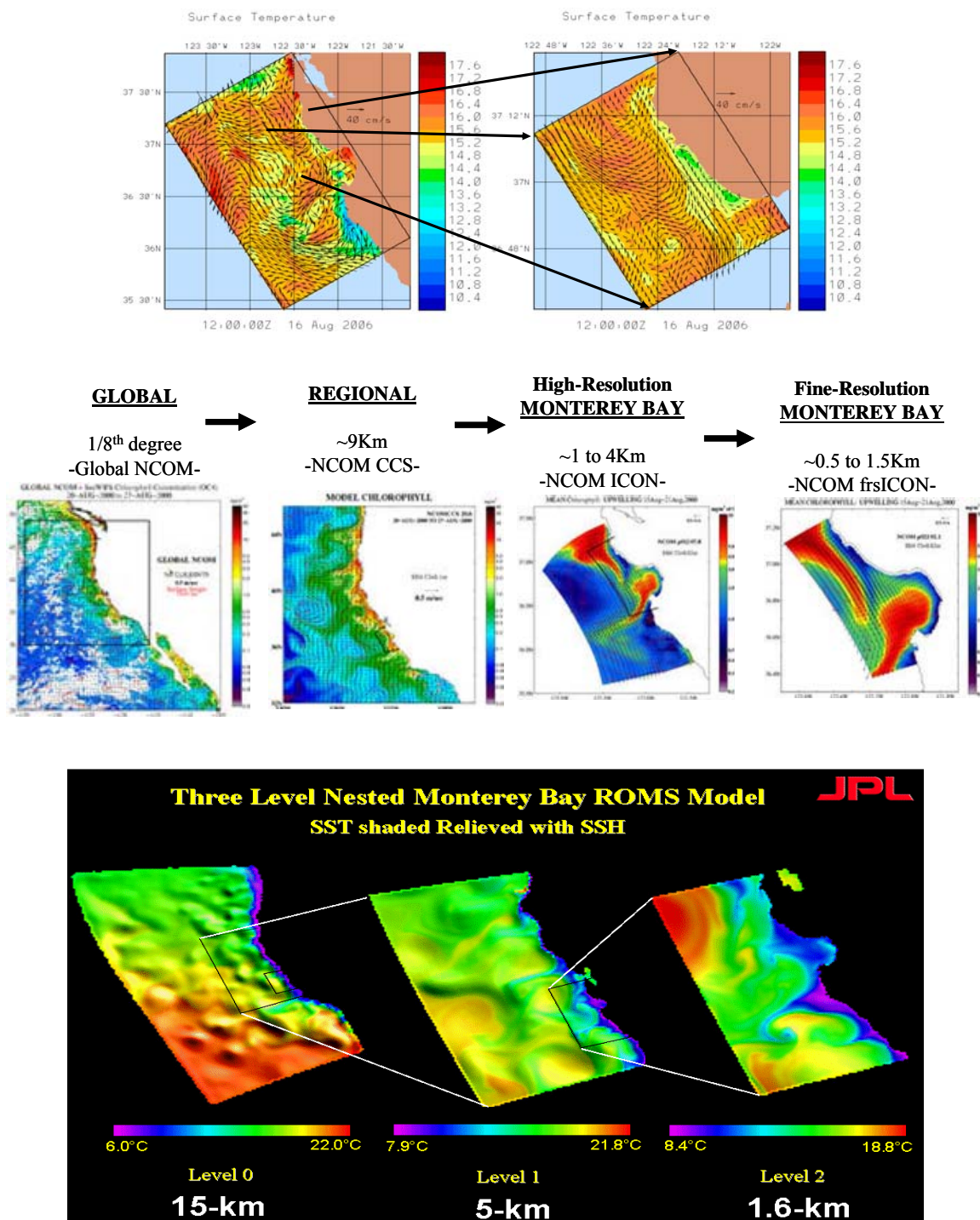


Figure 3. Top: HOPS two way nested modeling scheme (From Pierre Lermusiaux, MIT) Middle: Hierarchy of Navy Coastal Ocean Models (NCOM) in the Pacific (from <http://www7320.nrlssc.navy.mil>, last accessed May 2007) Bottom: Digital representation of ROMS model nesting depicting a three level one-way nested scheme (From <http://ocean.jpl.nasa.gov/MB06/>, last accessed April 2007).

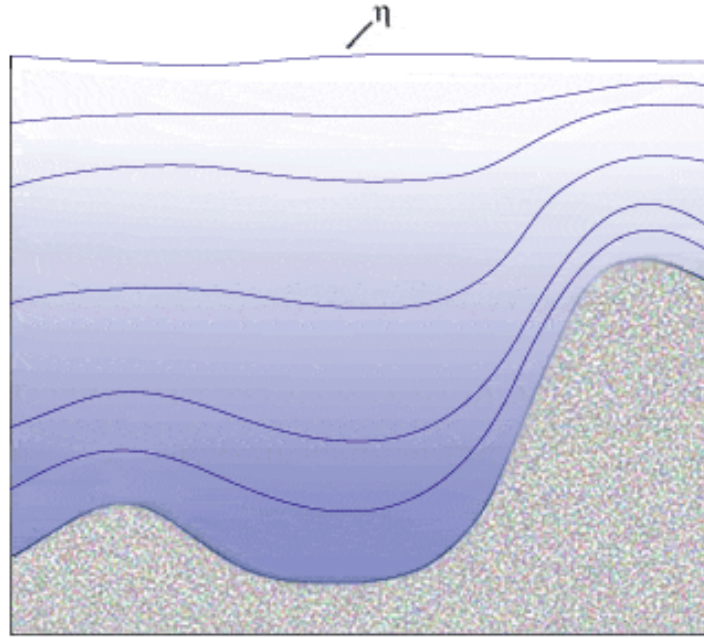


Figure 4. Illustration of Sigma coordinate method for resolving vertical levels in ocean models. This method follows the bottom topography and is more effective in coastal regions and over the continental shelf and slope. η represents sea surface height. Sigma coordinate systems are used by all three numerical models, the Harvard Ocean Prediction System (HOPS), Navy Coastal and Ocean Modeling (NCOM) and Regional Ocean Model System (ROMS) (From <http://www.oc.nps.navy.mil/nom/modeling/index.html>, last accessed April 2007).

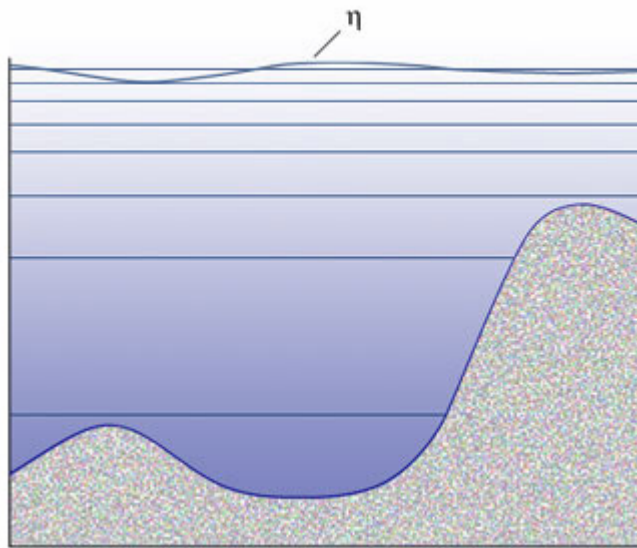


Figure 5. Illustration of z level coordinates. This type of vertical grid is more effective in the surface layers of the water column. η represents sea surface height (From <http://www.oc.nps.navy.mil/nom/modeling/index.html>, last accessed April 2007).

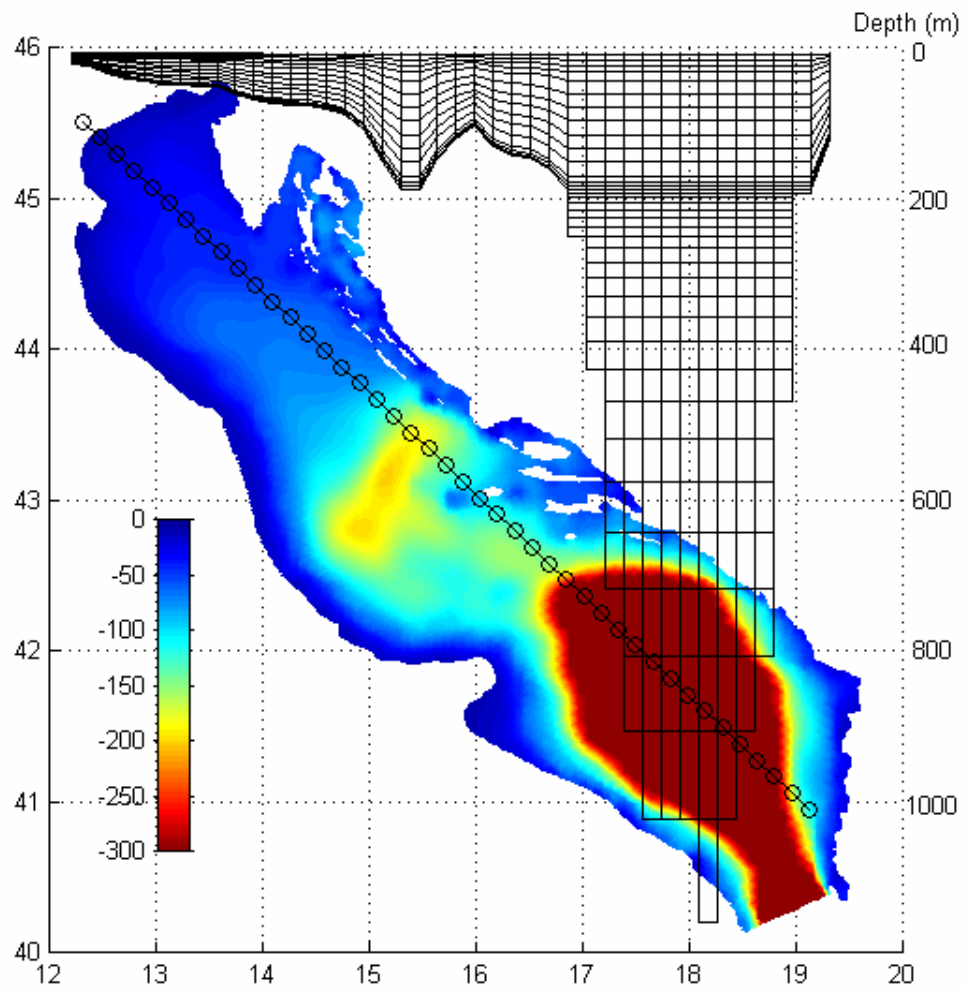


Figure 6. This representation of hybrid vertical levels shows the sigma coordinates at the surface layer and the z coordinates in the deep water and away from abrupt topography. (From Dr. Julie Pullen, Marine Meteorology Division, NRL).

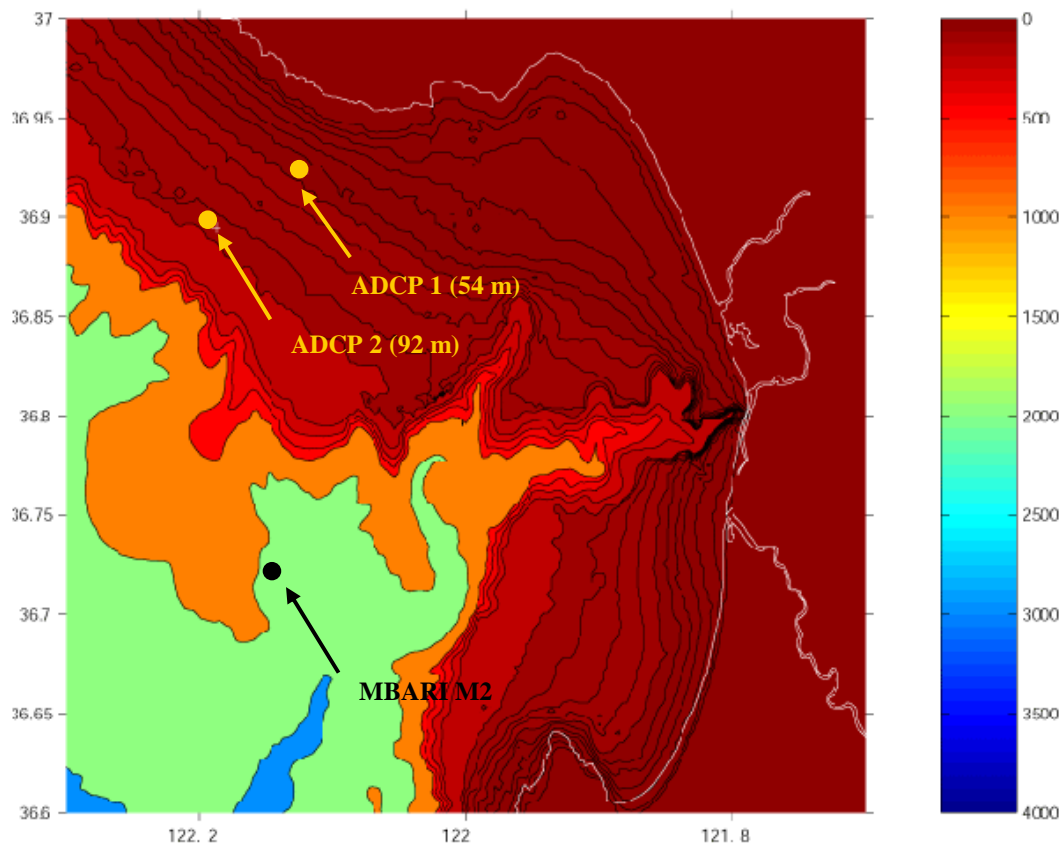


Figure 7. ADCP moorings and MBARI M2 wind buoy locations near the Monterey Bay. Bathymetric contours in meters are shown by the color bar. The solid white line is the coastline.

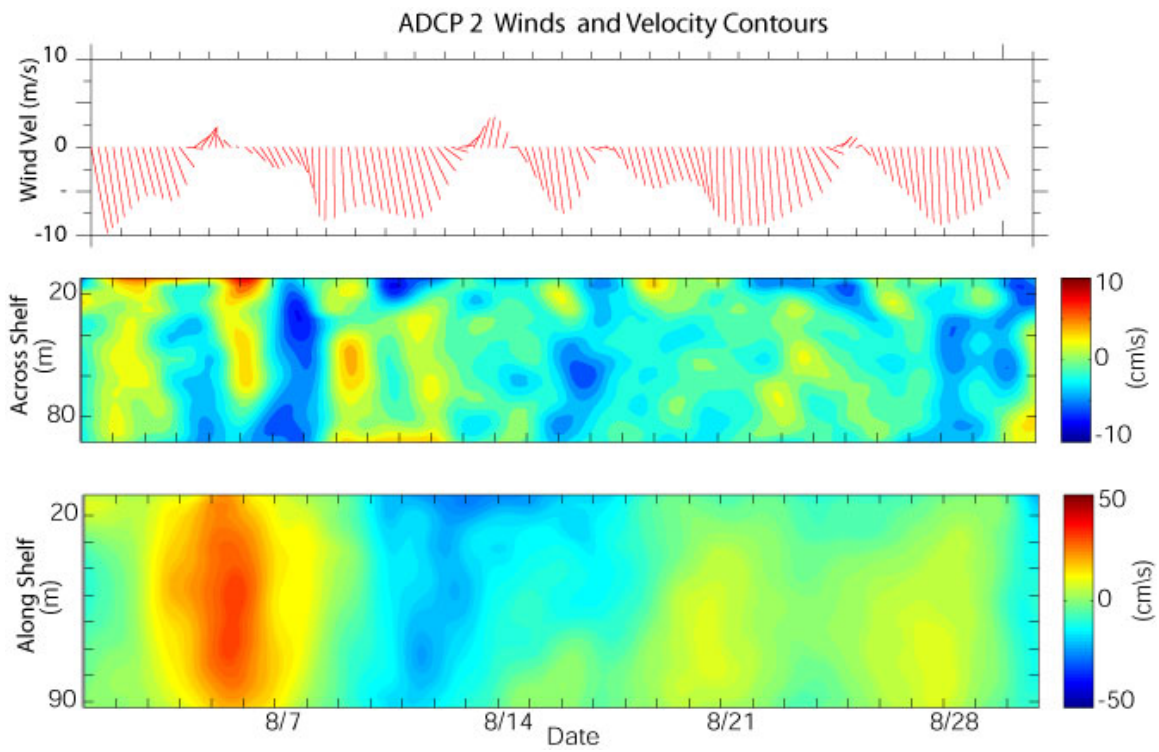


Figure 8. Wind vectors (top), across-shelf velocity contours (middle), and alongshore velocity contours (bottom) at ADCP 2.

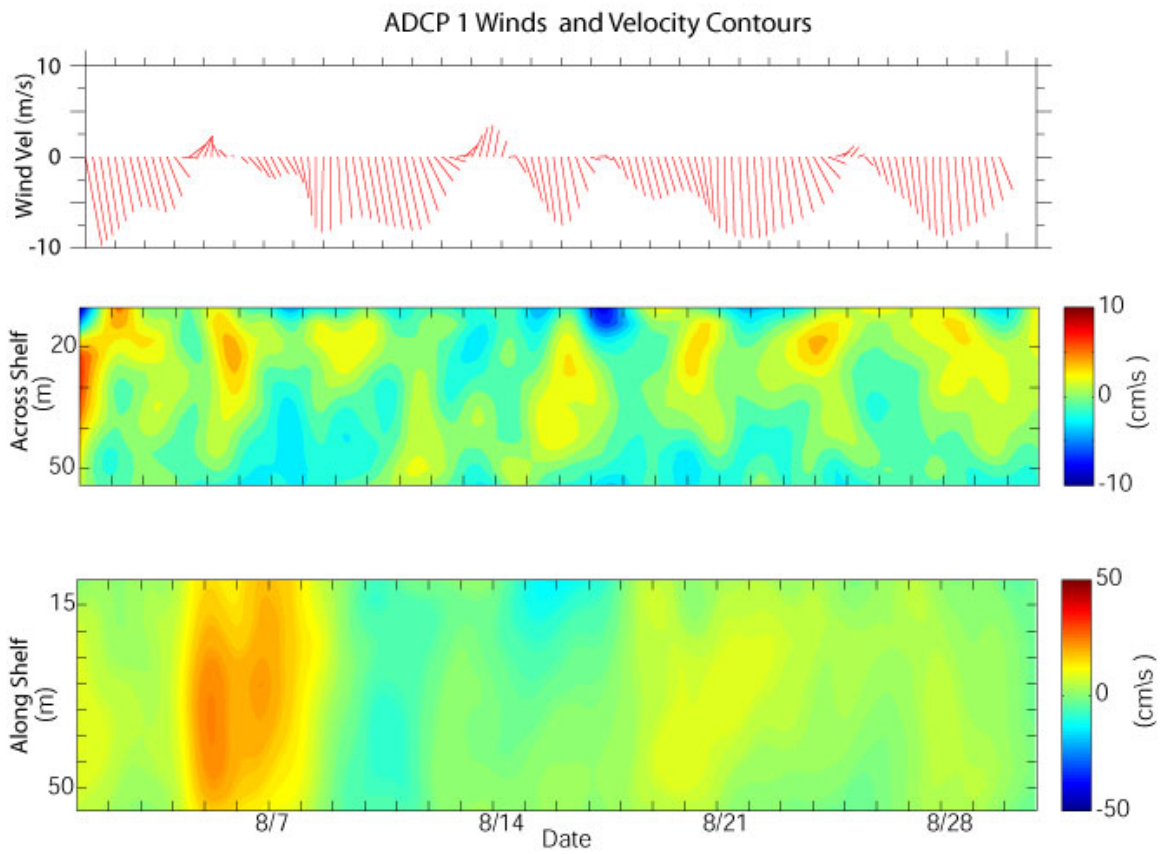


Figure 9. Wind vectors (top), across-shelf velocity contours (middle), and alongshore velocity contours (bottom) at ADCP 1.

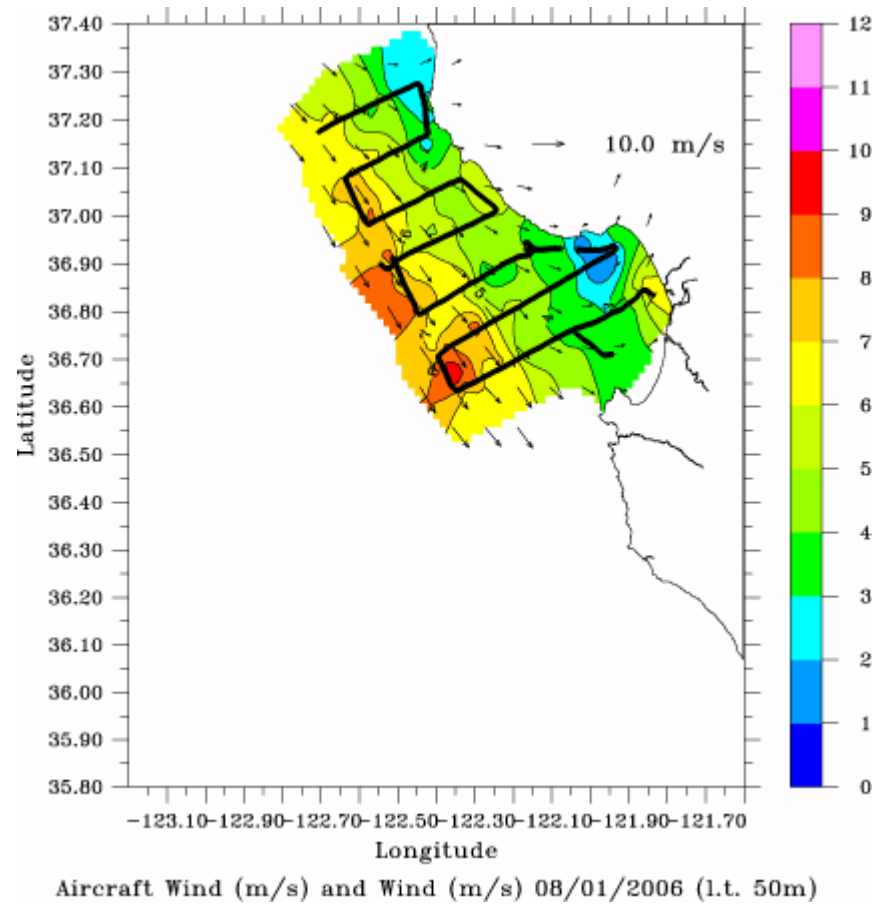


Figure 10. Spatial distribution of the surface wind at 30 m elevation as observed by the NPS Twin Otter Aircraft. The magnitude is shown by both the arrows and the color bar. The units are in m/s.

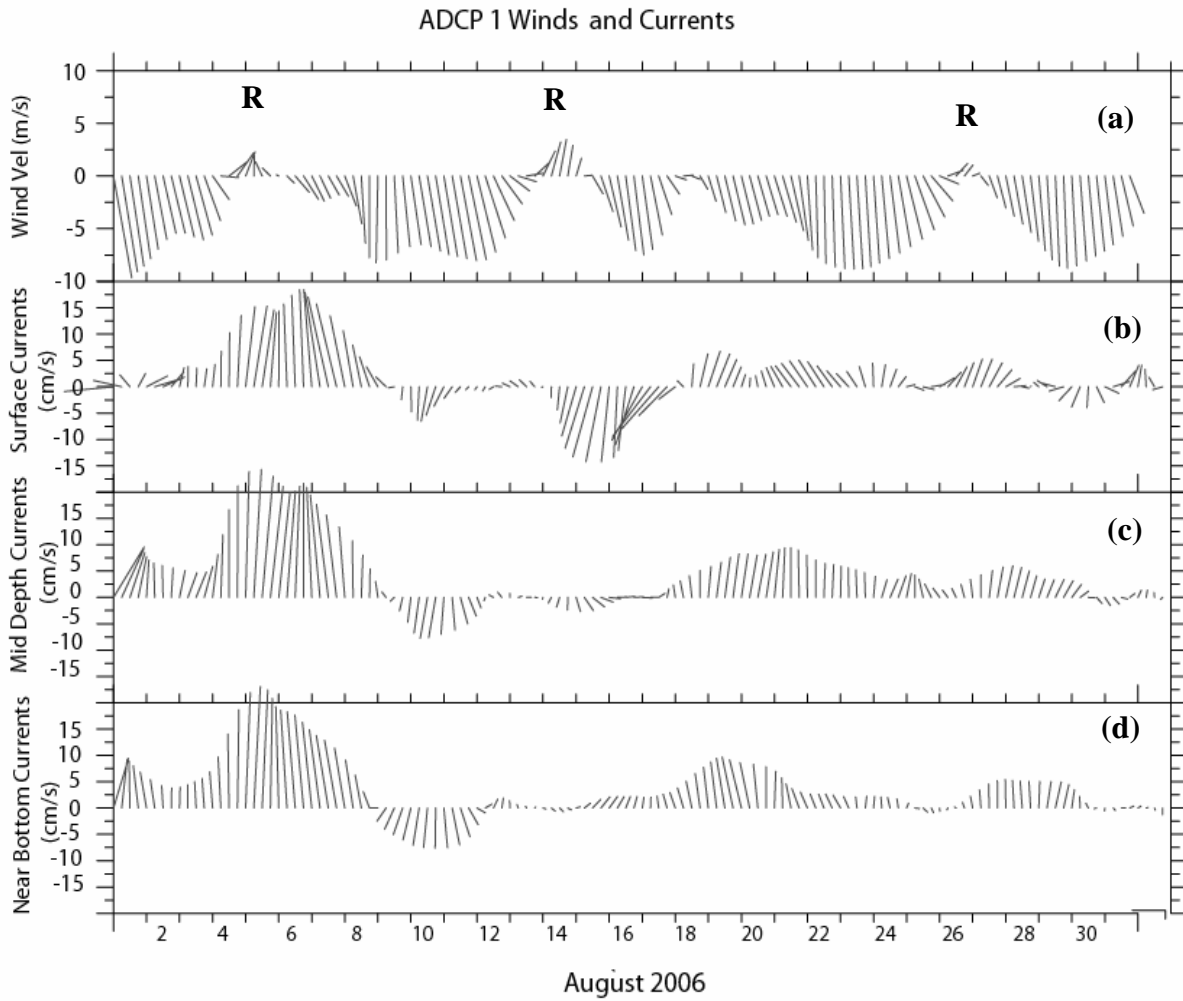


Figure 11. Stick plot of the velocity vectors for (a) the wind from MBARI M2 compared with the stick plots for the (b) surface (10 m), (c) mid-depth (34 m) and (d) near-bottom (46 m) currents for ADCP 1. The sticks are plotted every six hours. Relaxations in the winds are denoted by **R**. Wind relaxation events are positive (poleward) and upwelling wind events are negative (equatorward). Poleward current is positive and equatorward current is negative.

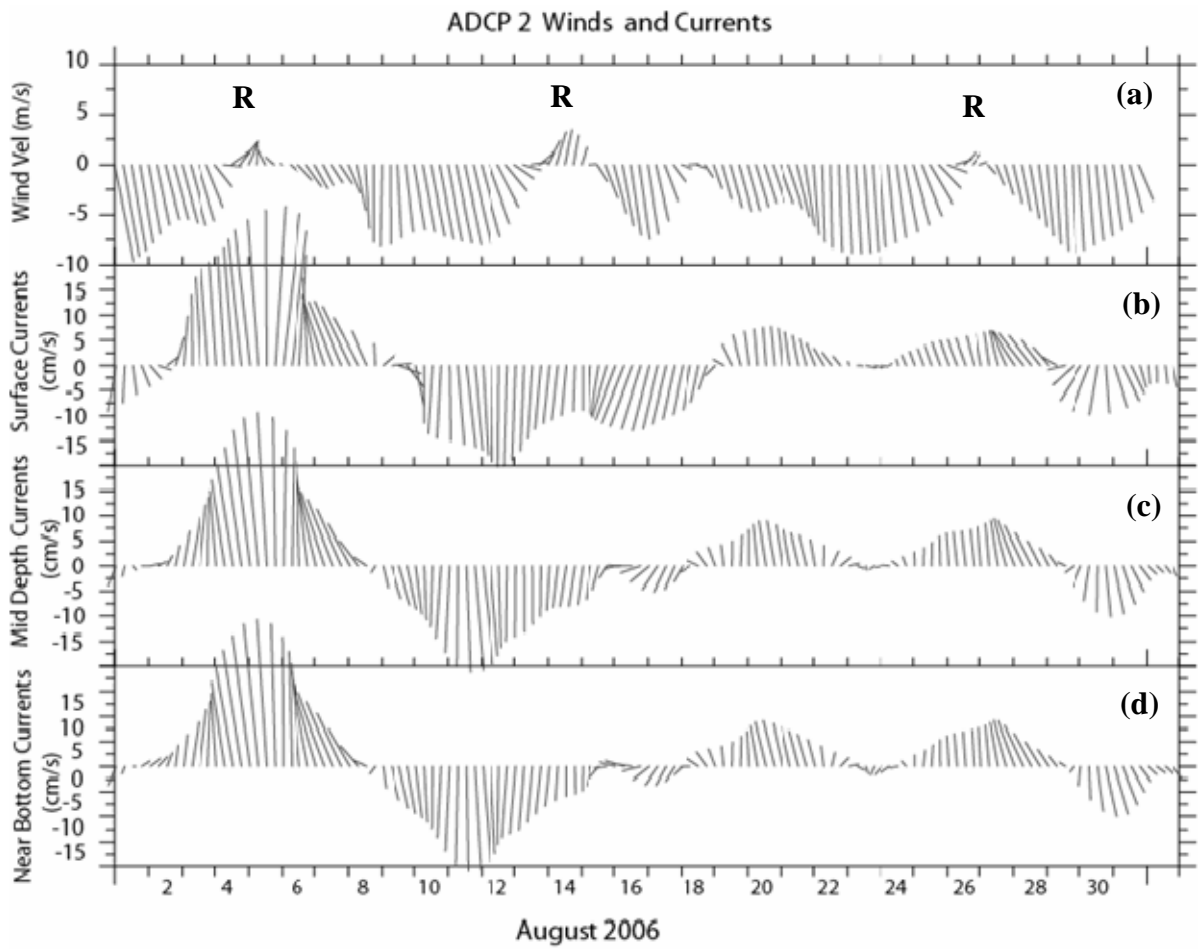
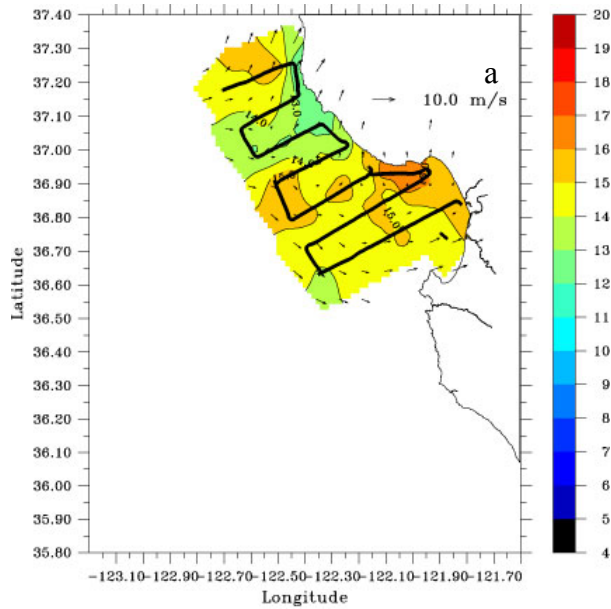
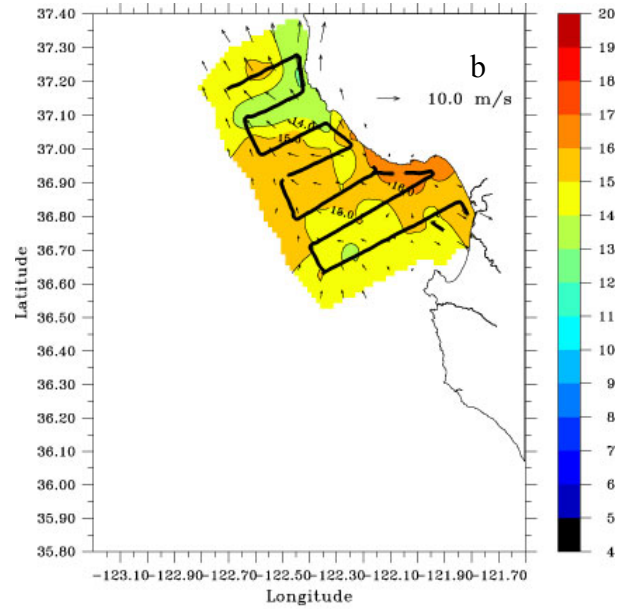


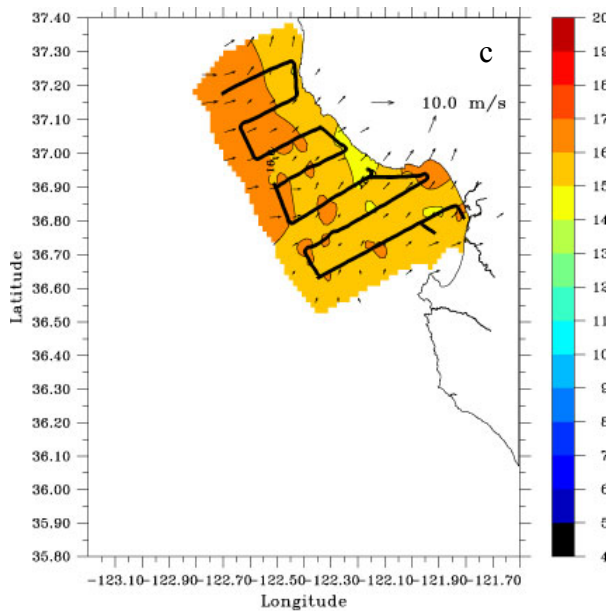
Figure 12. Stick plot of the velocity vectors for (a) the wind from MBARI M2 compared with the stick plots for the (b) surface (10 m), (c) mid-depth (34 m) and (d) near-bottom (46 m) currents for ADCP 2. The sticks are plotted every six hours. Relaxations in the winds are denoted by **R**. Wind relaxation events are positive (poleward) and upwelling wind events are negative (equatorward). Poleward current is positive and equatorward current is negative.



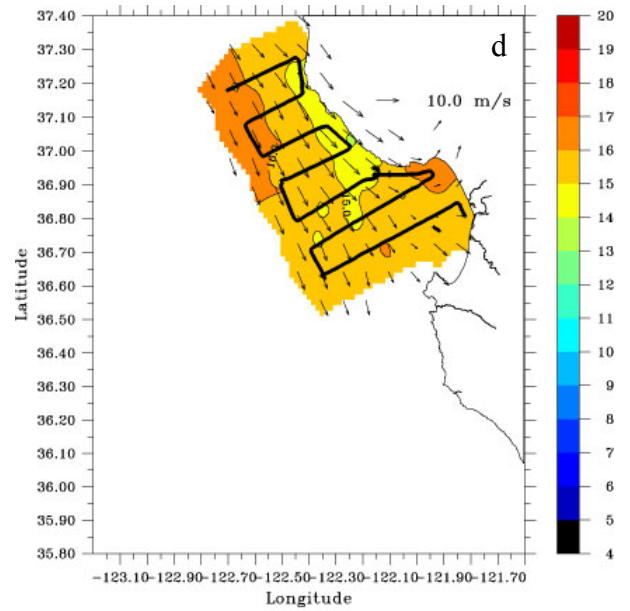
Aircraft SST (°C) and Wind (m/s) 08/03/2006 (l.t. 50m)



Aircraft SST (°C) and Wind (m/s) 08/04/2006 (l.t. 50m)



Aircraft SST (°C) and Wind (m/s) 08/07/2006 (l.t. 50m)



Aircraft SST (°C) and Wind (m/s) 08/08/2006 (l.t. 50m)

Figure 13. Spatial distribution of the wind at 30 m altitude and sea surface temperatures as observed by the NPS Twin Otter Aircraft for a) August 3; b) August 4; c) August 7; and d) August 8, 2006. The magnitude of the wind is shown by the arrows and the sea surface temperatures are shown by the color bar. The units are in m/s.

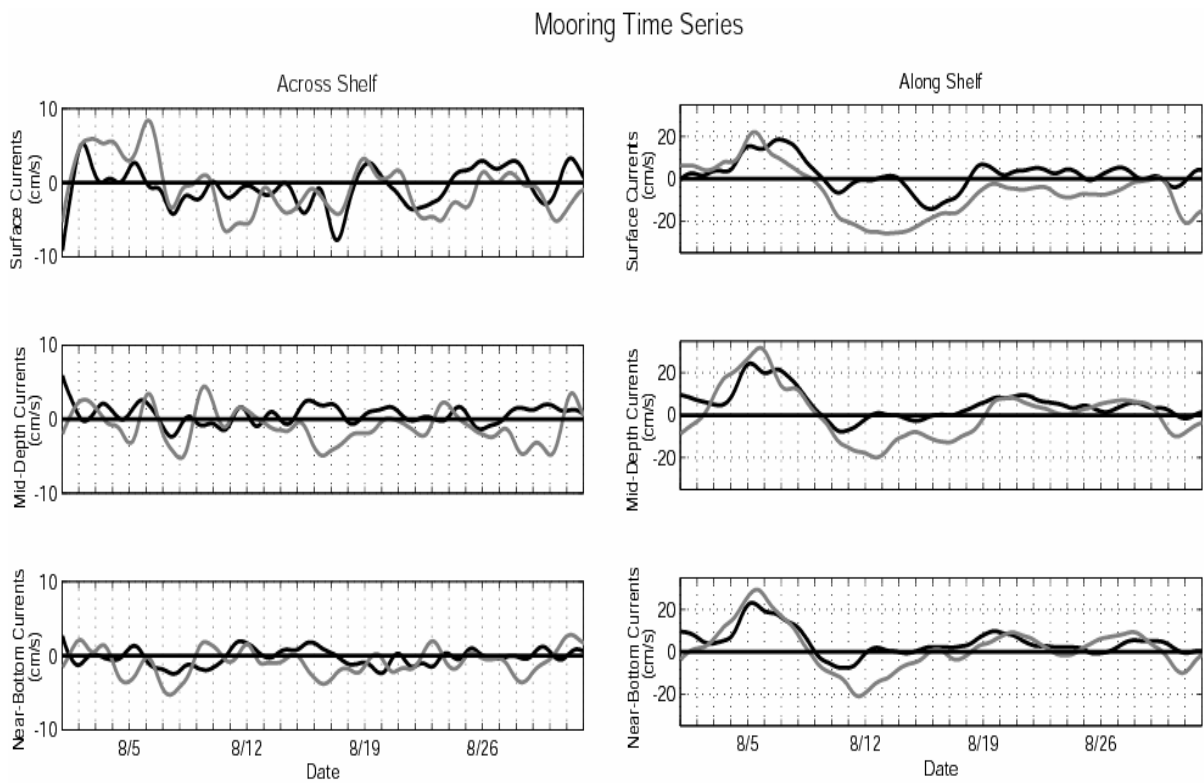


Figure 14. Time series comparing data from the two ADCPs. The black line is ADCP 1 and gray line is ADCP 2.

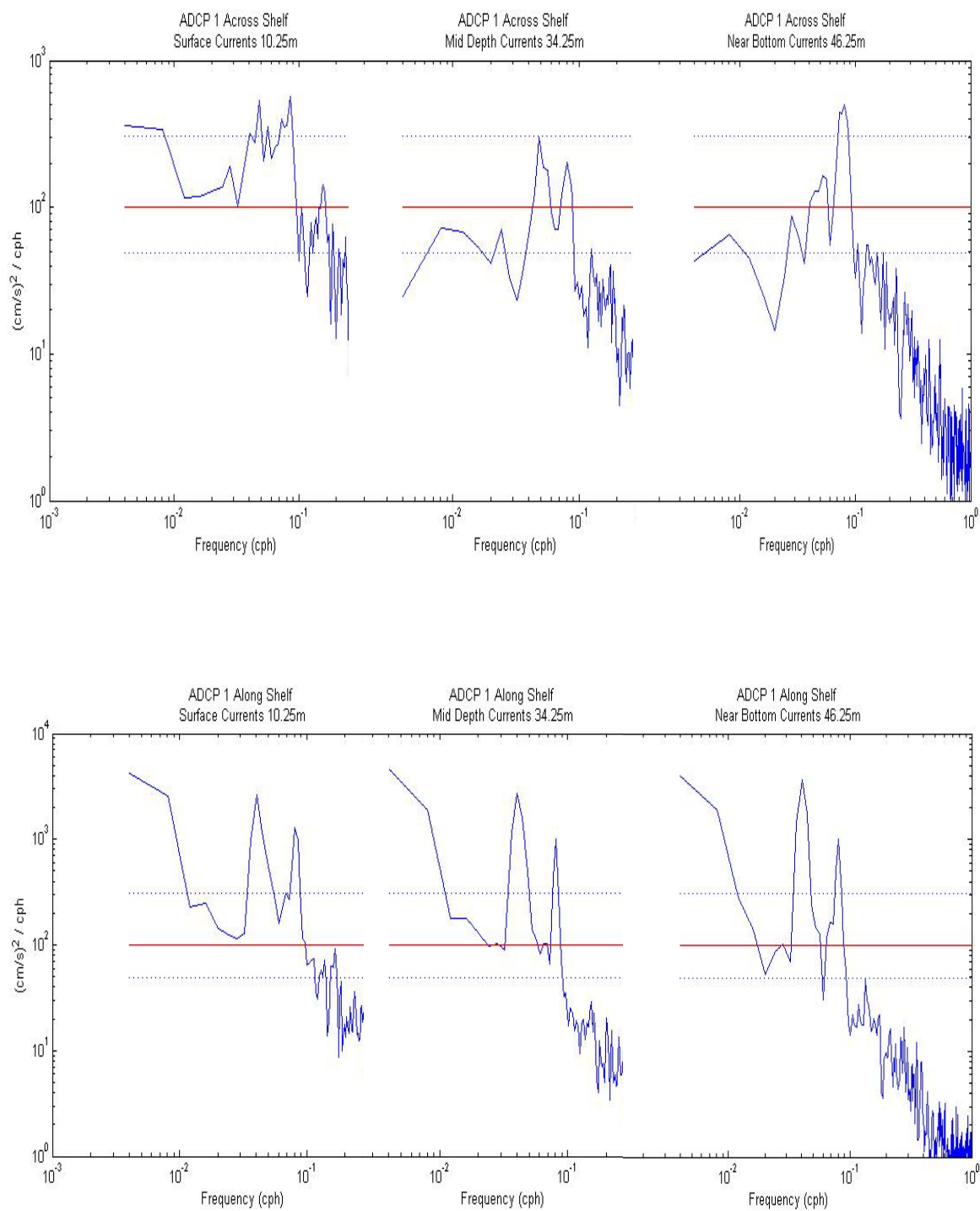


Figure 15. Autospectra of the surface (10 m), mid-depth (34 m), and near-bottom (46 m) currents for ADCP 1. Note the energy difference between the across-shelf (top) and alongshelf (bottom) components.

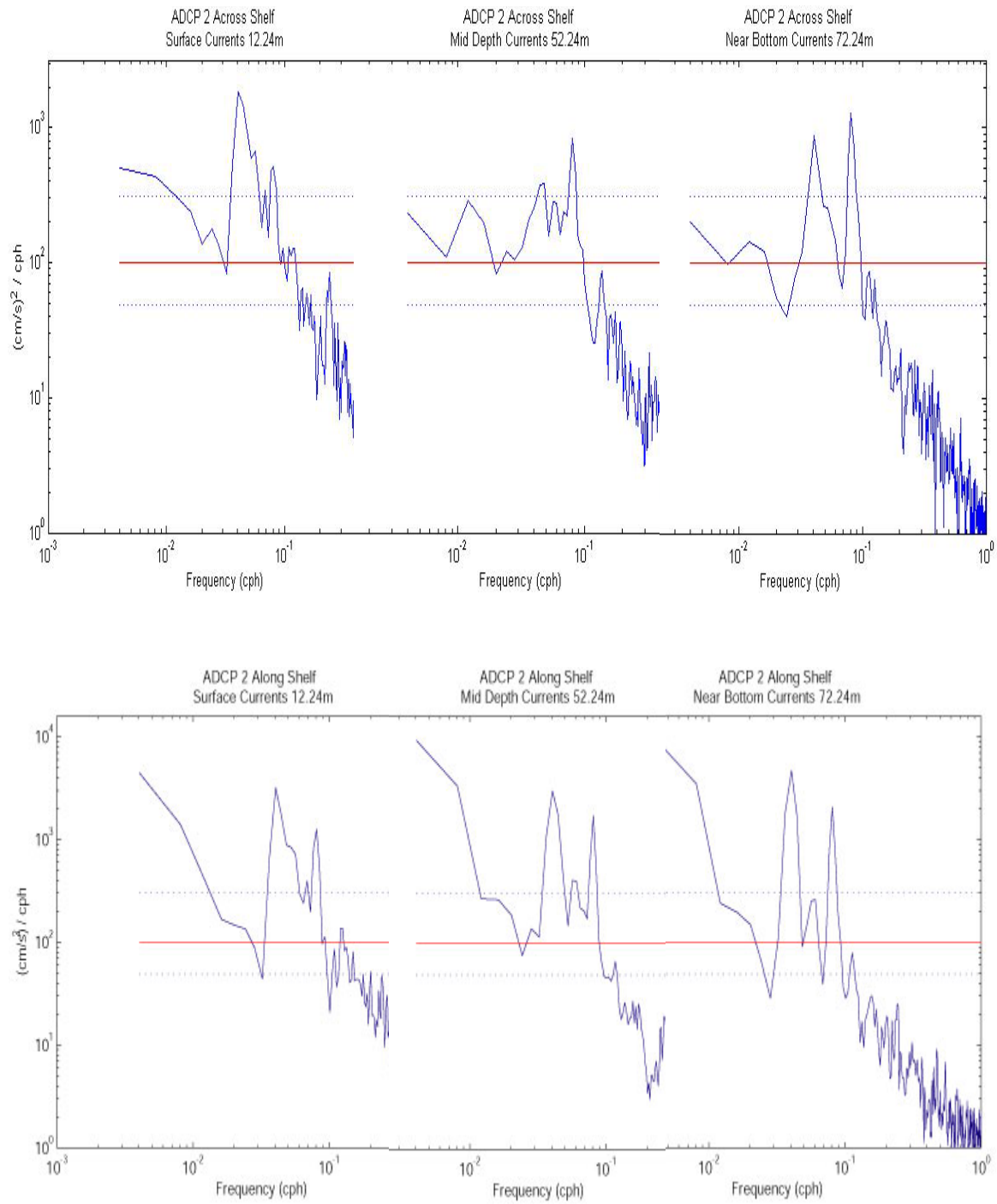


Figure 16. Autospectra of the surface (12.24m), mid-depth (52.24m), and near-bottom (72.24m) currents for ADCP 2. Note the energy difference between the across-shelf (top) and alongshelf (bottom) components.

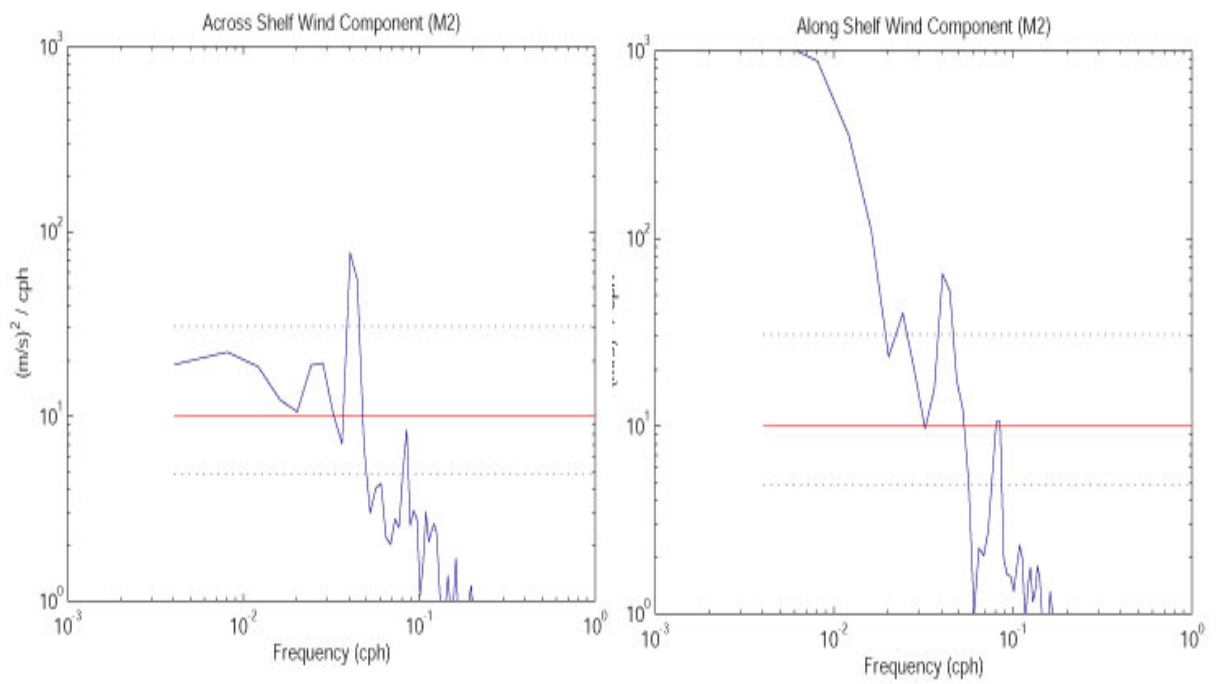


Figure 17. Across-shelf and alongshelf autospectra for the wind observations at MBARI Buoy M2.

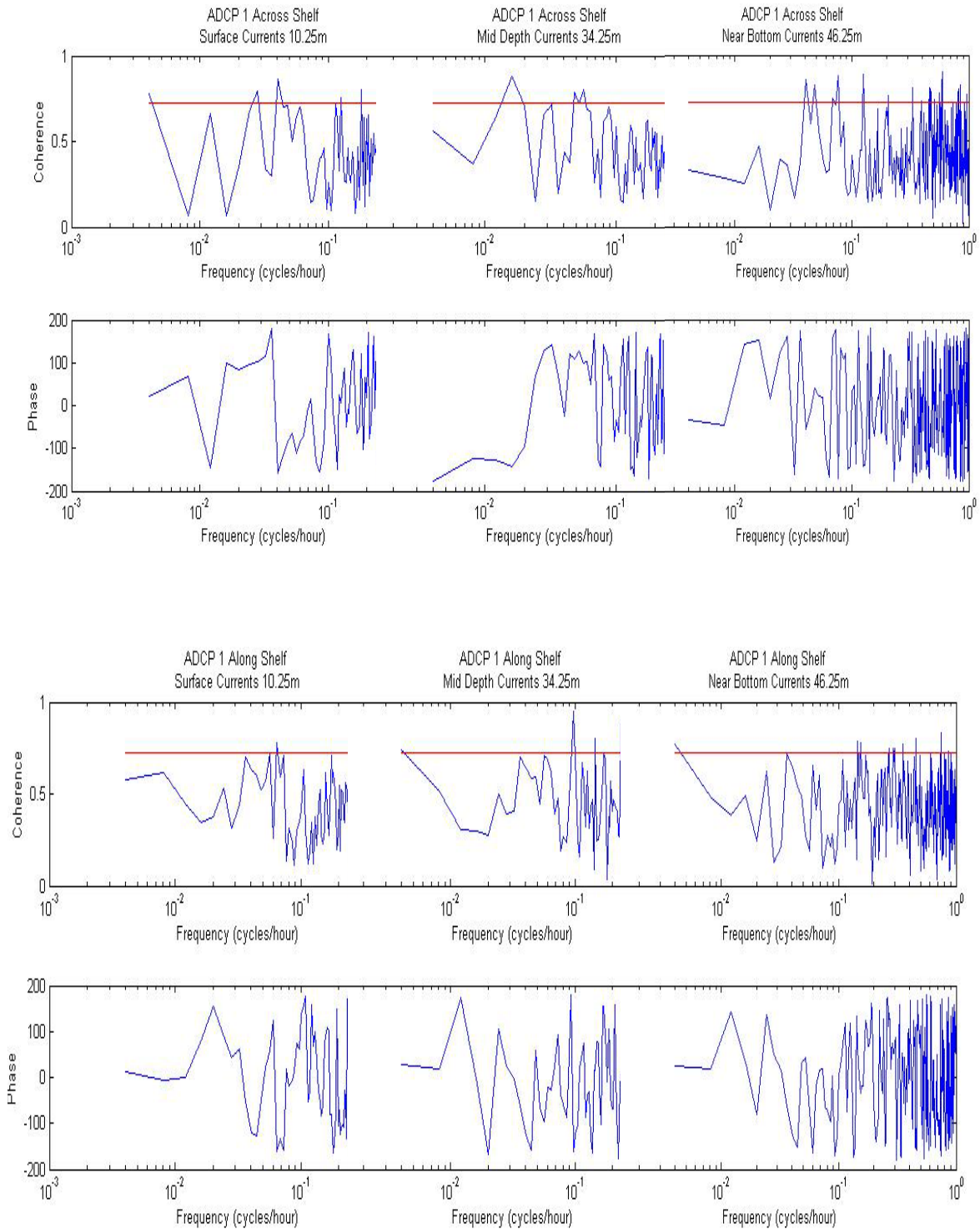


Figure 18. Coherence and phase plots between wind and current for surface (10 m), mid-depth (34 m), and near-bottom (46 m) currents for ADCP 1. A positive (negative) phase means wind leads (lags) the current. The red line indicates a 95% significance level for the coherence (From: Amos and Koopmans, 1963)

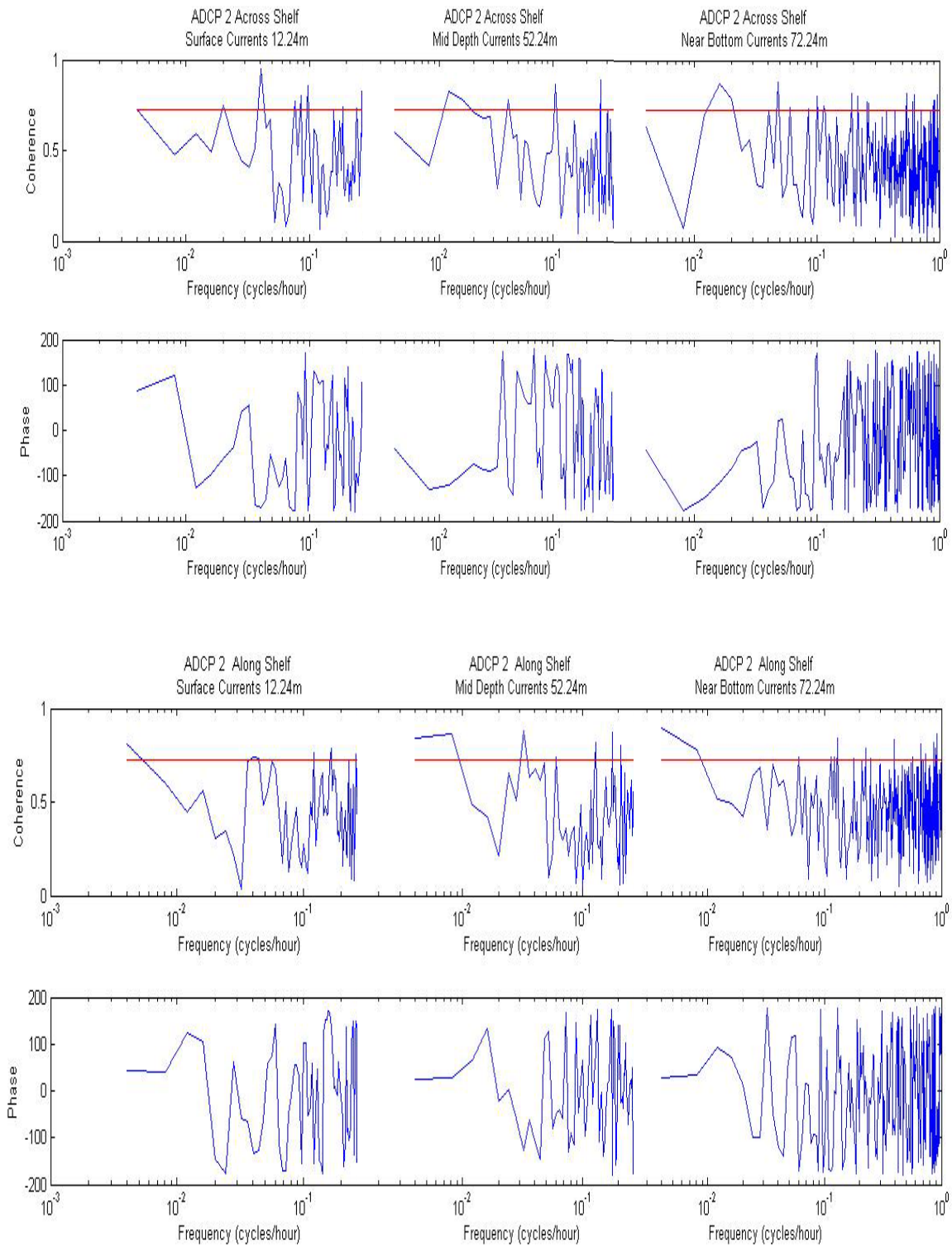


Figure 19. Coherence and phase plots between wind and current for surface (12 m), mid-depth (52 m), and near-bottom (72 m) currents for ADCP 2. A positive (negative) phase means wind leads (lags) the current. The red line indicates a 95% significance level for the coherence (From: Amos and Koopmans, 1963).

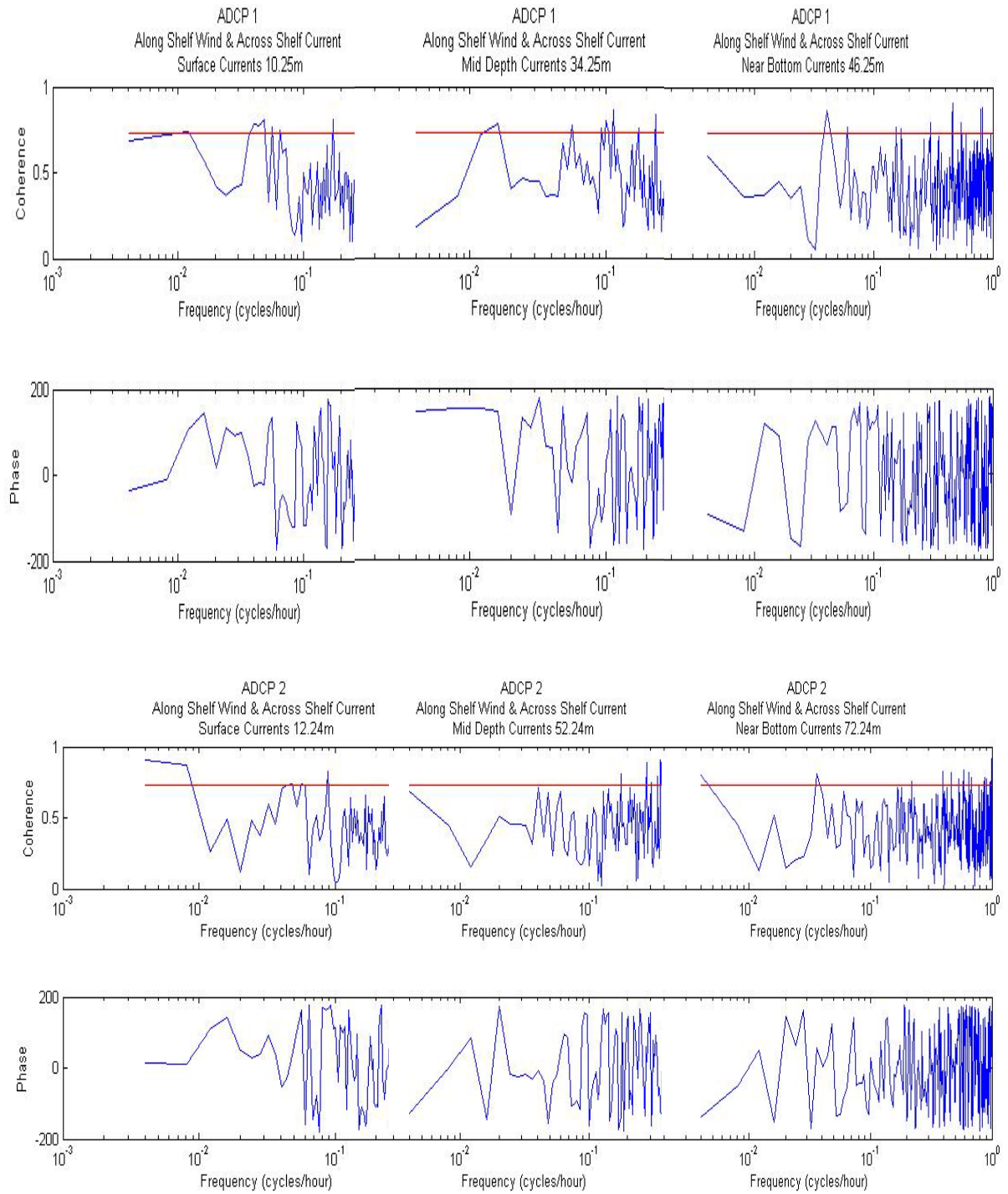


Figure 20. Coherence and phase plots for alongshelf wind and across-shelf currents for ADCP 1 and 2. A positive (negative) phase means wind leads (lags) the current. The red line indicates a 95% significance level for the coherence (From: Amos and Koopmans, 1963)

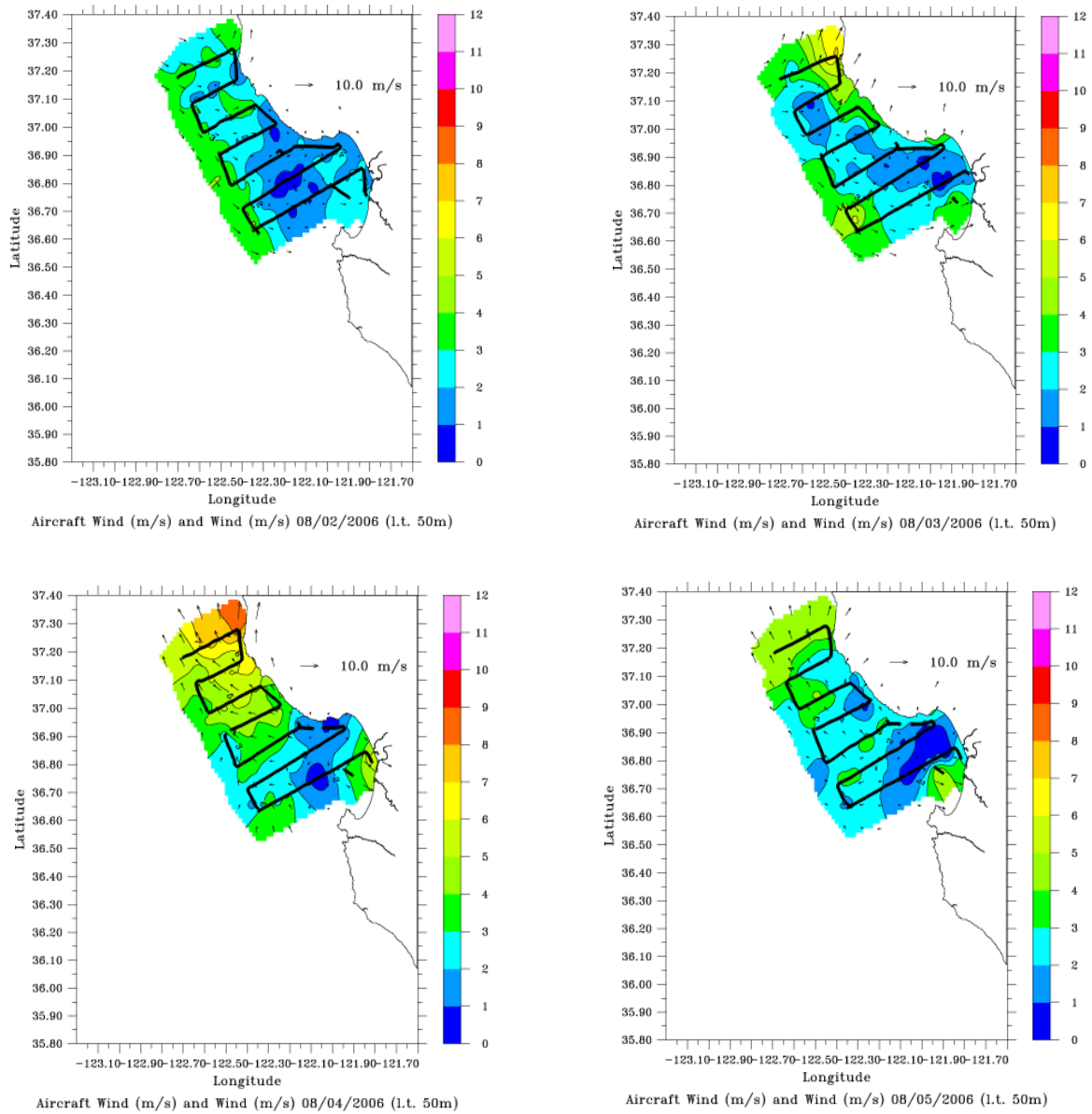


Figure 21. Aircraft data during the relaxation event on 02-05 August 2006. There are stronger winds north of the cape and minimum winds at the mouth of the bay.

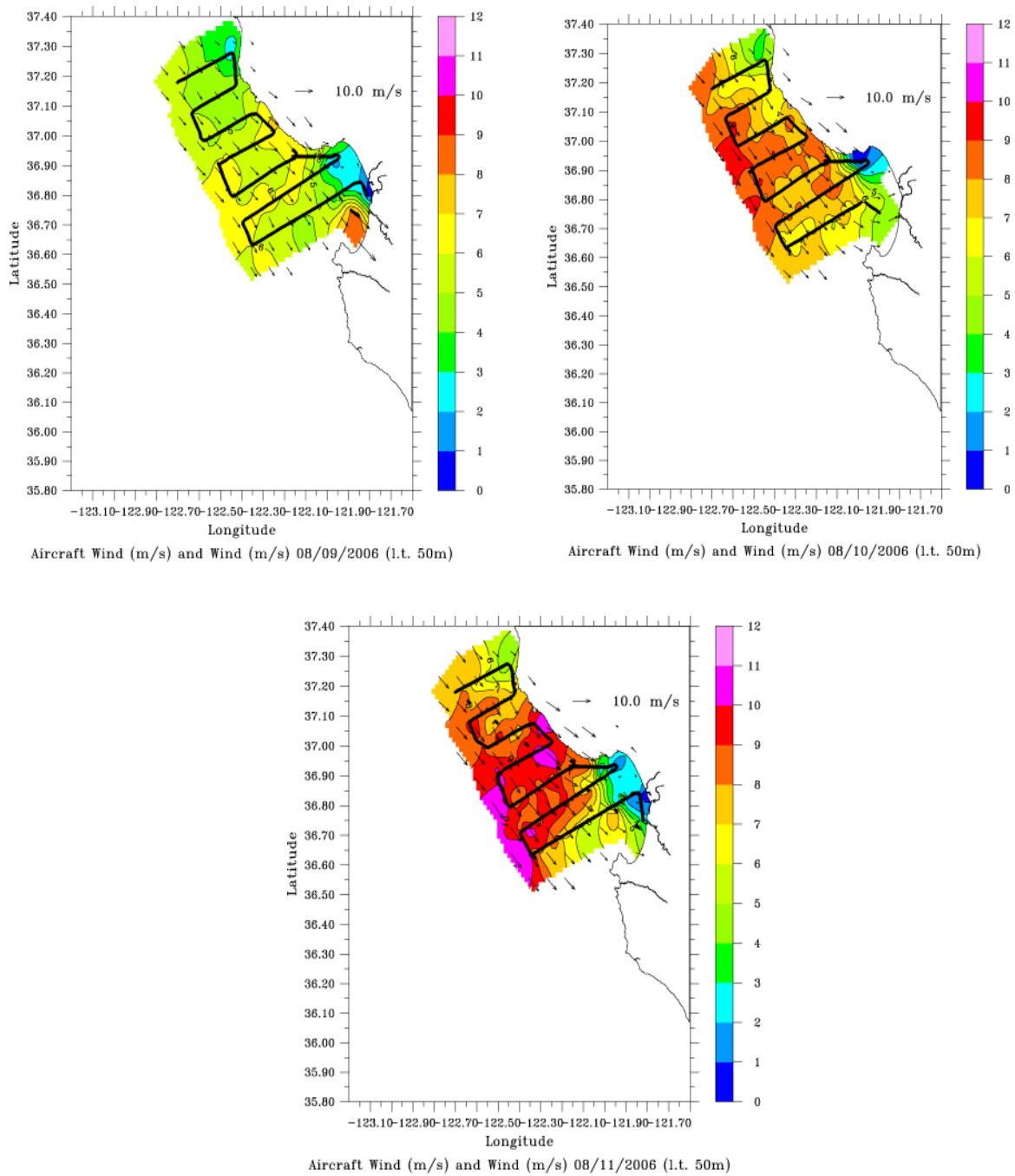


Figure 22. Upwelling event from the 09-11 August 2006. Note the maximum of alongshore wind off Point Año Nuevo.

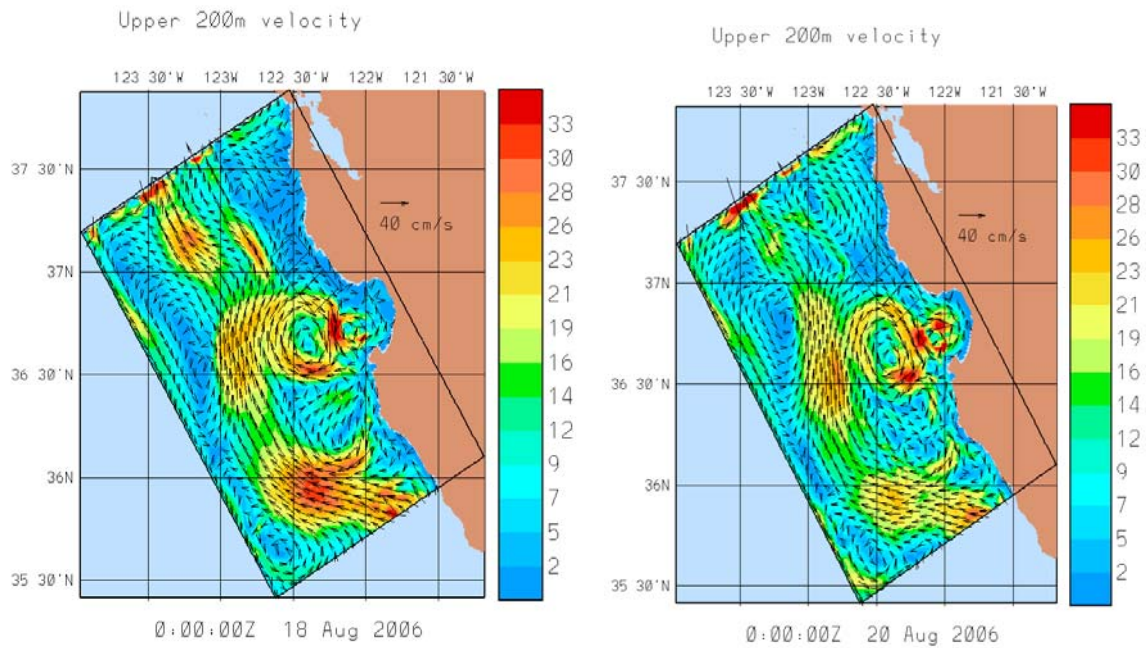


Figure 23. Harvard Ocean Modeling System model output showing eddies, meanders, and other non-local events that affect the current flow. (From Lermusiaux, W.G., P.J. Haley, and W.G. Leslie, 2006: ASAP: adaptive sampling and prediction Monterey Bay 2006, Harvard University, from http://oceans.deas.harvard.edu/ASAP/index_ASAP.html, last accessed February 2007).

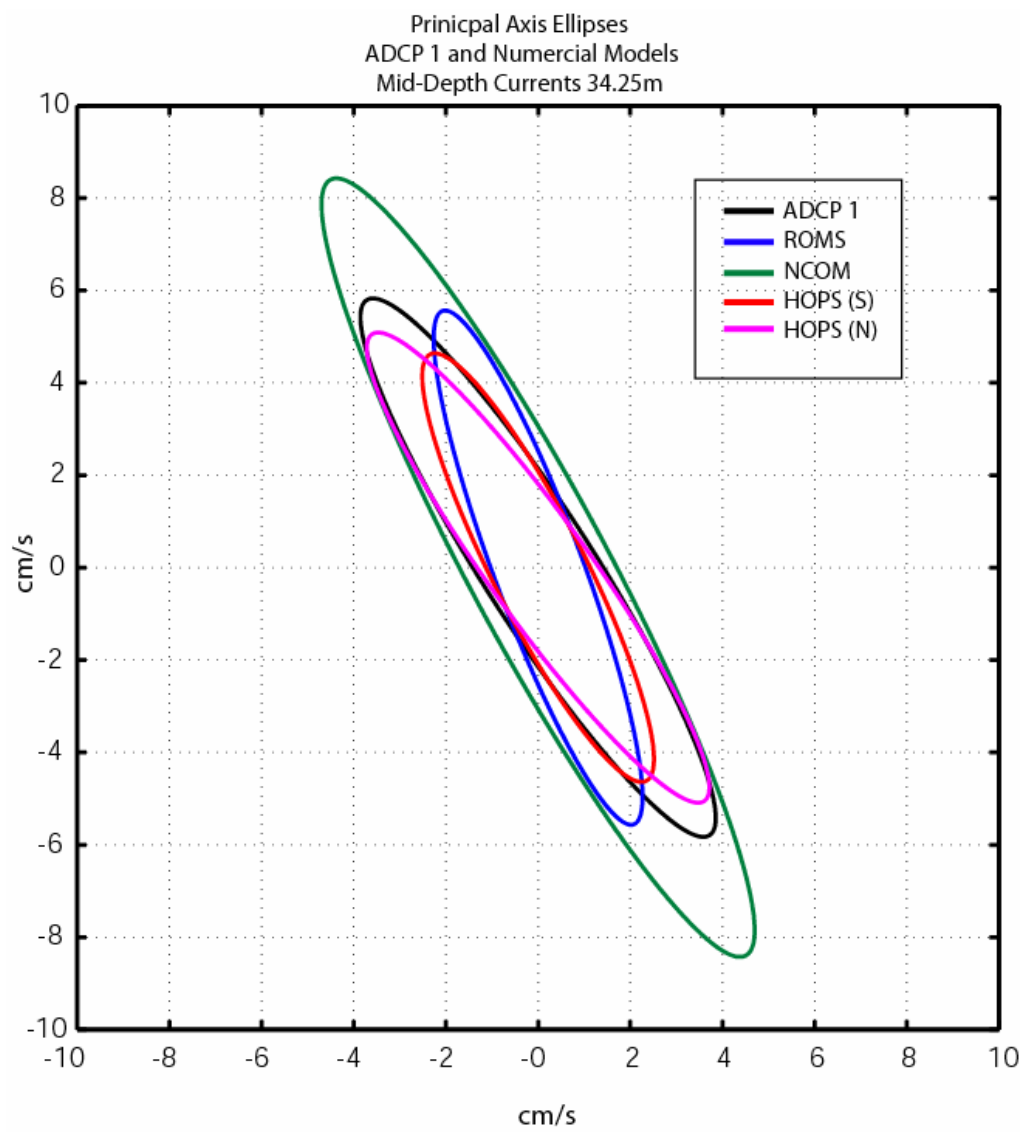


Figure 24. Principle variance ellipses for the numerical models and ADCP 1 mooring data.

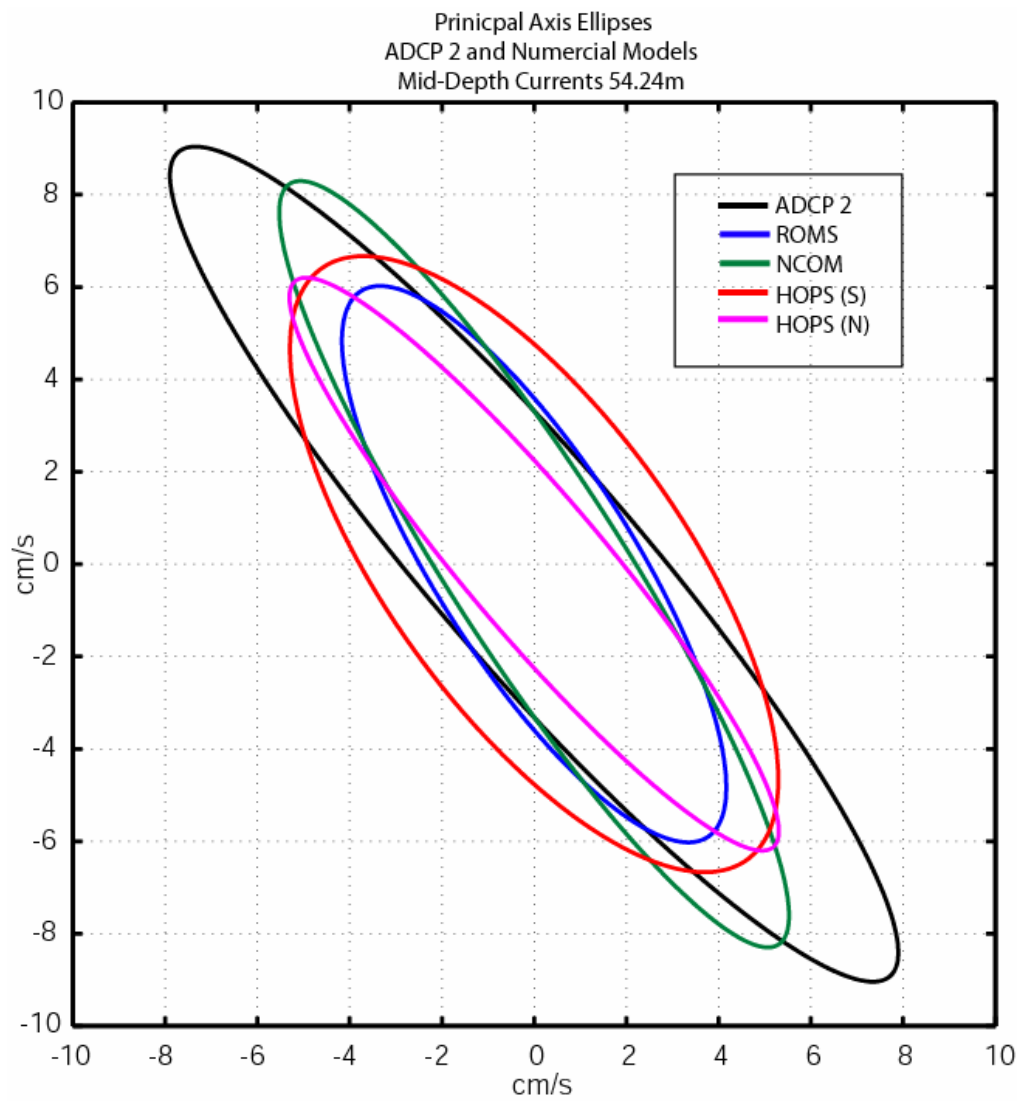


Figure 25. Principle variance ellipses for the numerical models and ADCP 2 mooring data.

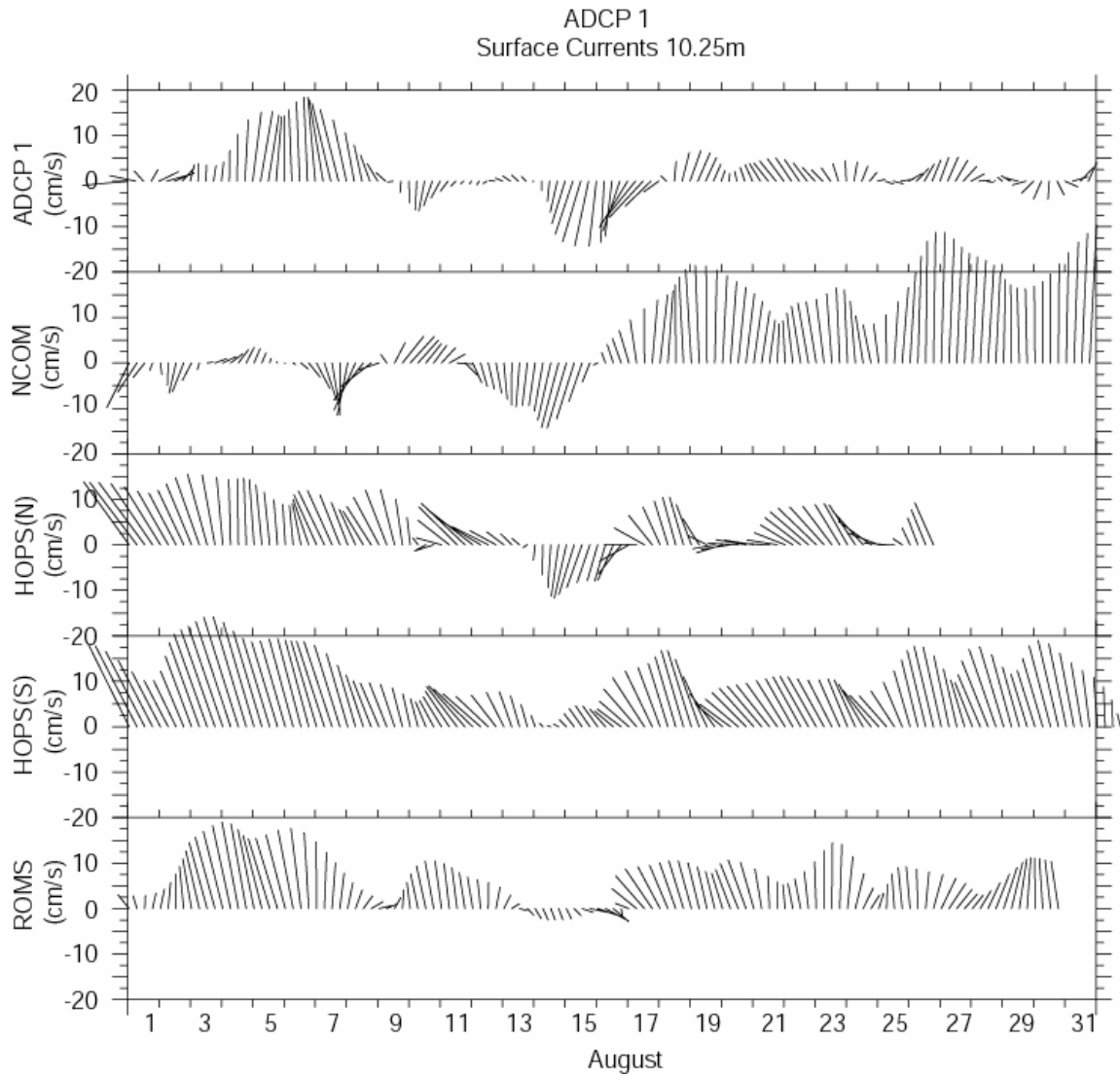


Figure 26. Stick vector plots comparing surface currents at ADCP 1 with the four numerical models.

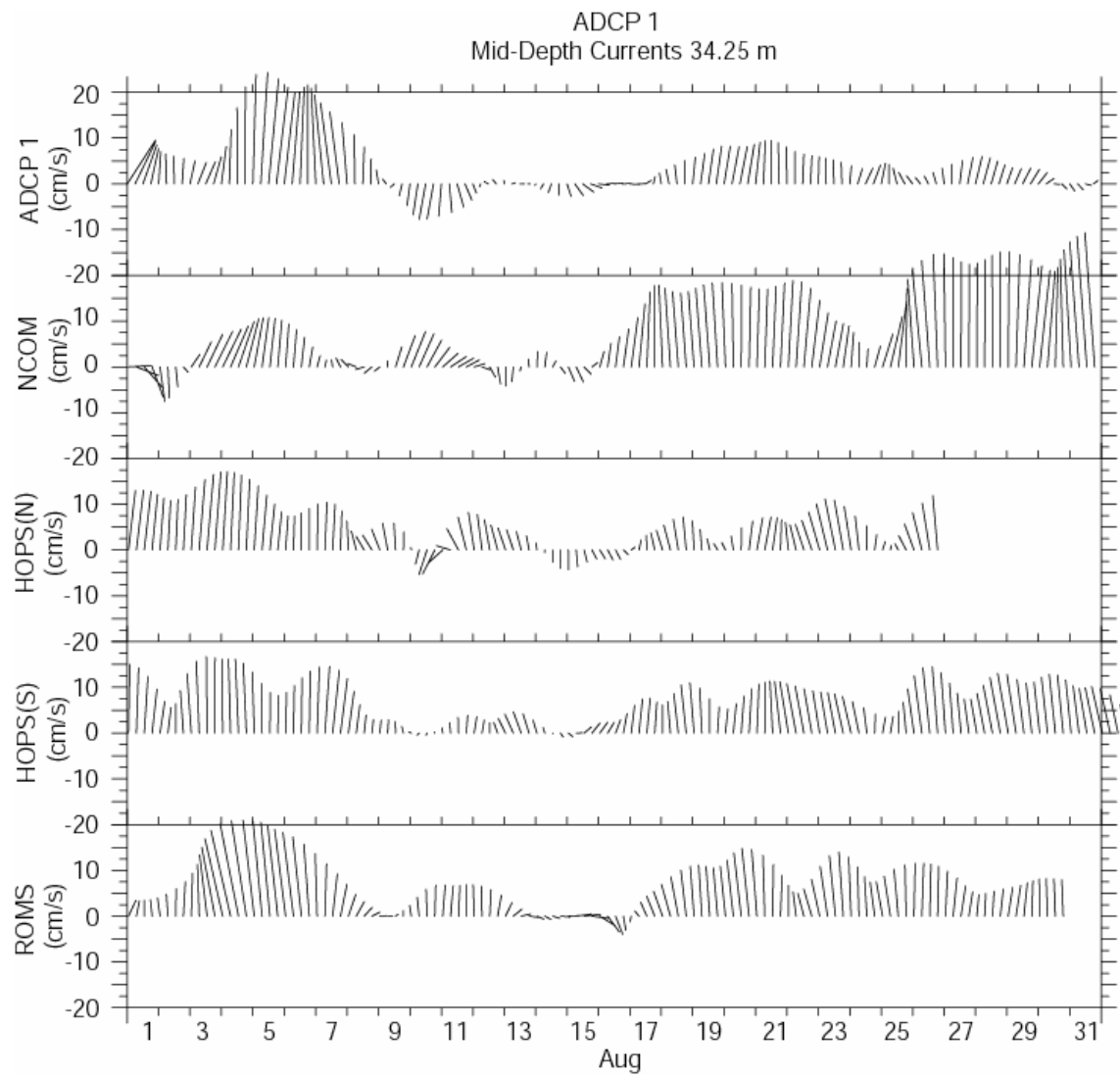


Figure 27. Stick vector plots comparing mid-depth currents at ADCP 1 with the four numerical models.

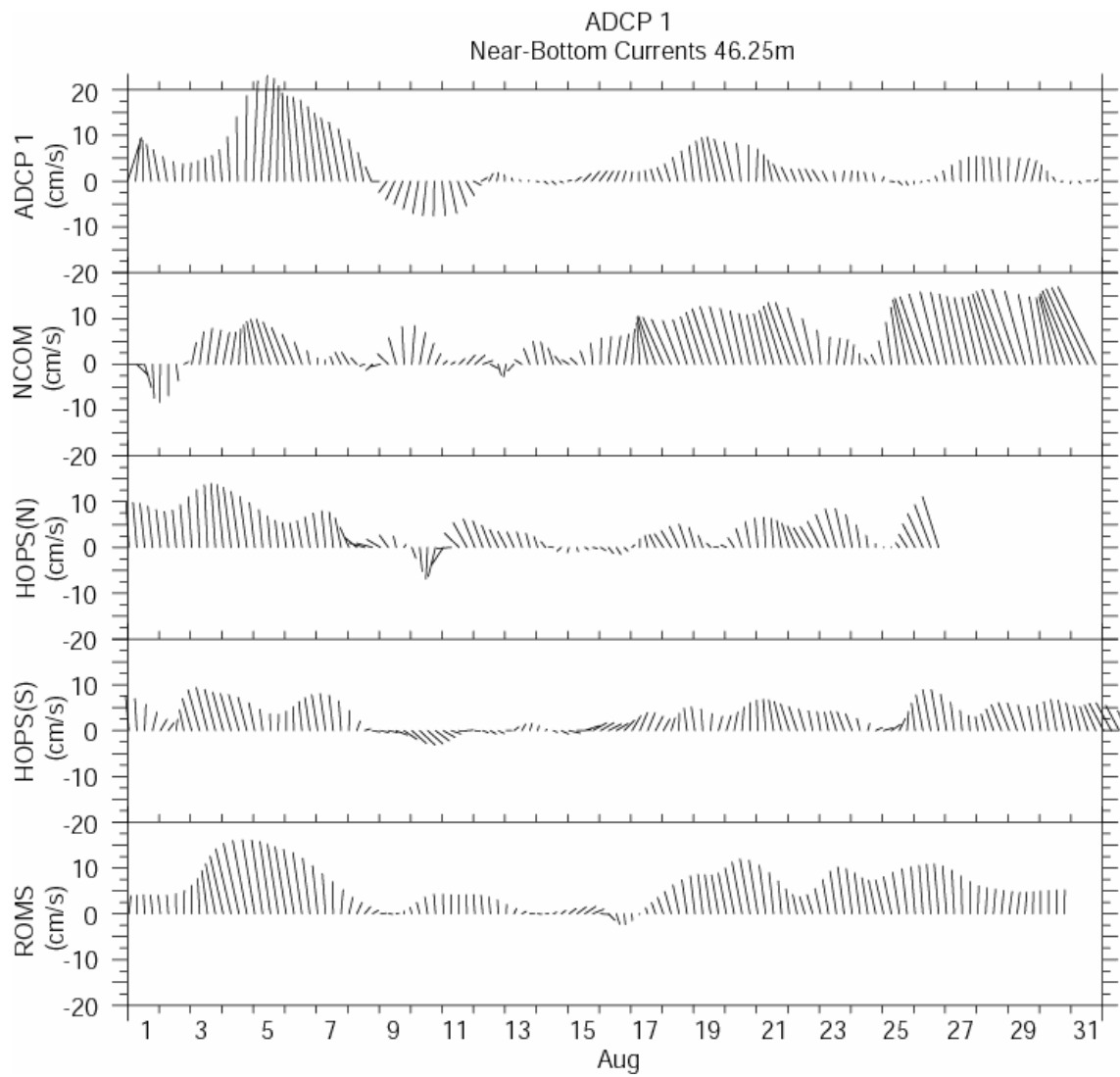


Figure 28. Stick vector plots comparing near-bottom currents at ADCP 1 with the four numerical models.

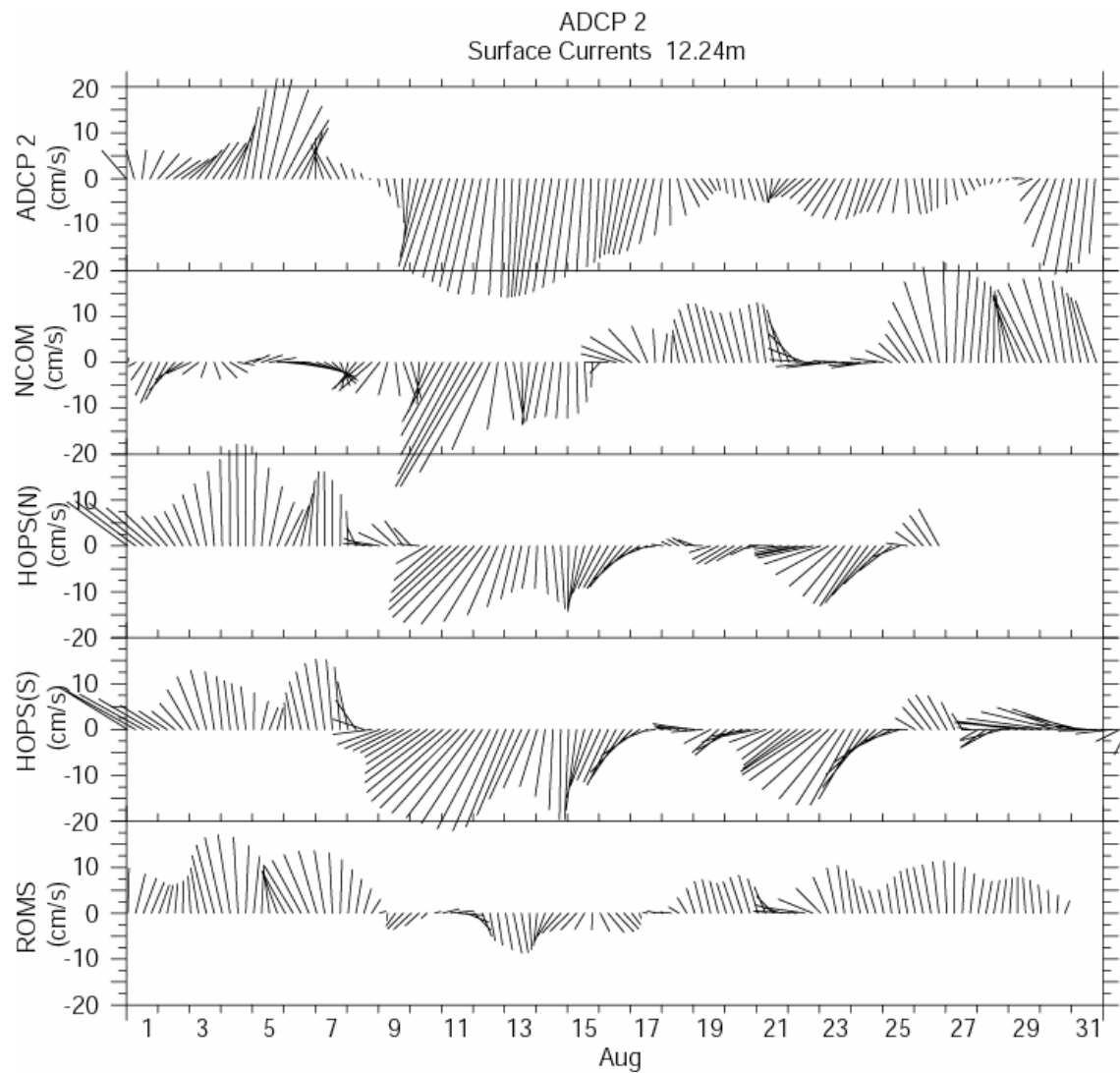


Figure 29. Stick vector plots comparing surface currents at ADCP 2 with the four numerical models.

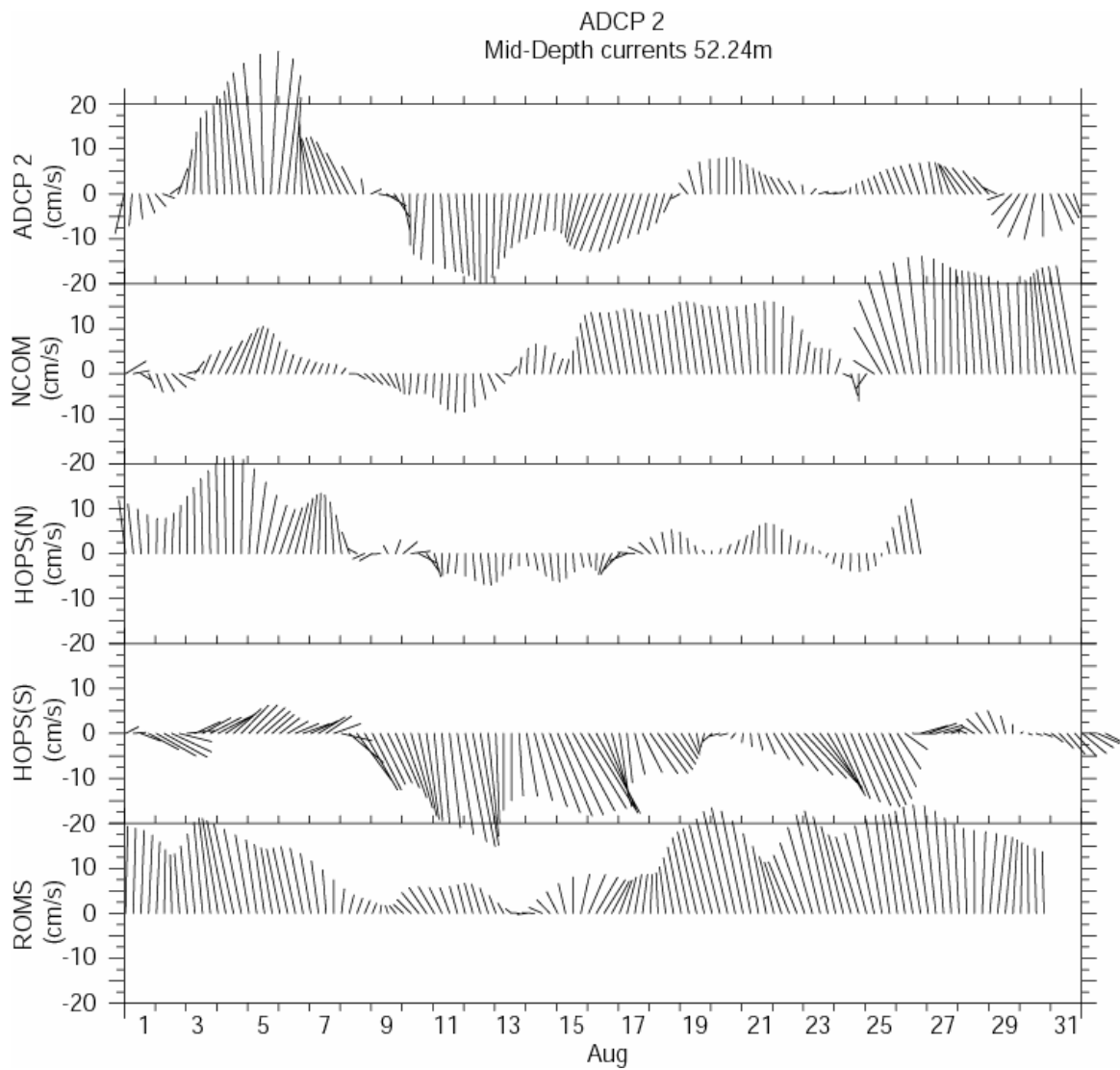


Figure 30. Stick vector plots comparing mid-depth currents at ADCP 2 with the four numerical models.

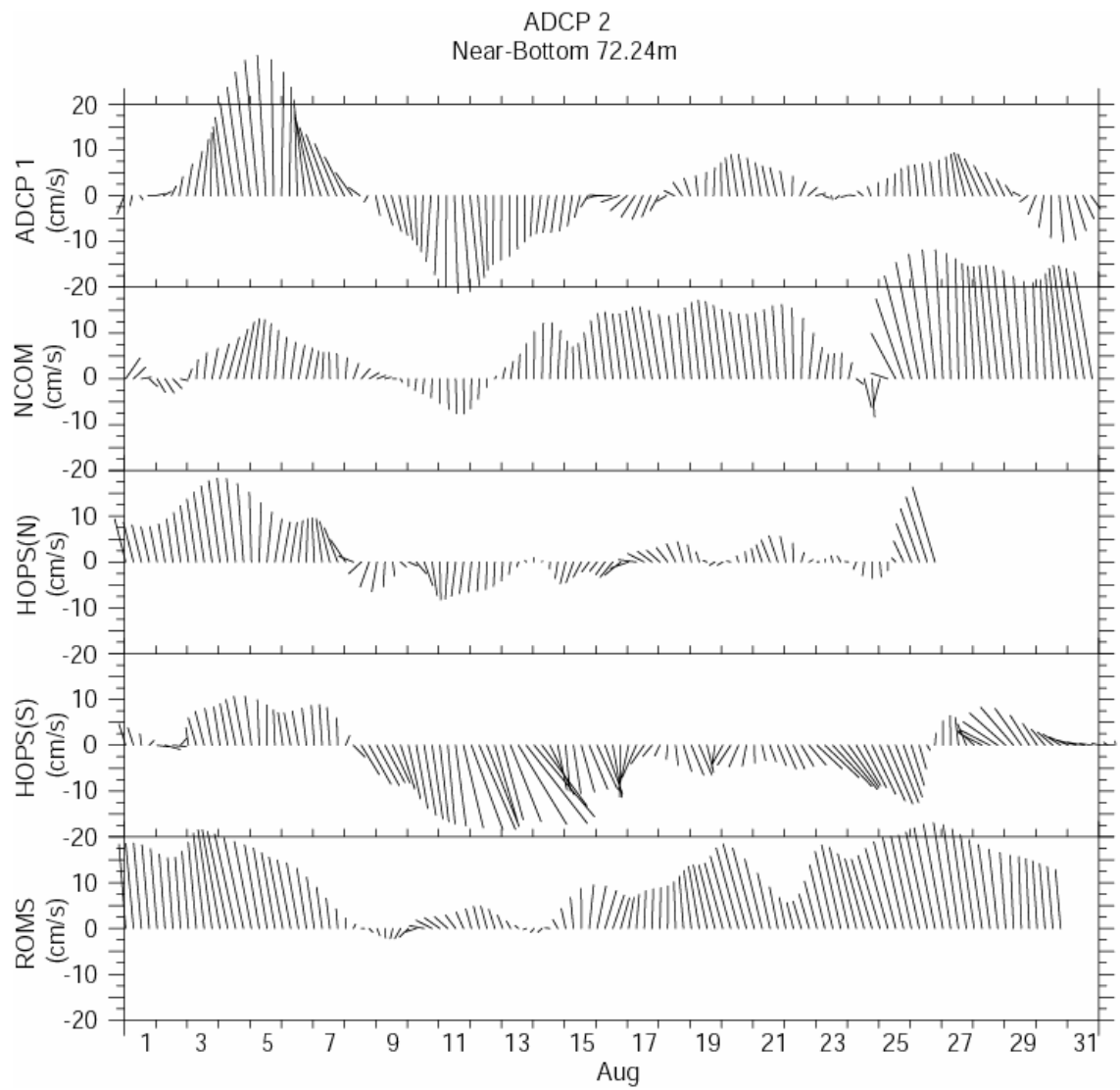


Figure 31. Stick vector plots comparing near-bottom currents at ADCP 2 with the four numerical models.

Model and ADCP Time Series
Center Box
ADCP 1 Surface Currents 10.25m

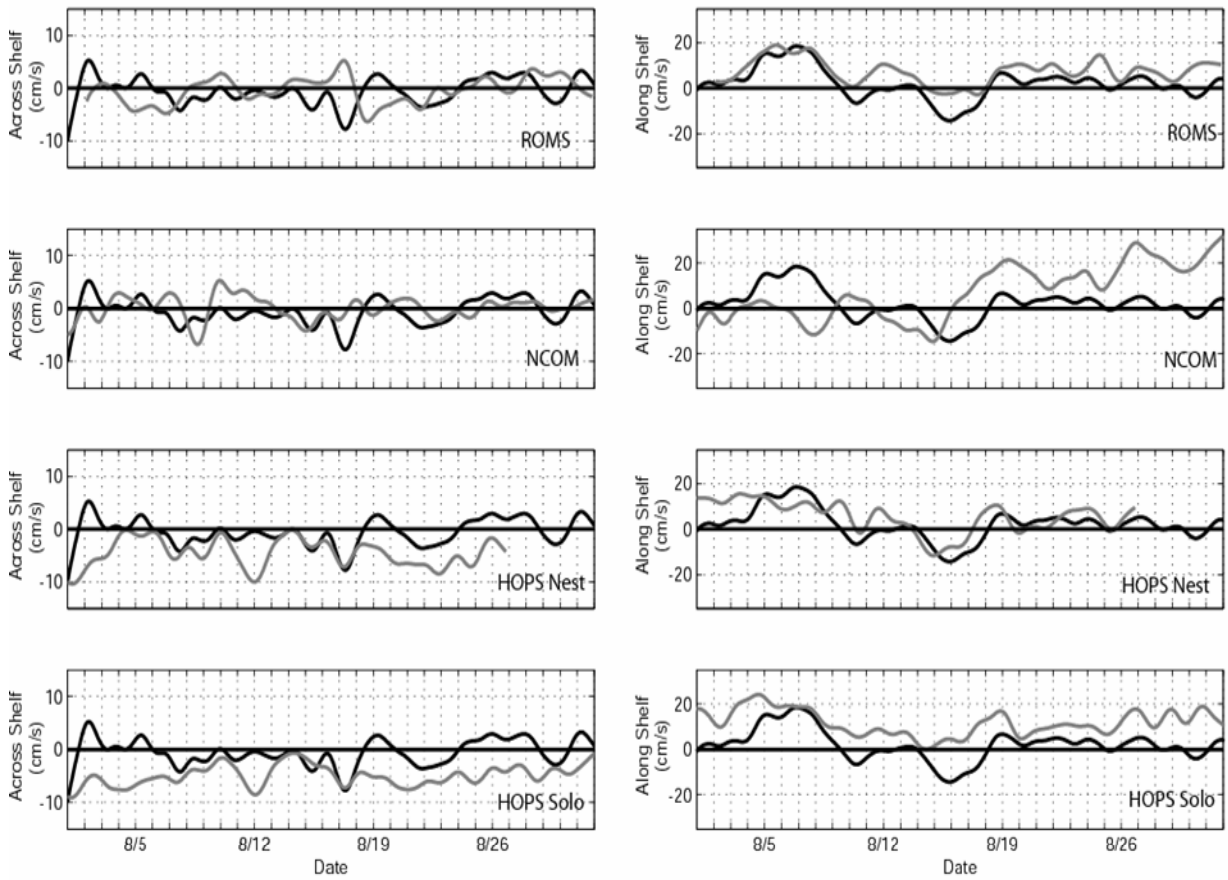


Figure 32. Spatial comparisons between the numerical models and ADCP time series for surface currents at ADCP 1. The gray line is the model time series and the black line is the ADCP time series. The across-shelf components form the left column and the alongshelf components are on the right.

Model and ADCP Time Series
Center Box
ADCP 1 Mid-Depth Currents 34.25m

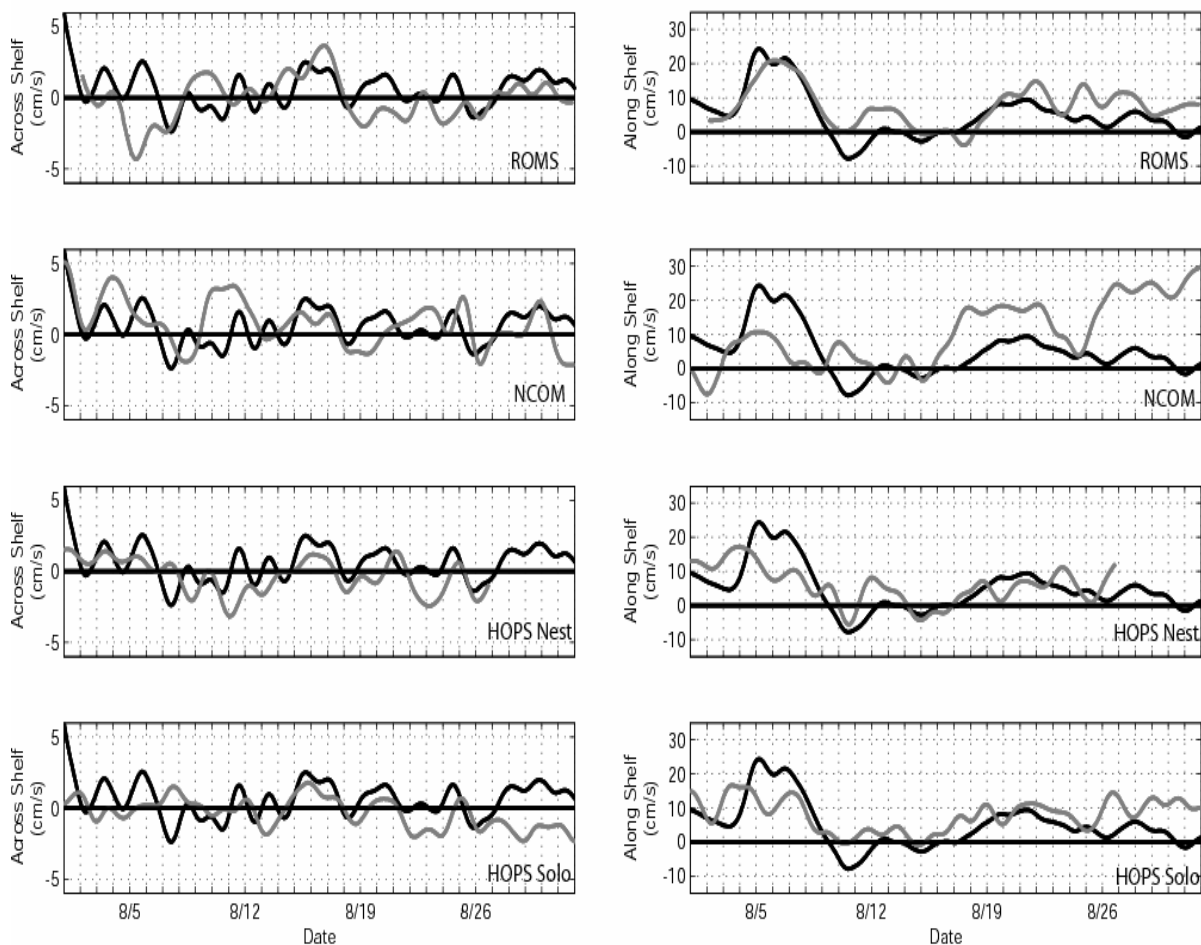


Figure 33. Spatial comparisons between the numerical models and ADCP time series for mid-depth currents at ADCP 1. The gray line is the model time series and the black line is the ADCP time series. The across-shelf components form the left column and the alongshelf components are on the right.

Model and ADCP Time Series
Center Box
ADCP 1 Near-Bottom Currents 46.25m

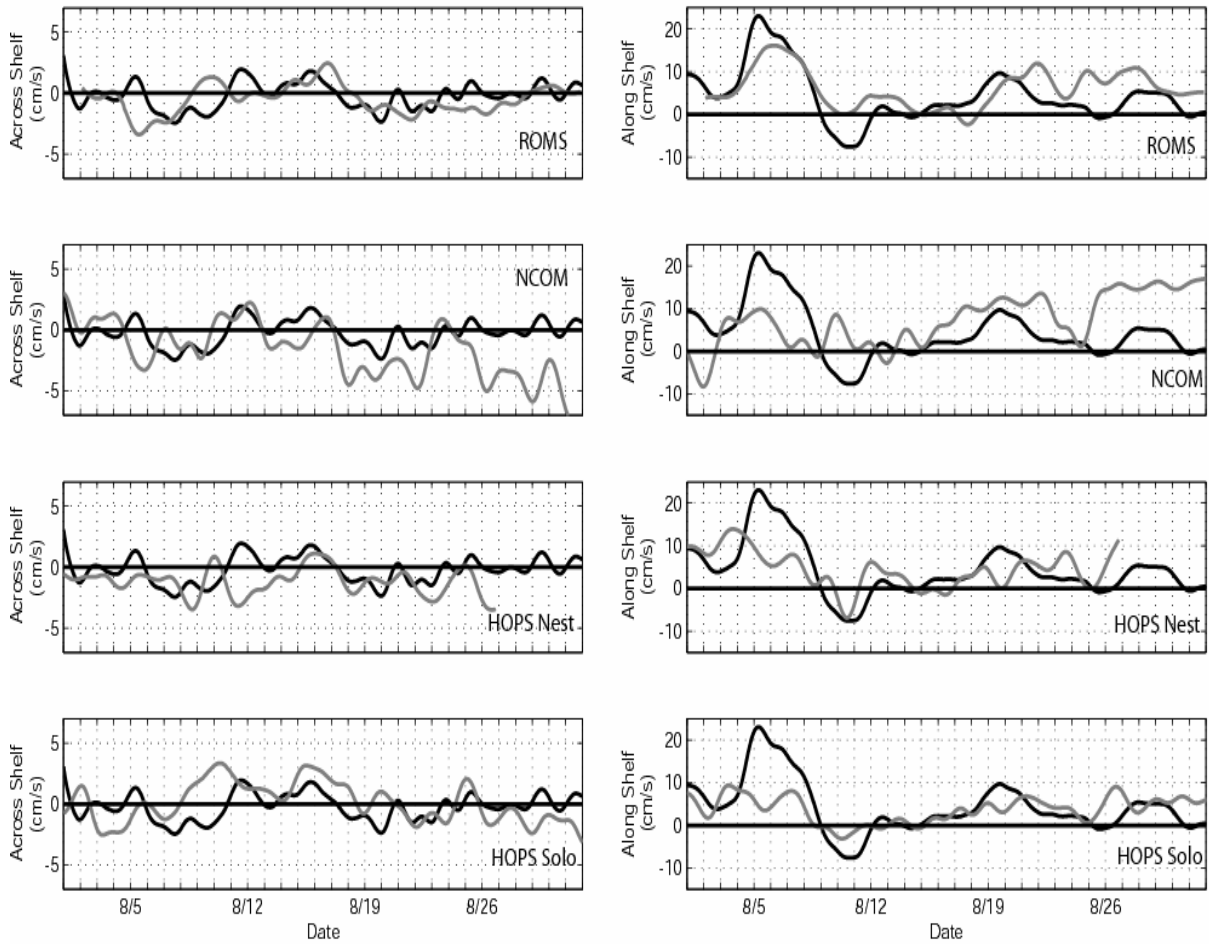


Figure 34. Spatial comparisons between the numerical models and ADCP time series for near-bottom currents at ADCP 1. The gray line is the model time series and the black line is the ADCP time series. The across-shelf components form the left column and the alongshelf components are on the right.

Model and ADCP Time Series
Center Box
ADCP 2 Surface Currents 12.24m

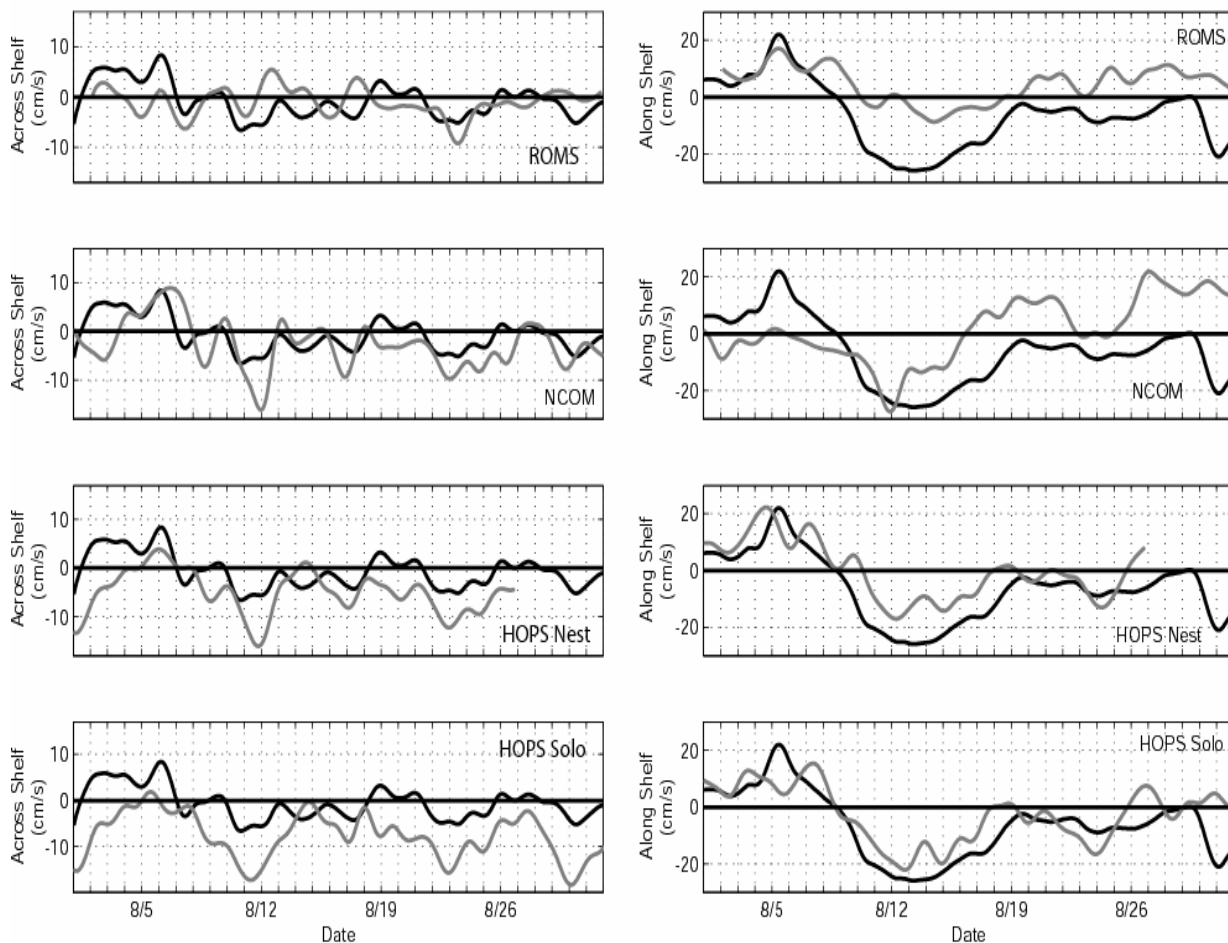


Figure 35. Spatial comparisons between the numerical models and ADCP time series for surface currents at ADCP 2. The gray line is the model time series and the black line is the ADCP time series. The across-shelf components form the left column and the alongshelf components are on the right.

Model and ADCP Time Series
Center Box
ADCP 2 Mid-Depth Currents 52.24m

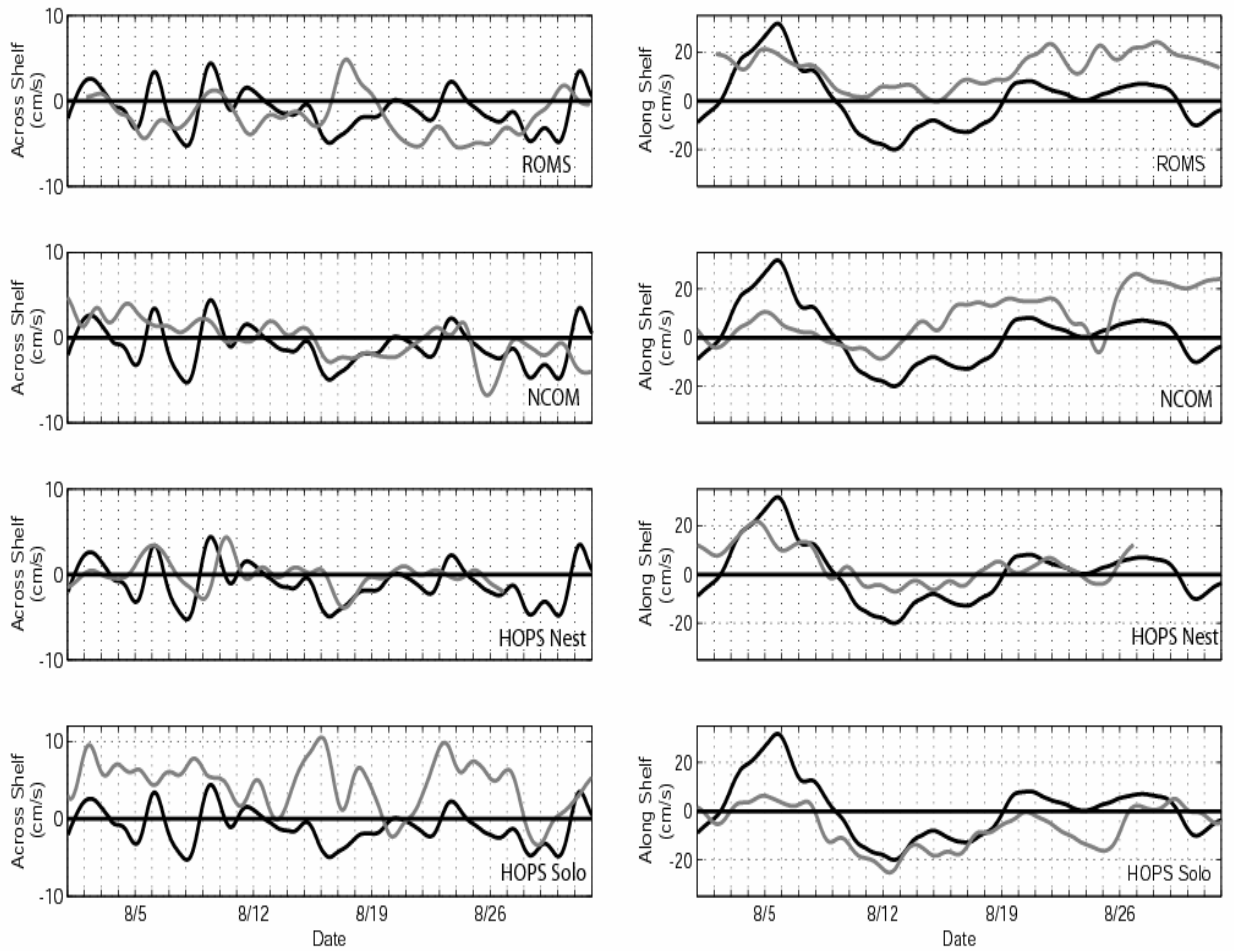


Figure 36. Spatial comparisons between the numerical models and ADCP time series for mid-depth currents at ADCP 2. The gray line is the model time series and the black line is the ADCP time series. The across-shelf components form the left column and the alongshelf components are on the right.

Model and ADCP Time Series
Center Box
ADCP 2 Near-Bottom Currents 72.24m

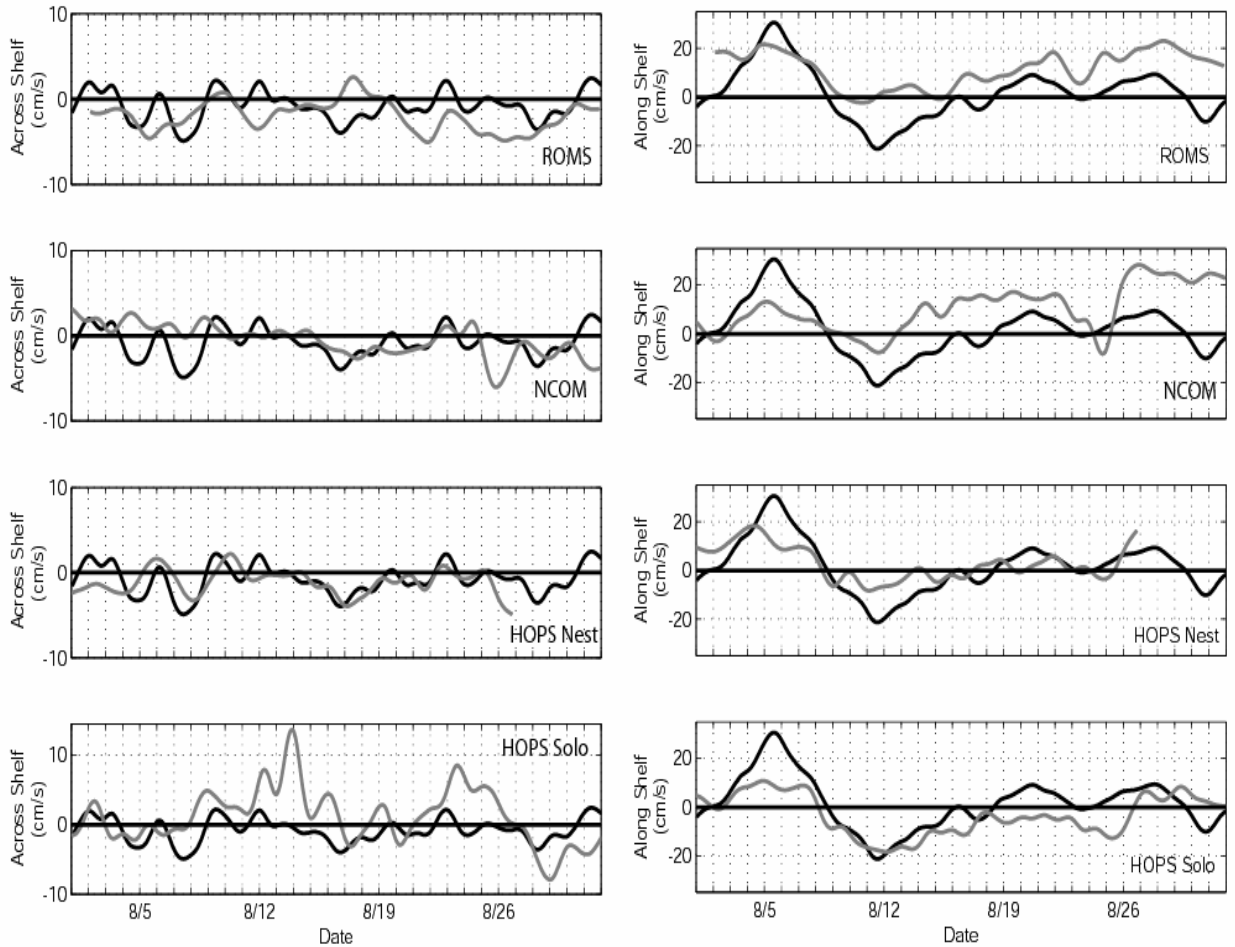


Figure 37. Spatial comparisons between the numerical models and ADCP time series for near-bottom currents at ADCP 2. The gray line is the model time series and the black line is the ADCP time series. The across-shelf components form the left column and the alongshelf components are on the right.

Model and ADCP Time Series
Center Box with Corresponding Lag
ADCP 1 Surface Currents 10.25m

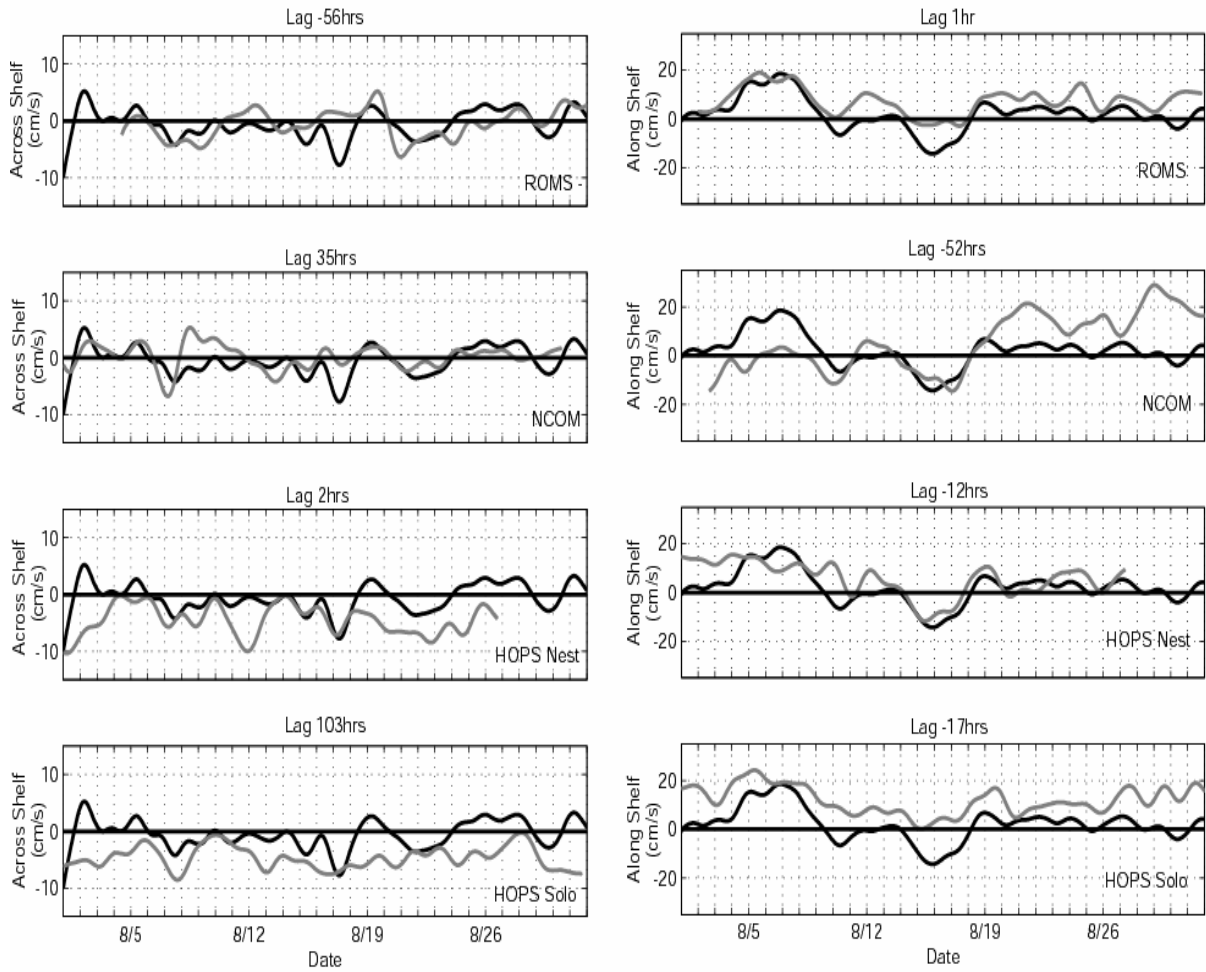


Figure 38. As in Figure 32, but with the series aligned better according to the cross-correlation results. The model output has been shifted forward/back according to the lag/lead estimated from the peak in the cross-correlation function.

Model and ADCP Time Series
Center Box with Corresponding Lag
ADCP 1 Mid-Depth Currents 34.25m

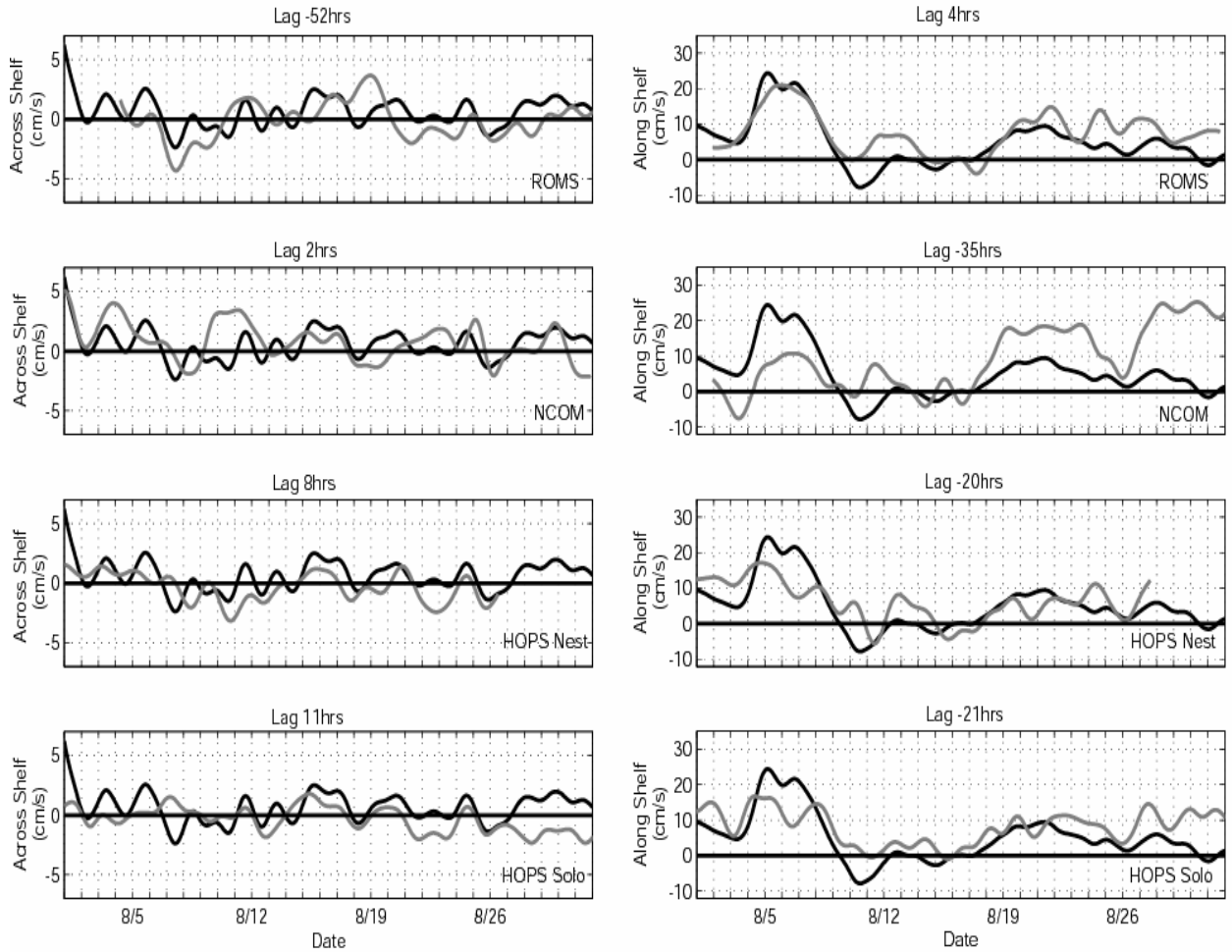


Figure 39. As in Figure 33, but with the series aligned better according to the cross-correlation results. The model output has been shifted forward/back according to the lag/lead estimated from the peak in the cross-correlation function.

Model and ADCP Time Series
Center Box with Corresponding Lag
ADCP 1 Near-Bottom Currents 46.25m

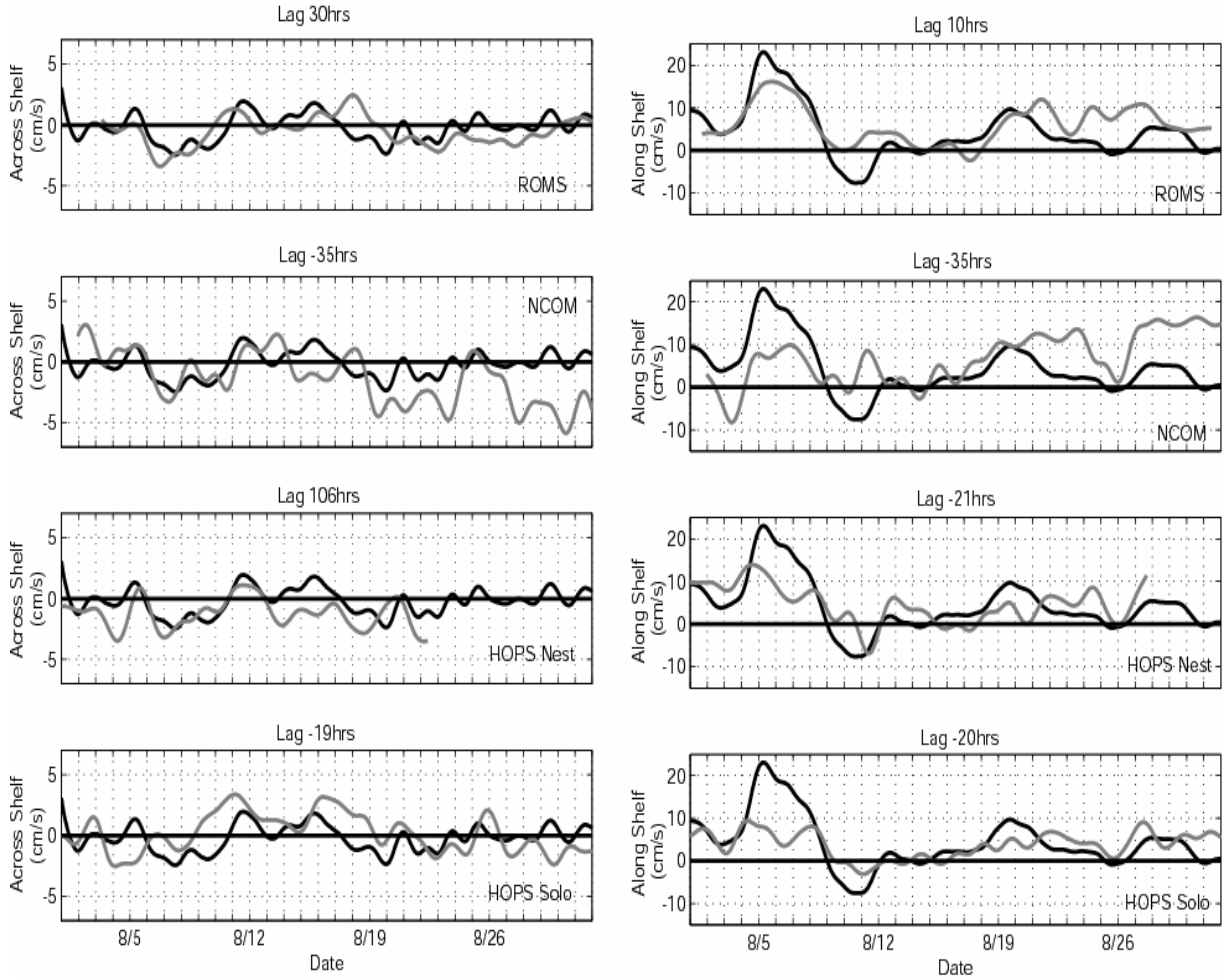


Figure 40. As in Figure 34, but with the series aligned better according to the cross-correlation results. The model output has been shifted forward/back according to the lag/lead estimated from the peak in the cross-correlation function.

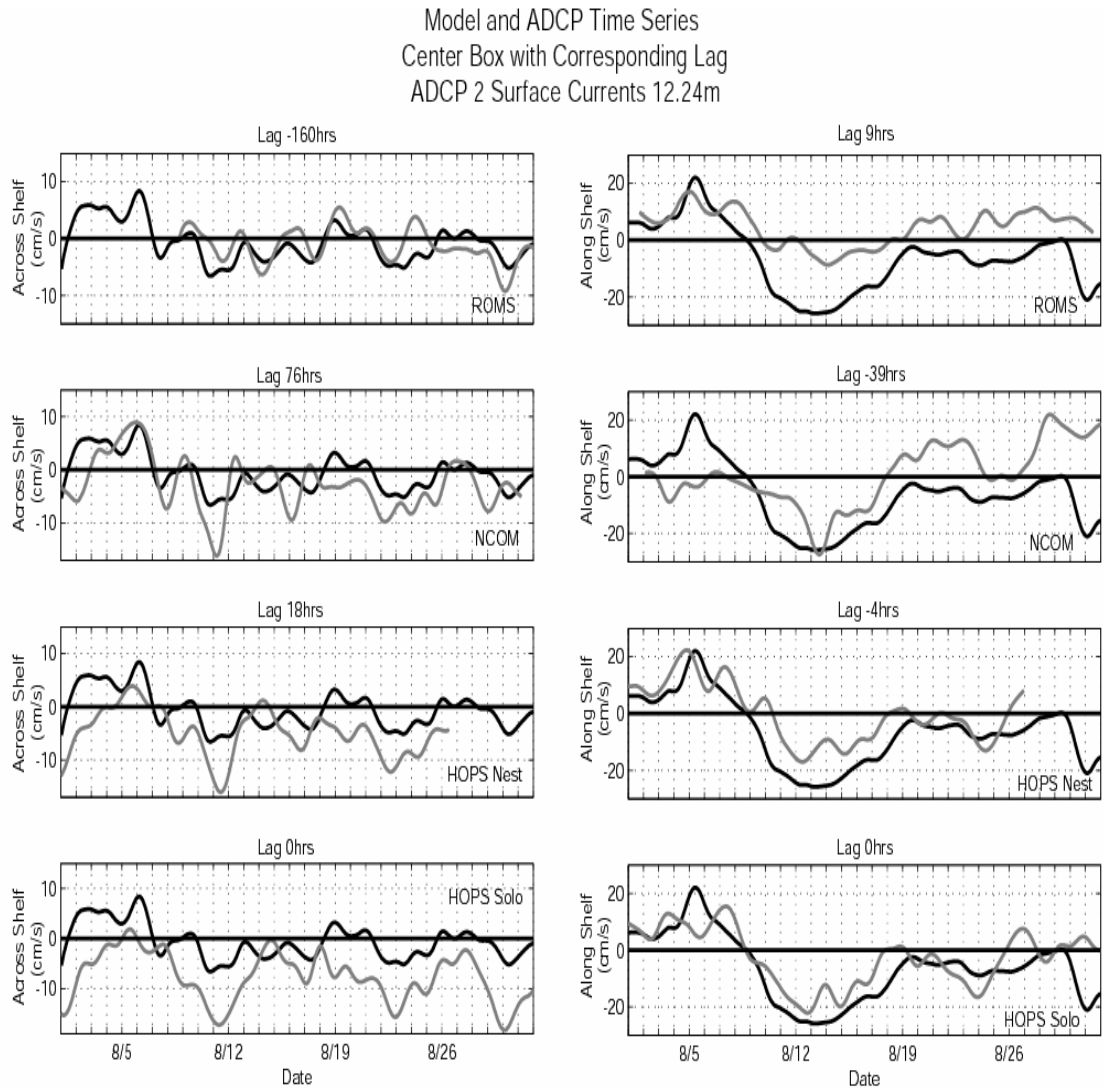


Figure 41. As in Figure 35, but with the series aligned better according to the cross-correlation results. The model output has been shifted forward/back according to the lag/lead estimated from the peak in the cross-correlation function.

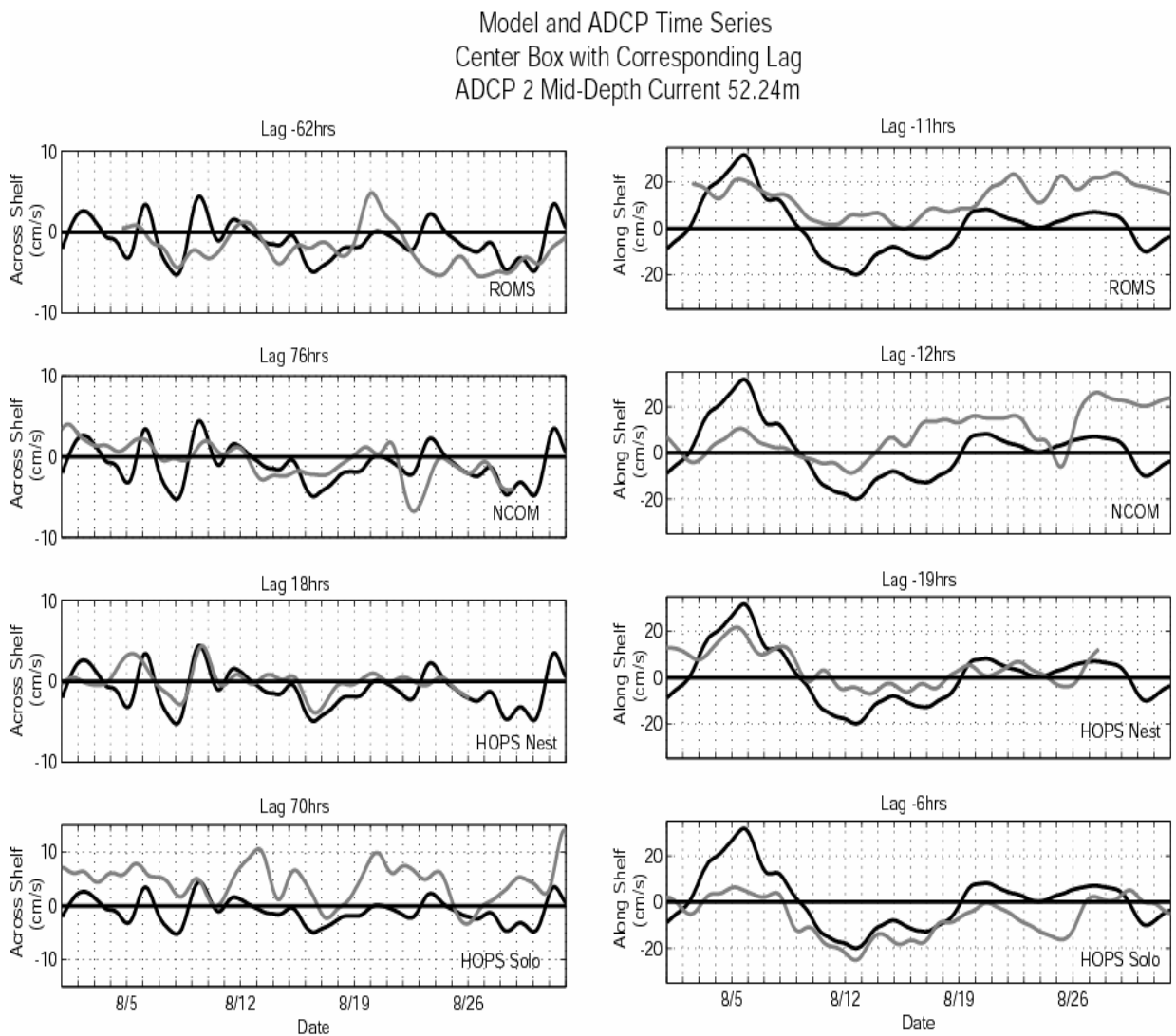


Figure 42. As in Figure 36, but with the series aligned better according to the cross-correlation results. The model output has been shifted forward/back according to the lag/lead estimated from the peak in the cross-correlation function.

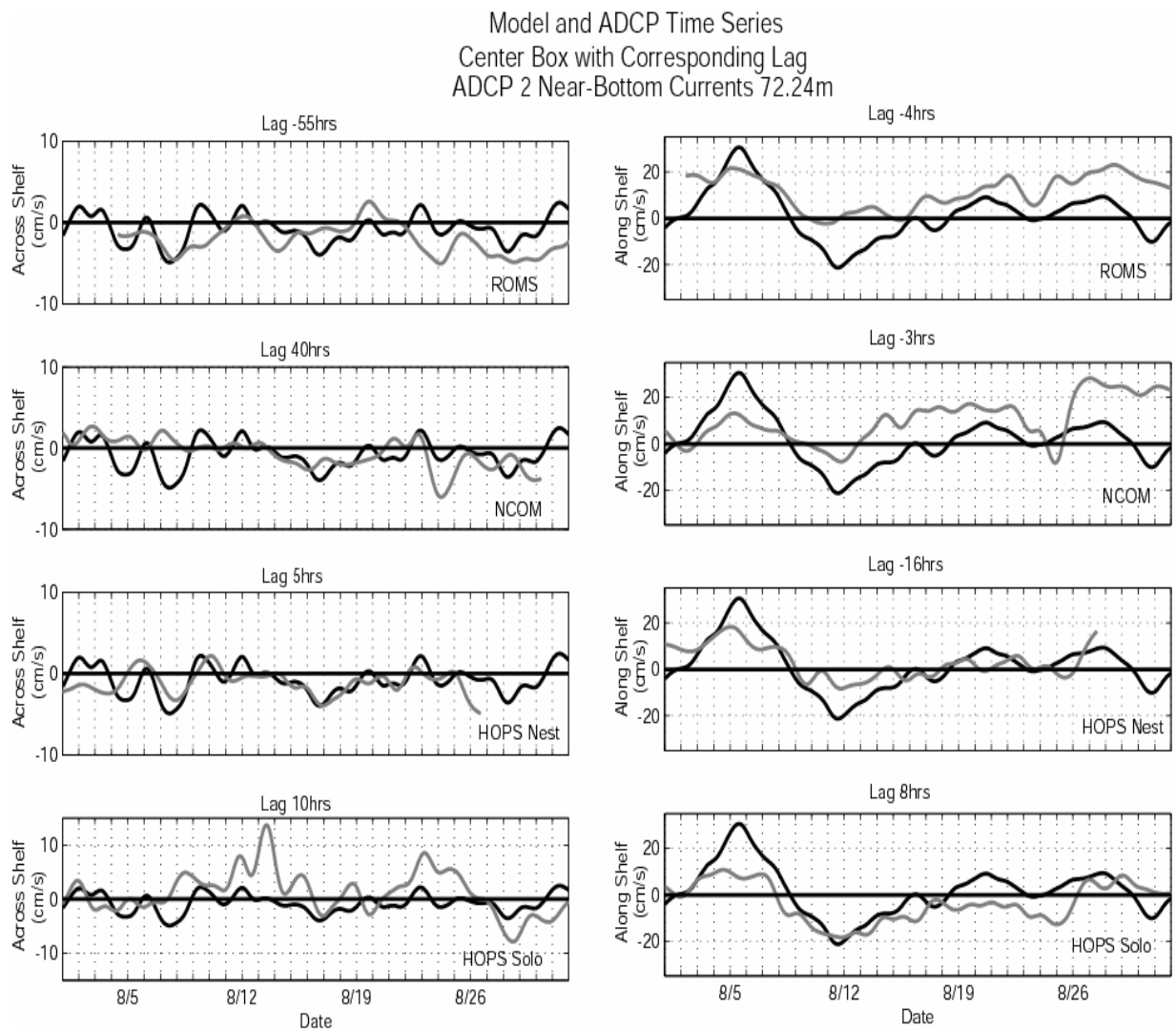


Figure 43. As in Figure 37, but with the series aligned better according to the cross-correlation results. The model output has been shifted forward/back according to the lag/lead estimated from the peak in the cross-correlation function.

Model and ADCP Time Series
Optimal Correlations with Lag
ADCP 1 Surface Currents 10.25m

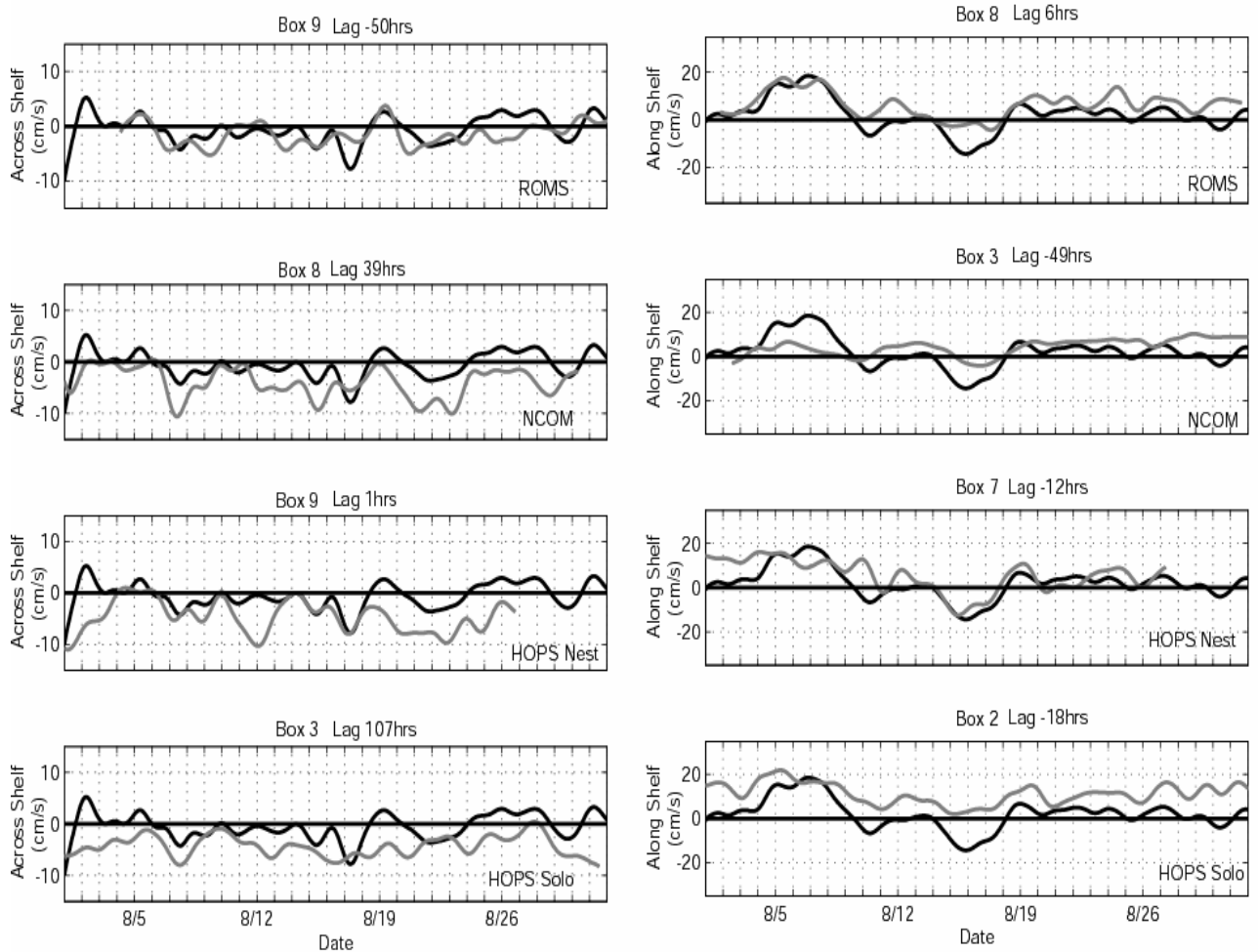


Figure 44. Optimal space/time lagged data producing the highest correlations and minimal rms error between the model output and the data at ADCP 1. For example, the alongshelf ROMS data was best at grid point 8, lagged back by 6 hours.

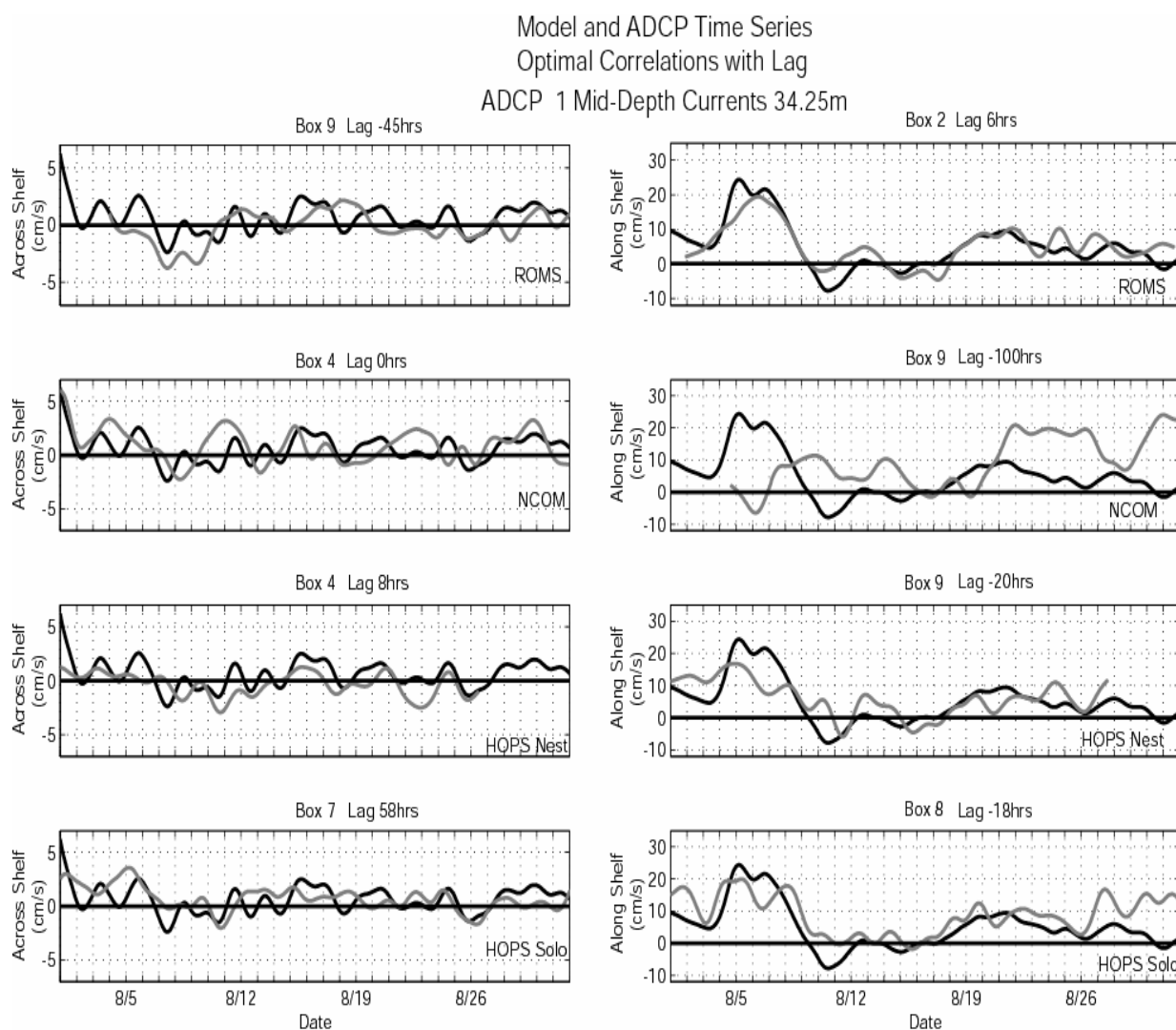


Figure 45. Optimal space/time lagged data producing the highest correlations and minimal rms error between the model output and the data at ADCP 1. For example, the alongshelf ROMS data was best at grid point 2, lagged back by 6 hours.

Model and ADCP Time Series
Optimal Correlations with Lag
ADCP 1 Near-Bottom Currents 46.25m

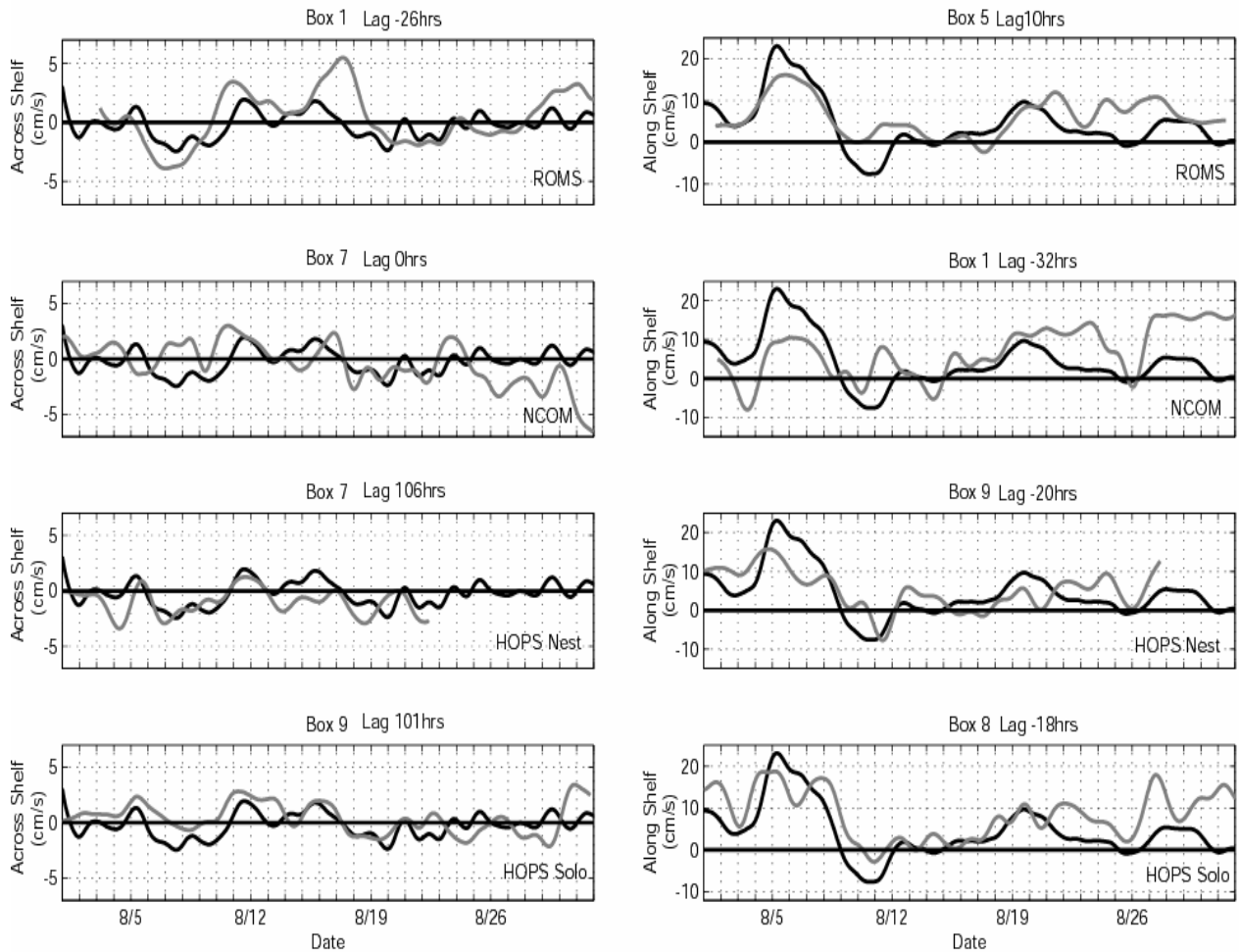


Figure 46. Optimal space/time lagged data producing the highest correlations and minimal rms error between the model output and the data at ADCP 1. For example, the alongshelf ROMS data was best at grid point 5, lagged back by 10 hours.

Model and ADCP Time Series
Optimal Correlations with Lag
ADCP 2 Surface Currents 12.24m

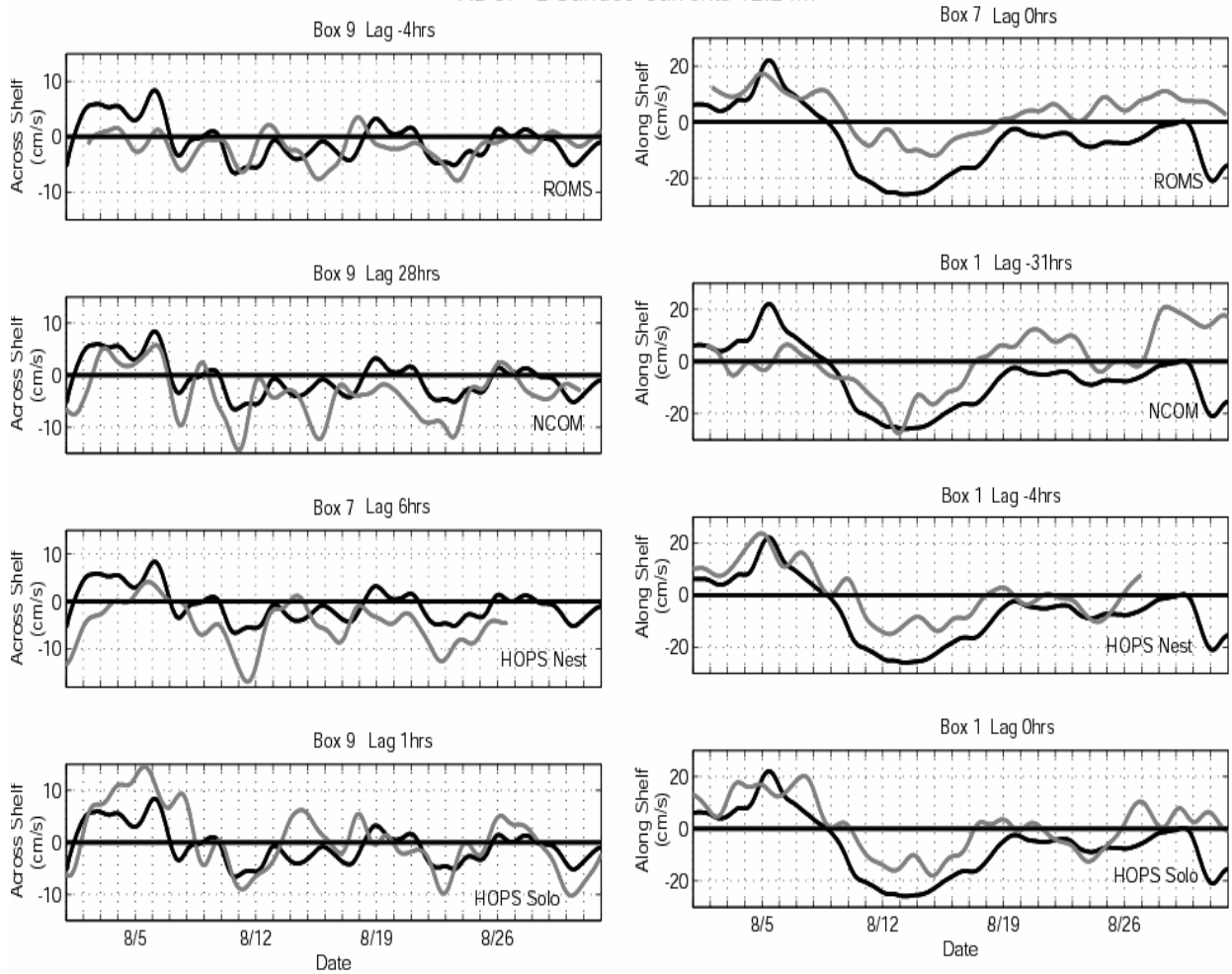


Figure 47. Optimal space/time lagged data producing the highest correlations and minimal rms error between the model output and the data at ADCP 2. For example, the alongshelf ROMS data was best at grid point 7, lagged by 0 hours.

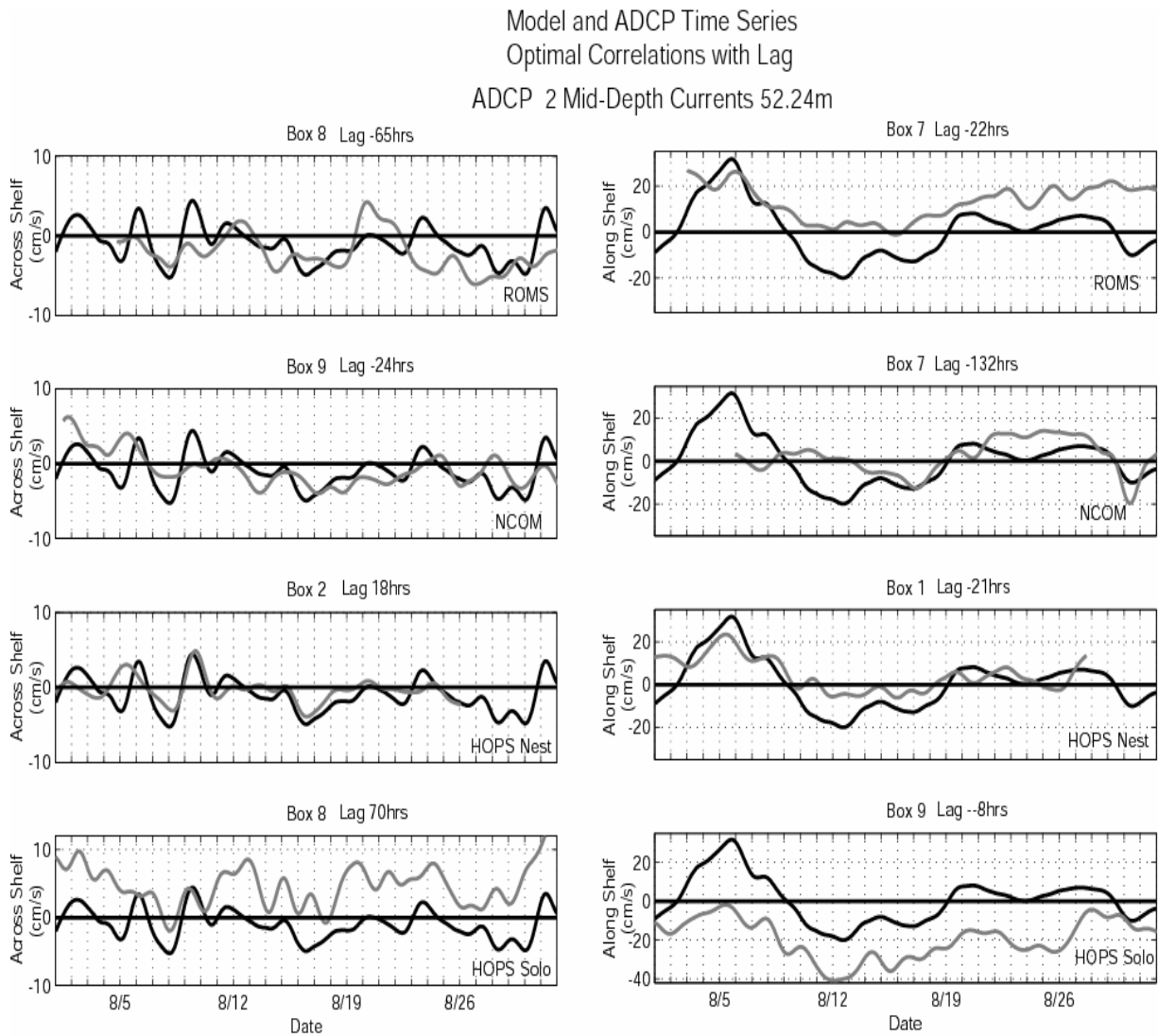


Figure 48. Optimal space/time lagged data producing the highest correlations and minimal rms error between the model output and the data at ADCP 2. For example, the alongshelf ROMS data was best at grid point 7, lagged ahead by 22 hours.

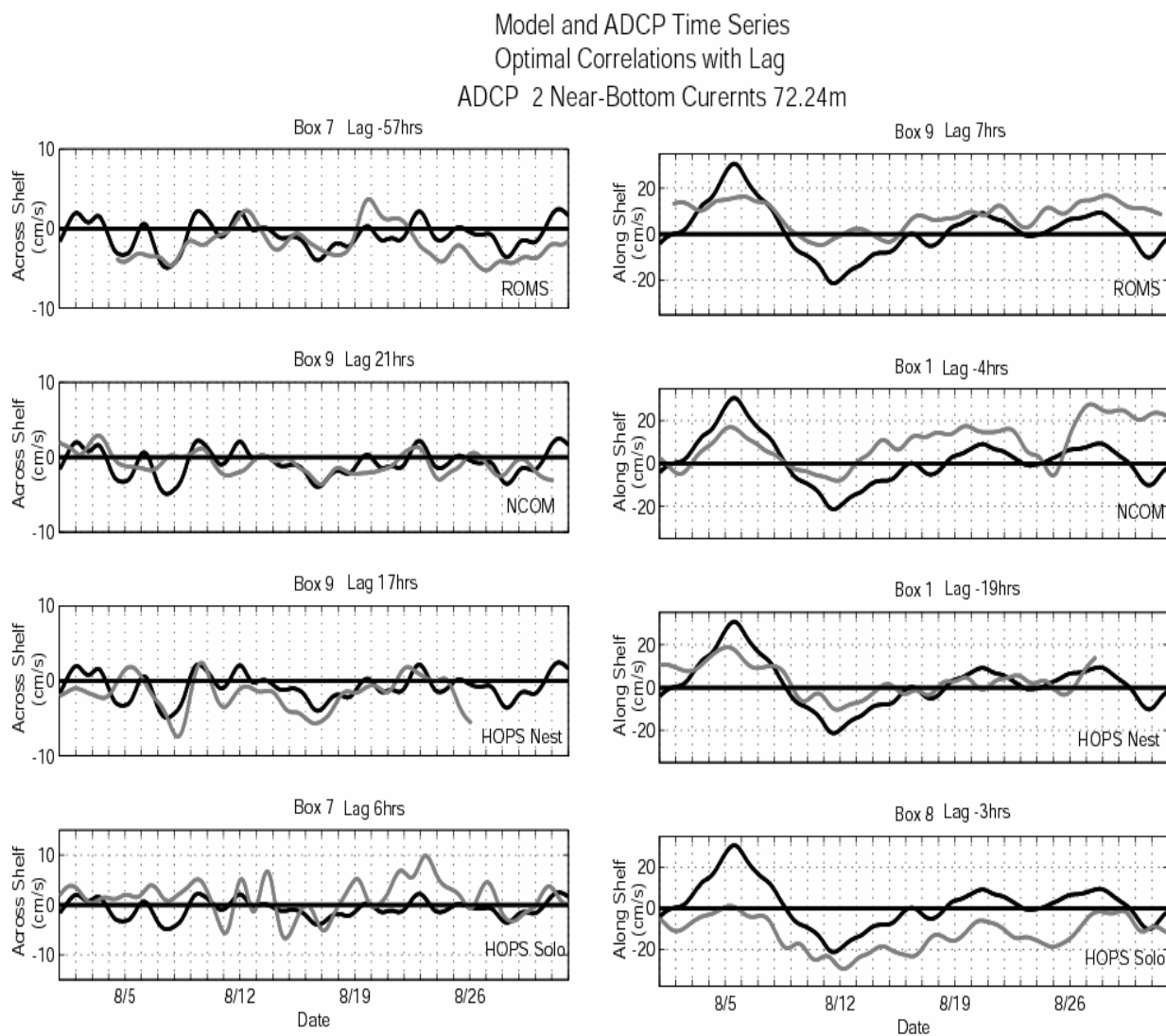


Figure 49. Optimal space/time lagged data producing the highest correlations and minimal rms error between the model output and the data at ADCP 2. For example, the alongshelf ROMS data was best at grid point 9, lagged back by 7 hours.

THIS PAGE INTENTIONALLY LEFT BLANK

APPENDIX B. TABLES

Summary of Key Features for the three ocean models (HOPS, ROMS and NCOM/ICON) used during the MB06 real-time operations			
Features	HOPS PIs: Allan Robinson robinson@ pacific.deas.harvard.edu Pierre Lermusiaux pierrel@ pacific.harvard.edu	ROMS PI: Yi Chao Yi.Chao @jpl.nasa.gov	NCOM/ICON PI: Igor Shulman Igor.Shulman@ nrlssc.navy.mil
Physical modeling component			
Model Domain	2-way nested (Mon-Bay/ San Fr. domain and Pt AN domain) Four-corner points: Mon-Bay/San Fr. domain NW: 123.97W, 37.187N NE: 122.53W, 37.876N SW: 122.62W, 35.403N SE: 121.19W, 36.092N Pt AN domain NW: 122.84W, 37.144N NE: 122.33W, 37.389N SW: 122.44W, 36.614N SE: 121.93W, 36.860N 1.5 km and 0.5 km resolutions Grid-point: Mon-Bay /San Fr.: 100x155 Pt AN: 107 x 138	Inner domain of a 3-level 1-way nested system Four-corner points: NW: 123.58W; 37.432N NE: 122.036W; 37.83N SW: 122.547W; 35.104N SE: 121.048W; 35.57N About 1.5 km resolution in Curvilinear-orthogonal grids Gridpoint:179x83	NCOM ICON (notation p012) model is one-way coupled to 9km NCOM California Current Model (NCOM CCS), which is one way coupled to 1/8 degree global NCOM model. Four-corner points over water: NW:123.2W, 36.9N NE:122.47W,37.44N SW:122.5W, 35.6N SE:121.43W, 35.86N Curvilinear-orthogonal grid with 1-4 km resolution, 81x53 grid points. NCOM frsICON (notation p022) is one way coupled to NCOM ICON model. Curvilinear-orthogonal grid with 0.5 – 1.5 km res. 114x97 grid
Vertical levels	30 double sigma	32 stretched sigma	Currently 30 sigma. NCOM ICON version with 41 sigma-Z vertical levels is being tested.
Horizontal mixing	Scale-selective Shapiro filter for numerical diffusion	Standard second order diffusion	Smagorinsky formulation
Vertical mixing	Vertical: Laplacian mixing, with viscosities and	K-Profile Parameterization	Mellor-Yamada 2.5 scheme

Summary of Key Features for the three ocean models (HOPS, ROMS and NCOM/ICON) used during the MB06 real-time operations			
	diffusivities estimated using (i) a simple turbulent mixing-layer model from the surface to a ``Ekman`` depth a function of the local wind-stress and (ii) below this wind mixing layer, a formulation based on Pacanowski and Philander (uses the local gradient Richardson number Ri)	(KPP)	
Initial conditions	Multiple initial states and dates have been utilized. Presently, the most successful IC is an initialization on July 27, based on: Synoptic (Mesoscale) state: hydrographic data (Glider, NPS-SST) between Jul 22 2006 and Jul 31 2006 (as available on the COOP web-site on 08-11), with a 3 day decorrelation time. Mean (Larger-scale) state: the above synoptic data and the Pt Sur CTD's Wecoma CTD's (up to Aug 8) few GTSSP CTD profiles for July 2006 Initial Surface Elevation and Barotropic Velocities set to sum of the standard geostrophic component and tidal component, and of data-based estimates of the undercurrent and of the CC at the open boundaries of the Mon-Bay-San Fr domain.	Climatology spinup to July 26, 2003 followed by COAMPS forcing	The NCOM ICON was initialized on July 11th of 2006 using fields from the regional model NCOM CCS and spun up with tidal forcing, with COAMPS 3km surface fluxes and with NCOM CCS on open boundaries. Starting from July 21th of 2006 available glider data are being assimilated.
Surface forcing			
Surface wind stress	3-km COAMPS wind stress; bi-cubically interpolated to HOPS grid	3-km COAMPS wind at 10-m computed with Large and Pond drag coefficient	3-km COAMPS wind stress
Air-sea heat flux	3-km COAMPS, bi-cubically interpolated to HOPS grid	3-km COAMPS radiative heat fluxes, bulk formula for sensible and latent heat fluxes	3-km COAMPS heat fluxes, short-wave flux penetrates water column. There is option for switch to bulk formulations

Summary of Key Features for the three ocean models (HOPS, ROMS and NCOM/ICON) used during the MB06 real-time operations			
Air-sea fresh-water flux	3-km COAMPS precipitation Evaporation derived from COAMPS latent heat flux using: $\text{Evap} = \text{HeatLatent}/(2.5008e6 - 2.3e3 * T_{\text{air}})$; T_{air} from COAMPS. All fields bi-cubically interpolated to HOPS	Climatology	3-km COAMPS (on or off)
River forcing	No	No	No (with the option to turn on)
Tides	Yes	Yes; There are three ROMS nowcast/forecast products: (1) 1.5-km ROMS without tides, (2) 1.5-km ROMS with tides, and (3) 600-m ROMS with tides	Yes
Open boundary conditions			
Open ocean boundary conditions	0.5km Pt AN domain: BCs provided by 1.5km Mon-Bay/San Fr. domain 1.5km Mon-Bay/San Fr. domain: Temp and Salt: combination of mapped data values and Orlanski radiation Internal Velocity: combination of data derived values and Orlanski radiation Surface pressure: combination of data derived values, OTIS tidal fields and Orlanski radiation Barotropic Momentum forcing: combination of data derived values, OTIS tidal fields and Orlanski radiation	1.5-km ROMS' BC is provided by 5-km ROMS; 5-km ROMS' BC is provided by 15-km ROMS; 15-km ROMS' BC is based on climatology and mixing Orlanski and Flather.	NCOM frsICON model BC are provided by NCOM ICON model. NCOM ICON'BC are provided by NCOM CCS model. NCOMCCS'BC are provided by the NCOM global model
Data assimilation			
Assimilation method	Optimal Interpolation or Error Subspace Statistical Estimation	3-dimensional variational method (3DVAR)	NRL Ocean Data Assimilation System (NCODA) (Multivariate Data Assimilation)
Assimilation window	12 hours (centered on 11 and 23 GMT, near colder and warmer SST times).	6 hours at 03, 09, 15, 21 GMT	12 hourly updates at 00Z and 12Z

Summary of Key Features for the three ocean models (HOPS, ROMS and NCOM/ICON) used during the MB06 real-time operations			
Observations being assimilated in the reanalysis			
CTDs	Pt Sur Wecoma Revelle	Pt. Sur	Pt. Sur
Gliders	SIO WHOI	SIO WHOI	SIO WHOI ASAP WHOI LOCO
NPS Aircraft SST	Yes	Yes	Yes
AUVs	Yes (Dorado, RU06)	Yes	Yes
Moorings: Temperature and Salinity	No	Yes	No
Moorings:ADCP	No	No	No
HF radars (CODAR)	No	No	No
Satellite data being assimilated in the reanalysis			
SST	No	Yes, along with AMSR-E for the 15- km ROMS	No in NCOM ICON and NCOM frsICON. The NCOMCCS assimilates TandS profiles and SST from the MODAS system. The MODAS TandS profiles and SST are derived from assimilation of altimeter SSH data; MCSST (Multi-Channel Sea Surface Temperature) and available in-situ Tand S profiles.
SSH	No	No in 1.5-km ROMS; Yes in 5-km and 15- km ROMS	No in NCOM ICON, or NCOM frsICON. Satellite SSHs are assimilated into the MODAS which is assimilated into the NCOM CCS and the NCOM global models.
Model Outputs			
T, S, u, v (including surface current)	Yes, netCDF files are provided daily. Each file contains: nowcast through 48-hour	Yes, netCDF files are provided every 6 hours for nowcast and every	Yes (with SSH), netCDF files are provided daily around 9AM PDT with

Summary of Key Features for the three ocean models (HOPS, ROMS and NCOM/ICON) used during the MB06 real-time operations			
provided to MBARI for analysis and comparisons	forecast fields. Files are provided both at twice daily and hourly time-resolutions.	24 hours for the 48-hour forecast fields	00Z and 12Z nowcasts and 33-hour forecast fields
LCS calculation and results	Yes.	Yes.	No
Web site with model images and movies	http://oceans.deas.harvard.edu/ASAP/index_ASAP.html	http://ocean.jpl.nasa.gov/MB06	http://www7320.nrlssc.navy.mil/ccsnrt

Table 1. Comparative table for the numerical models used during the ASAP project (From <http://aosn.mbari.org/coop/>, last accessed February 2007).

	ADCP 1		ADCP 2	
Depth	Mean	Std Dev	Mean	Std Dev
Surface 10 (12) m	(-0.57,2.05)	(2.47,6.84)	(-.68,-6.68)	(3.41,11.70)
Mid-depth 24 (52) m	(0.59,4.84)	(1.20,6.88)	(-.93,0.57)	(2.22,11.80)
Near-bottom 46 (72) m	(-0.22,4.17)	(1.06,6.27)	(-.80,1.69)	(1.80,10.35)

Table 2. Means and standard deviations from the ADCP data. Statistics are reported as across-shelf, alongshelf.

Component Correlations				
	Max Across-shelf	Sgn. Level	Max Alongshelf	Sgn. Level
Surface	0.48/-3	0.39	0.72/3	0.60
Mid Depth	<i>0.32/-197</i>	0.38	0.86/4	0.62
Near Bottom	0.50/51	0.39	0.86/1	0.58

Table 3. Correlation values between ADCP 1 and ADCP 2. The italicized numbers are statistically insignificant and the lags (hrs) are reported as the second number in the across-shelf and alongshelf components.

Vector Correlations	Magnitude	Orientation
Surface	0.7022	5.3028
Mid Depth	0.8258	-1.6107
Near Bottom	0.8347	-2.617

Table 4. Vector correlations for the cross correlation between ADCP 1 and ADCP 2. The magnitude describes the correlation between the two vectors while the orientation describes the angle between the vectors. A negative orientation indicates that ADCP 2 is to the right of ADCP 1.

ADCP 1					
Across-shelf					
	Period (days)	Period (hrs)	Coherence	Phase (deg)	Lag (hrs)
Surface (10.25m)	10.31	247.467	0.778	21.73	14.94
Along Shelf					
Mid Depth (34.25m)	10.31	247.467	0.737	28.18	19.37
Near Bottom (46.25m)	10.31	247.467	0.768	25.5	17.53

Table 5. Significant spectral peaks in the 5-10 day band from the cross spectra between the across-shelf wind and the across-shelf current and the alongshelf wind and the alongshelf current ADCP 1. A positive (negative) phase means wind leads (lags) the current. No data indicates no significant coherence in the 5-10 day band.

ADCP 2					
Alongshelf					
	Period (days)	Period (hrs)	Coherence	Phase (deg)	Lag (hrs)
Surface (12.24m)	10.31	247.467	0.811	44.33	30.47
Mid Depth (52.24m)	10.31	247.467	0.841	25.09	17.25
	5.16	123.733	0.863	28.07	9.65
Near Bottom (72.24m)	10.31	247.467	0.896	27.48	18.89
	5.16	123.733	0.78	35.44	12.18

Table 6. Significant spectral peaks from the alongshelf wind and the alongshelf current at ADCP 2. A positive (negative) phase means wind leads (lags) the current. There were no significant periods in the across-shelf component.

ADCP 2					
Along Shelf Wind/Across Shelf Current					
	Period (days)	Period (hrs)	Coherence	Phase	Lag(hrs)
Surface	10.31	247.467	0.911	14.25	9.80
	5.16	123.733	0.874	11.97	4.11
Mid Depth	NS	NS	NS	NS	NS
Near Bottom	10.31	247.467	0.804	-139.38	-95.81

Table 7. Significant spectral peaks from the cross spectra between the alongshelf wind and the across-shelf current for both mooring locations. A positive (negative) phase means wind leads (lags) the current. There were no significant periods at ADCP 1.

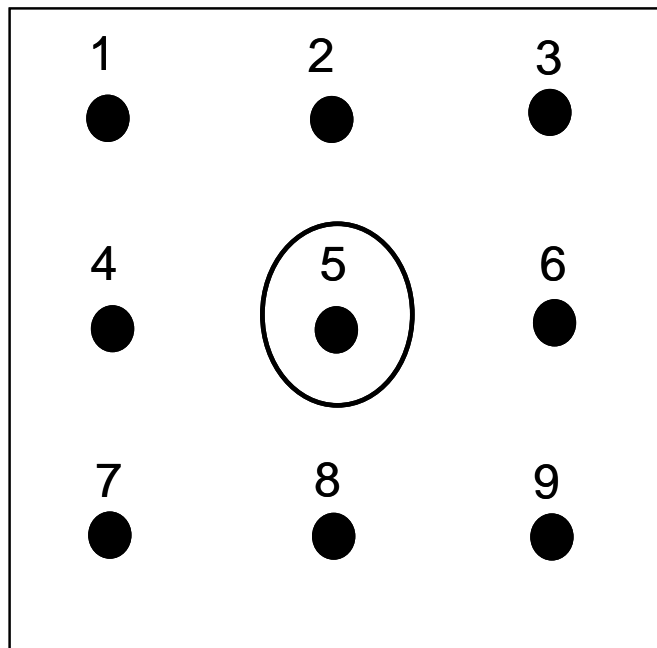


Table 8. The grid point locations for the model/data comparisons. The ADCP is at grid point 5.

NCOM Model
ADCP 1

Surface Currents 10.25m

Across-shelf Components				Alongshelf Components			
Correlation	0.2681	0.2533	0.433	Correlation	0.2403	0.2937	0.3138
RMS Error	3.2717	3.6062	2.4753	RMS Error	12.0045	11.2595	7.2351
Lag time (hrs)	29	-54	-45	Lag time (hrs)	-48	-47	-49
	0.3911	0.3664	0.4154		0.1807	0.1795	0.1921
	3.1497	2.6677	2.8473		13.332	12.7174	11.8622
	34	35	37		-47	-52	-46
	0.5199	0.5641	0.49		0.1743	0.1316	0.1112
	4.0476	4.0393	4.9431		12.8082	13.2805	13.6405
	36	39	45		-49	-56	-56

Mid Depth 34.25m

Across-shelf Components				Alongshelf Components			
Correlation	0.2832	0.24	NaN	Correlation	0.2007	0.2239	NaN
RMS Error	1.9993	2.591	NaN	RMS Error	10.827	7.6353	NaN
Lag time (hrs)	0	123	-200	Lag time (hrs)	-33	-40	-200
	0.3821	0.2729	0.2053		0.1462	0.1611	0.143
	1.5628	1.7069	2.2867		11.9803	11.3854	8.1157
	0	2	-102		-33	-35	-45
	0.3177	0.2801	0.3557		0.1063	0.0997	0.3557
	2.1686	2.6068	3.6774		11.661	12.9044	3.6774
	0	-101	-100		-35	-33	-100

Near Bottom 46.25m

Across-shelf Components				Alongshelf Components			
Correlation	0.1808	NaN	NaN	Correlation	0.2496	NaN	NaN
RMS Error	1.6629	NaN	NaN	RMS Error	8.3452	NaN	NaN
Lag time (hrs)	-97	-200	-200	Lag time (hrs)	-32	-200	-200
	0.3711	0.2241	NaN		0.1888	0.1783	NaN
	1.624	2.376	NaN		1.6286	8.2956	NaN
	0	-35	-200		-26	-35	-200
	0.4667	0.4083	0.2711		0.1202	0.1196	0.0922
	1.5961	2.3711	3.1873		11.3017	11.8169	9.5545
	0	0	-41		-29	-26	-30

Table 9. Computed correlation values, RMS errors and lag times (hrs) for the NCOM model at ADCP 1. The shaded grid points are insignificant and the bolded numbers are the highest/optimal correlations in the grid.

NCOM Model
ADCP 2

Surface Currents 12.24m

Across-shelf Components				Alongshelf Components			
Correlation	0.6423	0.5742	0.4969	Correlation	0.4358	0.3659	0.2664
RMS Error	4.4183	4.002	3.8022	RMS Error	13.8046	15.1099	16.596
Lag time (hrs)	1	7	21	Lag time (hrs)	-31	-31	-31
	0.6509	0.6326	0.6007		0.4114	0.3395	0.2547
	4.7147	4.3708	3.4955		12.9178	14.8002	16.3248
	6	18	24		-45	-39	-35
	0.5959	0.6405	0.6785		0.3467	0.3467	0.2513
	5.6864	5.3692	4.4585		13.5706	13.5568	15.2431
	17	25	28		-44	-45	-42

Mid Depth 52.24m

Across-shelf Components				Alongshelf Components			
Correlation	0.3413	0.3532	0.3782	Correlation	0.2982	0.2539	0.2298
RMS Error	2.6794	2.37	2.268	RMS Error	14.6745	16.2325	12.7521
Lag time (hrs)	78	73	50	Lag time (hrs)	-11	-8	-139
	0.4013	0.3805	0.3632		0.276	0.2496	0.2438
	2.4315	2.2224	2.4435		11.2143	12.0085	12.2776
	78	76	-16		-143	-146	-147
	0.2554	0.3345	0.437		0.3478	0.3106	0.2652
	2.6909	2.7756	2.246		9.8979	10.924	11.5842
	79	-25	-24		-132	-140	-147

Near Bottom 72.24m

Across-shelf Components				Alongshelf Components			
Correlation	0.2045	0.2787	0.2837	Correlation	0.4122	0.3771	0.3509
RMS Error	2.4741	2.0634	2.7032	RMS Error	13.7518	14.875	11.9281
Lag time (hrs)	54	57	29	Lag time (hrs)	-4	-2	-8
	0.2005	0.1724	0.2912		0.3758	0.307	0.2379
	2.4305	2.2128	1.8423		12.5527	14.7149	15.1506
	47	40	26		-6	-3	-3
	0.2295	0.1488	0.3349		0.2936	0.2525	0.1624
	2.8181	2.3357	1.7052		11.9181	13.5378	15.175
	46	28	21		-4	0	0

Table 10. Computed correlation values, RMS errors and lag times (hrs) for the NCOM model at ADCP 2. The shaded grid points are insignificant and the bolded numbers are the highest/optimal correlations in the grid.

ROMS Model
ADCP 1

Surface Currents 10.25m

Across-shelf Components				Alongshelf Components			
Correlation	0.2221	0.3654	0.1062	Correlation	0.8448	0.8233	0.6065
RMS Error	2.8892	2.6998	3.9701	RMS Error	5.0072	7.2178	11.6067
Lag time (hrs)	137	-63	-58	Lag time (hrs)	8	-3	-10
	0.2473	0.3307	0.3067		0.8257	0.855	0.7213
	3.2102	2.7299	3.0312		4.9397	6.5355	10.5216
	142	-56	-57		9	1	-5
	0.2786	0.2484	0.4467		0.7922	0.8582	0.7438
	3.1122	2.696	2.3654		5.0231	5.7496	10.1405
	144	-50	-50		12	6	-2

Mid Depth 34.25m

Across-shelf Components				Alongshelf Components			
Correlation	0.3452	0.3429	NaN	Correlation	0.6972	0.8681	NaN
RMS Error	1.9444	1.7801	NaN	RMS Error	6.7749	3.5366	NaN
Lag time (hrs)	-50	-52	-200	Lag time (hrs)	6	5	-200
	0.3699	0.3958	NaN		0.657	0.819	NaN
	1.9477	1.6331	NaN		7.2904	4.9045	NaN
	-56	-52	-200		6	4	-200
	0.3965	0.4006	0.4312		0.6178	0.7752	0.8527
	1.8059	1.5593	1.4796		7.8495	6.1131	3.972
	-58	-59	-45		6	6	5

Near Bottom 46.25m

Across-shelf Components				Alongshelf Components			
Correlation	0.5706	NaN	NaN	Correlation	0.7028	NaN	NaN
RMS Error	1.9324	NaN	NaN	RMS Error	6.6455	NaN	NaN
Lag time (hrs)	-26	-200	-200	Lag time (hrs)	12	-200	-200
	0.4821	0.4372	NaN		0.6045	0.7329	NaN
	1.8358	1.2452	NaN		8.1336	4.7331	NaN
	-31	-30	-200		11	10	-200
	0.3596	0.3764	NaN		0.5226	0.7082	NaN
	1.9981	1.4151	NaN		9.3613	5.6206	NaN
	-34	-33	-200		12	12	-200

Table 11. Computed correlation values, RMS errors and lag times (hrs) for the ROMS model at ADCP 1. The shaded grid points are insignificant and the bolded numbers are the highest/optimal correlations in the grid. NaN (Not a Number) indicates no model output provided at that depth/location.

ROMS Model
ADCP 2

Surface Currents 12.24m

Across-shelf Components				Alongshelf Components			
Correlation	0.2896	0.278	0.227	Correlation	0.7936	0.8098	0.7522
RMS Error	3.5129	3.3138	3.1065	RMS Error	13.1086	13.3681	15.0507
Lag time (hrs)	-83	-83	-80	Lag time (hrs)	11	15	26
	0.2265	0.3127	0.2599		0.8376	0.8354	0.8164
	3.562	2.9007	2.6023		12.7267	13.2403	14.2621
	-160	-160	-161		4	9	13
	0.2569	0.3275	0.4502		0.8742	0.8678	0.8515
	3.222	2.8674	3.4192		12.0086	12.7519	13.7439
	-161	-161	-4		0	4	8

Mid Depth 52.24m

Across-shelf Components				Alongshelf Components			
Correlation	0.2563	0.1757	0.1174	Correlation	0.6748	0.6384	0.7675
RMS Error	2.9006	2.9736	2.7497	RMS Error	14.9609	14.6554	10.9102
Lag time (hrs)	101	-157	-41	Lag time (hrs)	-18	6	20
	0.2129	0.2123	0.1454		0.7356	0.6581	0.7518
	2.9105	2.9761	2.8852		14.5869	15.2473	11.8415
	97	-62	-26		-22	-11	19
	0.3084	0.3107	0.2276		0.7707	0.7108	0.7308
	2.7362	2.8385	2.9507		14.2309	15.2828	13.3195
	-63	-65	-64		-22	-18	9

Near Bottom 72.24m

Across-shelf Components				Alongshelf Components			
Correlation	0.22	0.143	NaN	Correlation	0.7585	0.7203	NaN
RMS Error	2.6394	2.4234	NaN	RMS Error	13.2089	11.6544	NaN
Lag time (hrs)	98	120	-200	Lag time (hrs)	-11	0	-200
	0.2183	0.1633	0.2081		0.7876	0.7485	0.7742
	2.591	2.504	1.8553		13.2133	12.2142	9.4973
	-58	-55	131		-17	-4	6
	0.3856	0.2857	0.102		0.7902	0.7615	0.7907
	2.3212	2.4927	2.0534		13.19	13.3766	9.4859
	-57	-57	-57		-17	-9	7

Table 12. Computed correlation values, RMS errors and lag times (hrs) for the ROMS model at ADCP 2. The shaded grid points are insignificant and the bolded numbers are the highest/optimal correlations in the grid. NaN (Not a Number) indicates no model output provided at that depth/location.

HOPS Solo
ADCP 1

Surface Currents 10.25m

Across-shelf Components				Alongshelf Components			
Correlation	0.2059	0.3271	0.3709	Correlation	0.7877	0.7998	0.781
RMS Error	3.4818	4.0767	4.2207	RMS Error	9.3815	9.9843	9.8934
Lag time (hrs)	15	105	107	Lag time (hrs)	-18	-18	-20
	0.2548	0.2958	0.2872		0.7945	0.7838	0.7638
	3.997	4.64	4.333		9.9579	10.5393	9.9173
	103	103	106		-16	-17	-18
	0.3417	0.3014	0.3117		0.7709	0.744	0.7218
	4.2578	5.148	5.0235		10.3139	10.107	8.8037
	2	0	-63		-14	-16	-17

Mid Depth 34.25m

Across-shelf Components				Alongshelf Components			
Correlation	NaN	0.2772	0.2346	Correlation	NaN	0.6173	0.6729
RMS Error	NaN	1.334	1.5414	RMS Error	NaN	5.6452	5.5276
Lag time (hrs)	-200	-102	9	Lag time (hrs)	-200	-25	-22
	0.242	0.1992	0.3094		0.6391	0.6651	0.677
	1.2967	1.7392	1.4418		5.6217	6.083	6.4097
	-105	11	9		-24	-21	-21
	0.4218	0.2098	0.1768		0.6748	0.6834	0.683
	1.208	1.5895	1.8845		6.6127	6.4621	6.0684
	58	133	124		-22	-20	-18

Near Bottom 46.25m

Across-shelf Components				Alongshelf Components			
Correlation	NaN	NaN	NaN	Correlation	NaN	NaN	NaN
RMS Error	NaN	NaN	NaN	RMS Error	NaN	NaN	NaN
Lag time (hrs)	-200	-200	-200	Lag time (hrs)	-200	-200	-200
	NaN	0.1787	0.2876		NaN	0.5934	0.6608
	NaN	1.7706	1.396		NaN	5.1045	5.4576
	-200	-19	101		-200	-20	-18
	0.2763	0.3897	0.475		0.6298	0.6609	0.6575
	1.663	1.2937	1.3149		5.5276	6.4549	6.6923
	98	100	101		-21	-18	-16

Table 13. Computed correlation values, RMS errors and lag times (hrs) for the HOPS Solo model at ADCP 1. The shaded grid points are insignificant and the bolded numbers are the highest/optimal correlations in the grid. NaN (Not a Number) indicates no model output provided at that depth/location.

HOPS Solo
ADCP 2

Surface Currents 12.24m

Across-shelf Components				Alongshelf Components			
Correlation	0.5452	0.5454	0.5996	Correlation	0.8283	0.7946	0.7294
RMS Error	4.2095	5.4592	6.8971	RMS Error	9.9418	11.0821	12.0466
Lag time (hrs)	0	0	0	Lag time (hrs)	0	0	27
	0.5772	0.6049	0.6719		0.8106	0.7689	0.6721
	5.6197	7.9138	6.9925		8.2623	8.5113	9.5232
	0	0	0		-8	0	0
	0.669	0.6686	0.6978		0.7924	0.7236	0.6808
	6.5606	5.6661	4.4766		8.1689	8.4868	9.3196
	1	4	1		-13	-18	0

Mid Depth 52.24m

Across-shelf Components				Alongshelf Components			
Correlation	0.3894	0.3577	0.2838	Correlation	0.6954	0.6972	0.7069
RMS Error	2.2007	2.6369	5.3663	RMS Error	9.3829	8.5174	9.097
Lag time (hrs)	63	70	71	Lag time (hrs)	-19	-9	-5
	0.2899	0.3276	0.2525		0.7278	0.7633	0.7419
	2.9644	6.083	13.2437		8.4102	10.5921	13.7329
	54	70	74		-8	-6	-2
	0.3927	0.4355	0.2962		0.7829	0.7356	0.7919
	3.8569	5.8625	24.322		14.1991	10.8708	21.4509
	57	70	63		-8	-9	-8

Near Bottom 72.24m

Across-shelf Components				Alongshelf Components			
Correlation	0.2819	0.1952	1.631	Correlation	0.7324	0.7283	0.7296
RMS Error	4.1452	6.9088	7.2566	RMS Error	7.942	7.9259	9.8922
Lag time (hrs)	5	3	70	Lag time (hrs)	-15	-7	3
	0.2786	0.3029	0.2083		0.7483	0.7553	0.7605
	4.9049	4.2376	3.9341		7.2663	8.6404	12.4354
	53	10	7		-7	8	7
	0.3654	0.3412	0.3046		0.781	0.8058	0.7399
	3.7677	8.111	8.0529		13.7516	15.5224	13.6092
	6	64	85		-3	-3	8

Table 14. Computed correlation values, RMS errors and lag times (hrs) for the HOPS Solo model at ADCP 2. The shaded grid points are insignificant and the bolded numbers are the highest/optimal correlations in the grid.

HOPS Nested
ADCP 1

Surface Currents 10.25m

Across-shelf Components				Alongshelf Components			
Correlation	0.3291	0.2753	0.2767	Correlation	0.7136	0.7105	0.7083
RMS Error	3.5035	3.8184	4.7509	RMS Error	6.3303	6.3654	6.3785
Lag time (hrs)	-137	-136	2	Lag time (hrs)	-12	-12	-12
	0.3058	0.2953	0.3153		0.7227	0.7207	0.7185
	3.6577	4.7431	4.9254		6.216	6.1842	6.139
	-137	2	1		-12	-12	-13
	0.3016	0.3228	0.3411		0.7307	0.7274	0.7263
	4.6166	4.8597	4.9701		6.1023	6.0385	5.9144
	2	2	1		-12	-13	-14

Mid Depth 34.25m

Across-shelf Components				Alongshelf Components			
Correlation	0.5559	0.5527	0.5459	Correlation	0.6883	0.6807	0.6734
RMS Error	1.5092	1.5456	1.5761	RMS Error	5.4306	5.4861	5.5257
Lag time (hrs)	8	8	8	Lag time (hrs)	-21	-21	-20
	0.563	0.5505	0.5349		0.6858	0.6789	0.675
	1.3971	1.4304	1.5355		5.4713	5.5024	5.516
	8	8	9		-21	-20	-20
	0.55	0.5292	0.5069		0.6878	0.6855	0.6884
	1.3979	1.4943	1.5955		5.4604	5.4541	5.4166
	10	10	11		-20	-20	-20

Near Bottom 46.25m

Across-shelf Components				Alongshelf Components			
Correlation	0.397	0.4167	0.4475	Correlation	0.586	0.6012	0.6101
RMS Error	1.8324	1.9044	1.8699	RMS Error	5.7792	5.5582	5.4469
Lag time (hrs)	106	105	105	Lag time (hrs)	-21	-20	-20
	0.4718	0.5011	0.4905		0.633	0.6384	0.6413
	1.5645	1.4759	1.4621		5.2651	5.2026	5.1838
	107	106	104		-21	-21	-21
	0.5192	0.5043	0.4725		0.6578	0.6607	0.6692
	1.3076	1.2976	1.3704		5.0833	5.0704	5.0161
	106	108	107		-22	-21	-20

Table 15. Computed correlation values, RMS errors and lag times (hrs) for the HOPS Nested model at ADCP 1. The shaded grid points are insignificant and the bolded numbers are the highest/optimal correlations in the grid.

HOPS Nested
ADCP 2

Surface Currents 12.24m

Across-shelf Components				Alongshelf Components			
Correlation	0.6103	0.6031	0.5928	Correlation	0.9014	0.8941	0.8855
RMS Error	5.1774	5.2	5.1964	RMS Error	8.6438	8.6661	8.7924
Lag time (hrs)	9	9	9	Lag time (hrs)	-4	-4	-5
	0.6273	0.6237	0.6149		0.8904	0.8815	0.8722
	5.4629	5.5645	5.5551		8.3172	8.3126	8.405
	8	8	9		-5	-4	-4
	0.6462	0.6301	0.6212		0.8799	0.8703	0.8628
	5.465	5.4673	5.4451		8.1106	8.0469	8.0766
	6	7	9		-5	-5	-4

Mid Depth 52.24m

Across-shelf Components				Alongshelf Components			
Correlation	0.6322	0.6424	0.6181	Correlation	0.8574	0.852	0.8489
RMS Error	1.6753	1.6704	1.7361	RMS Error	7.7783	7.8143	7.8414
Lag time (hrs)	17	18	18	Lag time (hrs)	-21	-21	-21
	0.594	0.6071	0.5756		0.8496	0.8435	0.8437
	1.812	1.8496	1.9116		7.7712	7.8281	7.8318
	17	18	18		-19	-19	-19
	0.5207	0.5217	0.5007		0.8506	0.8446	0.8428
	1.9354	1.9208	1.9254		7.826	7.8386	7.7809
	17	17	16		-18	-18	-18

Near Bottom 72.24m

Across-shelf Components				Alongshelf Components			
Correlation	0.3864	0.4067	0.407	Correlation	0.8626	0.8584	0.8525
RMS Error	1.8494	1.754	1.6988	RMS Error	6.4165	6.4492	6.607
Lag time (hrs)	2	1	1	Lag time (hrs)	-19	-18	-17
	0.4207	0.4406	0.4218		0.8353	0.8283	0.8174
	1.7244	1.6973	1.8189		6.6737	6.8247	7.0704
	3	5	10		-16	-16	-16
	0.4511	0.4825	0.5071		0.8144	0.8053	0.7969
	1.9278	2.1469	2.1981		7.0156	7.2506	7.4344
	11	14	17		-13	-13	-14

Table 16. Computed correlation values, RMS errors and lag times (hrs) for the HOPS Nested model at ADCP 2. The shaded grid points are insignificant and the bolded numbers are the highest/optimal correlations in the grid.

Angles of Principle Axis Ellipses		
	Mooring 1 (deg)	Mooring 2 (deg)
NCOM	-61.79	-57.24
ROMS	-69.51	-57.57
HOPSn	-56.61	-48.18
HOPSS	-63.08	-54.21
ADCP	-56.28	-49.56

Table 17. Calculated angles for the principle axis ellipses of each model and ADCP data for the individual mooring locations.

THIS PAGE INTENTIONALLY LEFT BLANK

LIST OF REFERENCES

Amos, D. E., and L. H. Koopmans (1963). Tables of the distribution of the coefficient of coherence for stationary bivariate Gaussian Processes. Sandia Corporation. SCR-438.

Bendat, J. S., and A. G. Piersol (1986). Random data: Analysis and measurement procedures. New York, John Wiley and Sons.

Breaker, L. C. and C. N. K. Mooers, 1986: Oceanic variability off the central California coast, *Progress in Oceanography*, **17**, 61-135.

Chassignet, E. P., M. J. Bell, P. Brassuer, G. Evensen, S. M. Griffies, H. E. Hurlburt, C. Leprovost, G. Madec, J. McClean, J. Verron, and A. J. Wallcraft (2002). The Modeling Component of Ocean Forecasting, in *Proceedings of the International Symposium "En route to GODAE"* (pp. 41-46). Biarritz, France.

Cordell Bank National Marine Sanctuary, March 2007, last accessed February 2007, from <http://cordellbank.noaa.gov/environment/seasons.html>.

Davis, R. E., 1976: Predictability of sea surface temperature and sea level pressure anomalies of the north Pacific Ocean, *Journal of Physical Oceanography*, **6**, 249-267.

Ekman, V. W. (1905). On the influence of the Earth's rotation on ocean-currents. *Arkiv for Matematik Astronomi O. Fysik*, 2(100), 1-52.

Graham, W. M. and J. L. Largier. 1997: Upwelling shadows as nearshore retention sites: The example northern Monterey Bay, *Continental Shelf Research*, **17**, 509-532.

Hickey, B. (1998). Coastal oceanography of western North America from the tip of Baja California to Vancouver Island. In A. R. Robinson and K. H. Brink (Eds.), *The Sea* (pp. 345-393). John Wiley and Sons, Inc.

Huyer, A., 1984: Hydrographic observations along the CODE central line off northern California, 1981, *Journal of Physical Oceanography*, **14**, 1647-1658.

Jet Propulsion Lab, July 2006, last accessed April 2007, from <http://ourocean.jpl.nasa.gov/MB06/>.

Kosro, P. M., 1987: Structure of the coastal current field off northern California during the coastal ocean dynamics experiment, *Journal of Geophysical Research*, **92**, 1637-1654.

Kundu, P. K., 1975: Ekman veering observed near the ocean bottom, *Journal of Physical Oceanography*, **6**, 238-242.

Large, W. G. and S. Pond, 1981: Open ocean momentum flux measurements in moderate to strong winds, *Journal of Physical Oceanography*, **11**, 324-326.

Lermusiaux, W. G., P. J. Haley, and W. G. Leslie, 2006: ASAP: Adaptive sampling and prediction Monterey Bay 2006, Harvard University, last accessed February 2007, from http://oceans.deas.harvard.edu/ASAP/index_ASAP.html.

NCOM Monterey Model, "Modeling Approach," August 2006, last accessed May 2007, from <http://www7320.nrlssc.navy.mil/ccsnrt-MontereyBay/ModelApproach/mainPage.html>.

Numerical Ocean Modeling, 2003, last accessed April 2007, from <http://www.oc.nps.navy.mil/nom/modeling/index.html>.

Princeton ASAP Program, 2006, last accessed April 2007, from <http://engineering.princeton.edu/gallery/asap/index.htm>.

Ramp, S. R., L. K. Rosenfeld, T. D. Tisch, and M. K. Hicks, 1997: Moored observations of the current and temperature structure over the continental slope off central California: 1. A basic description of variability, *Journal of Geophysical Research*, **102**, 22,877-22,902.

Ramp, S. R., and C. L. Abbott, 1998: The vertical structure of currents over the continental shelf off Point Sur, CA, during spring 1990, *Deep Sea Research Part II*, **45**, 1443-1470.

Ramp, S. R., J. D. Paduan, I. Shulman, J. Kindle, F. L. Bahr, and F. Chavez, 2005: Observations of upwelling and relaxation events in the northern Monterey Bay during August 2000, *Journal of Geophysical Research*, **111**, C07013, doi:10.1029/2004JC00238.

Robinson, A. R. (1999). Forecasting and simulating coastal ocean processes and variabilities with the Harvard Ocean Prediction System. In C. N. K. Mooers (Ed.), *Coastal Ocean Prediction*, AGU Coastal and Estuarine Studies Series (77-100). American Geophysical Union.

Rosenfeld, L. K., F. B. Schwing, N. Garfield, and D. E. Tracy, 1994: Bifurcated flow from an upwelling center: a cold water source for Monterey Bay, *Continental Shelf Research*, **14**, 931-964.

Schepetkin, A. F., and J. C. Williams, 2004: The Regional Oceanic Modeling System: a split –explicit, free surface, topography-following-coordinate ocean model, *Ocean Modeling*, **9**, 347-404.

Send U., R. C. Beardsley, and C. D. Winant, 1987: Relaxation from upwelling in the coastal ocean dynamics experiments, *Journal of Geophysical Research*, **92**, 1683-1698.

Shulman I., C. R. Wu, J. K. Lewis, J. D. Paduan, L. K. Rosenfeld, J. C. Kindle, S.R. Ramp, and C.A. Collins, 2002: High resolution modeling and data assimilation in the Monterey Bay area, *Continental Shelf Research*, **22**, 1129-1151.

Summary of Three Ocean Models, 2006, last accessed April 2007, from <http://aosn.mbari.org/coop/>.

Teledyne RD Instruments, 2007, last accessed January 2007, from <http://www.rdinstruments.com/sen.html>.

Winant, C. D., R. C. Beardsley, and R. E. Davis, 1987: Moored wind, temperature, and current observations made during coastal ocean dynamics experiments 1 and 2 over the northern California continental shelf and upper slope, *Journal of Geophysical Research*, **92**, 1569-1604.

THIS PAGE INTENTIONALLY LEFT BLANK

INITIAL DISTRIBUTION LIST

1. Defense Technical Information Center
Ft. Belvoir, Virginia
2. Dudley Knox Library
Naval Postgraduate School
Monterey, California
3. Dr. S. R. Ramp
Department of Oceanography
Monterey, California
4. Dr. L. K. Rosenfeld
Department of Oceanography
Monterey, California
5. Dr. M.L. Batteen
Department of Oceanography
Monterey, California
6. Rebecca Wolf, ENS, USN
Naval Postgraduate School
Monterey, California